Electroluminescence of Graded-gap Structures with Blocking and Ohmic Contacts

B. S. Sokolovskiĭ*^, V. I. Ivanov-Omskiĭ**, and G. A. Il'chuk***

*Franko National University, Lviv, 79602 Ukraine
^e-mail: sokol@franko.lviv.ua
**Ioffe Physicotechnical Institute, Russian Academy of Sciences, St. Petersburg, 194021 Russia
***Lviv National Polytechnic University, Lviv, 79013 Ukraine
Submitted April 11, 2005; accepted for publication April 13, 2005

Abstract—Special features of the electroluminescence of uniformly doped graded-gap structures with blocking and ohmic contacts are studied theoretically. Analytical expressions for the spectral and integrated electroluminescence intensities are derived and analyzed in the case of a constant gradient of the band gap and a strong absorption of light. It is shown that the presence of the blocking contact on the wide-gap face of the graded-gap structure leads to an increase in the efficiency of the negative and, especially, positive electroluminescence compared to the case of a graded-gap structure with two ohmic contacts. The recombination radiation of a graded-gap structure with the blocking contact at the narrow-gap face features in the majority of cases a sign-alternating spectral dependence; a broad band of negative electroluminescence is prevalent in this dependence in the region of high currents. © 2005 Pleiades Publishing, Inc.

1. INTRODUCTION

Graded-gap semiconductors feature a number of unique properties, first of all, the presence of quasi-electric fields and the coordinate dependence of the light-absorption coefficient; as a result, these semiconductors showed themselves to advantage as materials for the fabrication of various devices, in particular, light-emitting diodes [1, 2]. An appreciable spatial redistribution of minority charge carriers that occurs in the uniformly doped graded-gap semiconductors when a current flows through them [3] makes it possible to excite the recombination radiation in these semiconductors whose intensity differs significantly from that in the equilibrium state. In this context, theoretical consideration of the electroluminescent properties of various types of graded-gap structures is not only of academic interest but also of practical importance for the development of new sources of optical radiation, especially in the infrared region of the spectrum. It was shown previously [4] that the electroluminescence (EL) spectrum of graded-gap structures with ohmic contacts can be controlled in a wide range by varying the electric current; it is important that positive or negative EL arises depending on the current direction. In this paper, we show theoretically that the intensity of EL (especially, of positive EL) can be increased substantially by replacing one of the ohmic contacts of the graded-gap structure with a blocking contact.

2. MODEL OF A GRADED-GAP STRUCTURE AND THE ASSUMPTION FORMULAS

Let us consider a wafer that has the thickness d and is made of a graded-gap semiconductor (with the n-type conductivity for the sake of definiteness) in which the band gap E_g decreases linearly with the coordinate x, i.e.,

$$E_g(x) = E_g(0) - |\nabla E_g| x. \tag{1}$$

It is assumed that the graded-gap semiconductor is doped uniformly with a donor impurity with a fairly high concentration N_D, so that the equilibrium concentrations of electrons n_0 and holes p_0 are defined by the expressions [5]

$$n_0 \approx N_D, \quad p_0(x) = \frac{n_i^2(0)}{N_D} \exp\left(\frac{|\nabla E_g|}{kT} x\right), \tag{2}$$

where $n_i(x)$ is the intrinsic concentration of charge carriers in a graded-gap semiconductor.

Current-carrying contacts are formed on the graded-gap faces at $x = 0$ and $x = d$; one of these contacts is blocking, while the other is ohmic and makes sure that the charge-carrier concentration is equal to its equilibrium value. For example, an n–n^+ junction or an isotype heterojunction that contains a layer with a wider gap can be used as the blocking contact. We assume that the blocking contact blocks completely the flow of minority charge carriers. It is also assumed that the ohmic and

blocking contacts are transparent for the recombination radiation, which can be attained by choosing the appropriate materials for the contacts or by making these contacts into a grid configuration.

The flow of electric current through the graded-gap structure under consideration leads to a deviation of the hole concentration $p(x)$ from its equilibrium value $p_0(x)$, whereas the concentration of the majority charge carriers remains virtually unchanged.[1] The nonequilibrium-carrier recombination is accompanied by emission that is complementary to the equilibrium emission (i.e., by luminescence). Consideration of the recombination radiation that exits from the wide-gap face ($x = 0$) of the graded-gap structure is of the greatest interest since, in this case, the radiation can come from internal regions of the semiconductor owing to the effect of the wide-gap window. In the case where the light-absorption coefficient α is a step function of the photon energy $h\nu$

$$\alpha = \alpha_0 \theta[h\nu - E_g(x)],$$

we can use the data reported in [7] to represent the spectral intensity of EL I_ν measured from the wide-gap face as

$$I_\nu = \beta h\nu R_0 \int_{x_0}^{d} \frac{np - n_i^2}{n_i^2} \exp[-\alpha_0(x - x_0)]dx, \qquad (3)$$

where β is a coefficient that depends on the conditions of the exit of radiation through the face $x = 0$ and the contact on this face, in particular, on the angle of total internal reflection;

$$R_0 = 8\pi \bar{n}^2 c^{-2} \alpha_0 \nu^2 \exp(-h\nu/kT)$$

is the rate of equilibrium radiative recombination of charge carriers at $h\nu \gg kT$; $\bar{n}$ is the refractive index of the graded-gap semiconductor; and c is the speed of light in free space. The coordinate x_0 in formula (3) is determined from the equation $E_g(x_0) = h\nu$, i.e.,

$$x_0 = \frac{E_g(0) - h\nu}{|\nabla E_g|}. \qquad (4)$$

In what follows, we restrict ourselves to the case of strong absorption of light, assuming that the following inequalities are satisfied:

$$\alpha_0 \gg |\nabla E_g|/kT, d^{-1}, L_+^{-1}, L_-^{-1}.$$

---

[1] It is worth noting that the flow of a current through graded-gap structures with intrinsic conductivity is not accompanied by an appreciable spatial redistribution of the charge carriers. This behavior is possible under the effect of the Lorentz force under conditions where the magnetoconcentration effect is pronounced [6].

Here, L_+ and L_- are the characteristic lengths of variation in $p(x)$ along the direction of the charge-carrier drift motion or in the opposite direction, respectively. In this case, the functions that describe the coordinate dependences of the charge-carrier concentrations can be factored outside the integral sign in expression (3). As a result, we obtain the following expression for the EL intensity in the spectral range $E_g(d)/h \leq \nu \leq E_g(0)/h$:

$$I_\nu = \frac{N_D[p(x_0) - p_0(x_0)]}{n_i^2(x_0)} I_\nu^0. \qquad (5)$$

Here,

$$I_\nu^0 = 8\pi\beta\bar{n}^2 c^{-2} h\nu^3 \exp(-h\nu/kT)$$

is the spectral intensity of equilibrium emission from a graded-gap semiconductor in the region of the band-to-band transitions ($\nu \geq E_g(d)/h$). A weak frequency dependence of the ratio $I_\nu^0/n_i^2(x_0)$ at $E_g(d)/h \leq \nu \leq E_g(0)/h$ is a specific feature of formula (5). It is worth noting that, in contrast to the case of weak absorption of light [8], expression (5) for I_ν does not involve explicitly the gradient of the band gap. The EL intensity in the region $\nu > E_g(0)/h$ is defined by formula (5) where we should set $x_0 = 0$.

The spatial (coordinate) distribution of the nonequilibrium-hole concentration, which is required for calculating the EL intensity and is established in a graded-gap semiconductor after the passage of a current with the density **j**, defined by the continuity equation [3]

$$\frac{d^2p}{d\xi^2} - (i + \gamma)\frac{dp}{d\xi} - p = -\frac{n_i^2(0)}{N_D}\exp(\gamma\xi), \qquad (6)$$

where we introduced the dimensionless quantities: the coordinate $\xi = x/L_p$, the current density $i = j_x L_p/kT\mu_n N_D$, and the band-gap gradient $\gamma = L_p|\nabla E_g|/kT$. It is assumed that the diffusion length of holes L_p and the mobilities of electrons μ_n and holes μ_p are coordinate-independent. Equation (6) is valid if the inequality $\mu_n N_D \gg \mu_p p_0(d)$ is satisfied, i.e., if the contribution of the minority charge carriers to the total current can be disregarded.

Equation (6) should be supplemented with two boundary conditions that are written as

$$\frac{dp(0)}{d\xi} - (i + \gamma)p(0) = 0, \quad p(\bar{d}) = \frac{n_i^2(\bar{d})}{N_D}\exp(\gamma\bar{d}) \quad (7)$$

($\bar{d} = d/L_p$) for a graded-gap structure with a blocking contact on the wide-gap face ($\xi = 0$) and

$$p(0) = \frac{n_i^2(0)}{N_D}, \quad \frac{dp(\bar{d})}{d\xi} - (i + \gamma)p(\bar{d}) = 0 \qquad (8)$$

for a graded-gap structure with a blocking contact formed on the narrow-gap face ($\xi = \bar{d}$).

$$I_\nu = \frac{i}{i\gamma + 1}\left[\frac{\exp(-\delta^-\xi_0)\{\sinh[\delta^*(\xi_0 - \bar{d})] + \gamma\varphi(\xi_0)\exp(\delta^-\bar{d})\}}{\varphi(\bar{d})} - \gamma\right]I_\nu^0, \qquad (9)$$

where,

$$\varphi(z) = \delta^+\sinh(\delta^*z) + \delta^*\cosh(\delta^*z),$$

$$\delta^\pm = \frac{\gamma \pm i}{2}, \quad \delta^* = \frac{\sqrt{(\gamma + i)^2 + 4}}{2}.$$

If the variable $\xi_0 = x_0/L_p$ and formula (4) are used, expression (9) defines the spectral dependence of the EL intensity in the range

$$E_g(d)/h \le \nu \le E_g(0)/h \quad (0 \le \xi_0 \le \bar{d}).$$

The EL spectrum in the frequency region $\nu > E_g(0)/h$ can be calculated using the formula

$$I_\nu = \frac{(h\nu)^3}{E_g^3(0)}I_\nu^{max}\exp\left[-\frac{h\nu - E_g(0)}{kT}\right], \qquad (10)$$

where I_ν^{max} is the EL intensity obtained using expression (9) at $\nu = E_g(0)/h$.

As follows from expressions (9) and (10), the features of EL are governed by the electric-current direction. If the current i flows in the direction in which the band gap increases ($i < 0$), the entire volume of a graded-gap semiconductor is enriched with nonequilibrium charge carriers as a result of the hole injection from the structure's regions with a narrower band gap. Radiative recombination of the above nonequilibrium carriers forms the spectrum of positive EL. If the direction of the current is opposite ($i > 0$), so that holes drift in the direction corresponding to a decrease in the band gap (i.e., in the direction that corresponds to an increase in the hole equilibrium concentration), the effect of the distributed extraction of nonequilibrium charge carriers becomes pronounced [3]; as a result of this effect, virtually the entire volume of the semiconductor is found to be depleted of holes. This circumstance brings about a decrease in the recombination-radiation intensity as compared to its equilibrium value; i.e., the so-called negative luminescence originates. This type of luminescence was observed for the first time in indium antimonide placed in crossed electric and magnetic fields [9] and was then studied in detail in a number of semi-

3. RESULTS OF CALCULATIONS AND DISCUSSION

3.1. The Case of a Graded-Gap Structure with a Blocking Contact on the Wide-Gap Face

Solving Eq. (6) with boundary conditions (7) and using formula (5), we obtain the following expression:

conductors both in the case of the magnetoconcentration effect and in the cases of the exclusion and extraction effects (see, for example, reviews [10, 11]).

The EL intensity I_ν is proportional to the current for each frequency if the currents are low ($|i| \ll \gamma$, $\bar{d}^{-1}$, $\bar{d}$). In contrast, as the current increases, the current dependence of I_ν becomes nonlinear; it is noteworthy that variations in the current affect the different portions of the EL spectrum differently. In the region of high currents ($|i| \gg \gamma$, $\bar{d}^{-1}$, $\bar{d}$) and at $i < 0$, in which case a constant hole concentration $p_0(d)$ is established in almost the entire volume of the semiconductor (except for a thin layer that has a thickness on the order of $|i|^{-1}$ and is adjacent to the blocking contact), the spectral intensity of positive EL in the approximation linear in γ/i and $\bar{d}/i$ is described by the expressions

$$I_\nu = i^2\left(1 - \frac{2\gamma}{|i|}\right)\exp(-|i|\xi_0 + \gamma\bar{d})I_\nu^0 \qquad (11)$$

if $0 \le \xi_0 < 2|i|^{-1}\ln|i|$ and

$$I_\nu = \left[\left(1 + \frac{\xi_0 - \bar{d}}{|i|}\right)\exp[\gamma(\bar{d} - \xi_0)] - 1\right]I_\nu^0 \qquad (12)$$

if $2|i|^{-1}\ln|i| < \xi_0 \le \bar{d}$. Here, I_ν^0 is the intensity of the equilibrium radiation.

Thus, the spectrum of positive EL observed at high currents consists of (i) an extended long-wavelength portion whose shape is independent of the current and depends only on the band-gap gradient and (ii) a narrow short-wavelength band that becomes even narrower (and the EL at the edge of this band (at $h\nu = E_g(0)$) is intensified simultaneously) as the current increases. It is worth noting that $I_\nu = 0$ at $h\nu = E_g(0)$ in the case of a graded-gap structure with two ohmic contacts [4]. The position of the peak in the spectrum of positive EL for the graded-gap structure under consideration is independent of the current and is located at $h\nu = E_g(0)$.
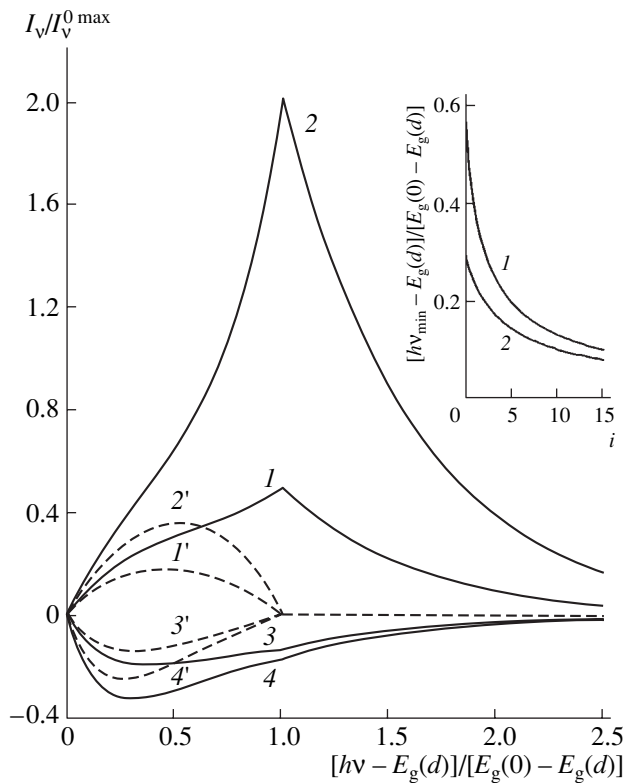
Fig. 1. Spectral dependences of the electroluminescence intensity for a graded-gap structure with the blocking contact on the wide-gap face (solid lines) and with two ohmic contacts (dashed lines) at $E_g(0) = 16kT$, $\bar{d} = 2$, $\gamma = 1$, and the dimensionless current density $i = (1, 1') -1$, $(2, 2') -2$, $(3, 3')$ 1, and $(4, 4')$ 2. In the inset, we show the dependences of the position of the minimum in the spectrum of negative electroluminescence on the dimensionless current density at $\gamma = (1)$ 1 and (2) 2.

In the region of high currents ($i \gg \gamma$, $\bar{d}^{-1}$, $\bar{d}$), the spectrum of negative EL that arises at $i > 0$ includes a broad feature in the range

$$0 \leq \xi_0 < \bar{d} - i^{-1}\ln(i\gamma)$$

with an intensity close to the limiting value $-I_\nu^0$,

$$I_\nu = -\left[1 - \frac{1}{i\gamma} + \frac{1}{i\gamma}\left(1 - \frac{\gamma}{i} - \frac{\xi_0}{i}\right)\exp(-\gamma\xi_0)\right]I_\nu^0, \quad (13)$$

and a narrow long-wavelength band ($\bar{d} - i^{-1}\ln(i\gamma) < \xi_0 \leq \bar{d}$) whose intensity vanishes exponentially as

$$I_\nu = -\{1 - \exp[i(\xi_0 - \bar{d})]\}I_\nu^0. \quad (14)$$

A minimum in the spectral dependence of the negative-EL intensity shifts to longer wavelengths as the current increases and is located at the following photon energy in the high-current region:

$$h\nu_{\min} = E_g(d) + \frac{kT\gamma}{i}\ln(i\gamma). \quad (15)$$

In order to calculate the spectral dependences of the EL intensity using formulas (9) and (10), we should know the equilibrium-emission intensity I_ν^0 that is controlled by the minimum band gap in a specific graded-gap structure in the case of strong absorption of light. It is noteworthy that the shape of the EL-intensity spectral dependences is nearly the same for various semiconductors at insignificant variations in the band gap $[E_g(0) - E_g(d)]/E_g(d)$, specifically, if the inequality $kT\gamma\bar{d} \ll E_g(d)$ is satisfied; it is evident that this inequality can be more easily satisfied in the case of wide-gap semiconductors.

In what follows, we illustrate special features of EL in graded-gap structures taking as an example the CdHgTe alloy that is of great interest for fabricating not only detectors but also sources of infrared radiation. We assume that we have an n-CdHgTe graded-gap structure at $T = 290$ K with a fixed band gap at the face with the wider band gap $E_g(0) = 0.4$ eV ($E_g(0)/kT = 16$); at this face, the donor concentration $N_D = 5 \times 10^{15}$ cm^{-3}, the hole diffusion length $L_p = 10$ μm, and the electron mobility $\mu_n = 2 \times 10^3$ cm^2/(V s) [12, 13]. We assume that the thickness of the graded-gap structure is 20 μm (i.e., $\bar{d} = 2$). For the above parameters, the relations between the dimensional and dimensionless values of the current densities and the band-gap gradients are as follows: $j_x = 40i$ A/cm^2 and $dE_g/dx = 25\gamma$ eV/cm. In Fig. 1, we show the dependences of intensities of the positive and negative EL on the photon energy in the region of intermediate currents ($|i| \gtrsim \gamma$). The spectral dependences of EL for graded-gap structures with ohmic contacts are also shown in Fig. 1 for the sake of comparison. As can be seen from Fig. 1, the EL spectra of both types of the graded-gap structures differ radically from one another. First, the spectra of the positive and negative EL extend to the region of energies that exceed the maximum value of the band gap $E_g(0)$ in the graded-gap structures with a blocking contact on the wide-gap face. Second, the presence of a blocking contact brings about an increase in the intensity of positive EL in the entire frequency range, especially in its short-wavelength region; it is noteworthy that not only the EL intensity but also the spectral-curve asymmetry increase as the current increases. As compared to the case of positive EL, the effect of the blocking contact on the negative-EL intensity is weaker because the absolute value of this EL intensity cannot exceed the intensity of the equilibrium recombination radiation. The position of the minimum in the spectrum of negative EL (as can be seen from the inset in Fig. 1) shifts appreciably to shorter wavelengths as the current and the band-gap gradient increase.

The integrated intensities I of the positive and negative EL for the graded-gap structure under consideration are obtained by integrating expressions (9) and (10) in the relevant frequency range; in the region of

high currents ($|i| \gg \gamma$, $\bar{d}^{-1}$, $\bar{d}$), these dependences are described by the following relations:

$$I = \frac{E_g^3(0)}{E_g^3(d)}$$

$$\times \left[i^2 \left(1 - \frac{\gamma}{|i|} - \frac{3kT}{E_g(d)} + \frac{3kT}{E_g(0)} \right) + \frac{E_g^4(0) - E_g^4(d)}{4kTE_g^3(0)} \right] I_0, \quad (16)$$

$$I = -\left[1 - \frac{1}{i\gamma} - \frac{\gamma}{i} \left(1 - \frac{3kT}{E_g(d)} \right) \right] I_0. \quad (17)$$

Here,

$$I_0 = 8\pi\beta\bar{n}^2 c^{-2} kT h^{-4} E_g^3(d)$$

$$\times [1 + 3kT/E_g(d)] \exp(-E_g(d)/kT)$$

is the integrated intensity of the equilibrium recombination radiation for the graded-gap structure. Dependences (16) and (17) were obtained in the first approximation with respect to the parameters γ/i and $kT/E_g(d)$ in the case where $E_g(d) \gg kT$ and $\exp(\gamma\bar{d}) \gg 1$.

It follows from expression (16) that, in the region of high currents, the relative value of the positive-EL intensity I/I_0 increases following a square law as the current increases and depends superlinearly on the band-gap gradient. It is noteworthy that the dependence $I/I_0 \sim \gamma^3$ takes place at $\gamma \gg E_g(d)/kT\bar{d}$. The ratio between the intensities of the positive EL for the graded-gap structures with a blocking contact (I) and for those with two ohmic contacts (I^*) in the range of high currents at $E_g^4(0) \gg E_g^4(d)$ is given by

$$\frac{I}{I^*} = \frac{4kT}{E_g(0)} \left(1 - \frac{\gamma}{|i|} \right) i^2; \quad (18)$$

i.e., the presence of a blocking contact on the wide-gap face makes it possible to increase substantially the integrated intensity of recombination emission from a graded-gap semiconductor. This behavior is caused by the absence of a restriction imposed on the concentration of nonequilibrium charge carriers at (and in the vicinity of) the wide-gap face; this restriction takes place in the case of the ohmic contact.

The absolute value of the integrated intensity of the negative EL for the structure under consideration exceeds the corresponding quantity for a graded-gap structure with two ohmic contacts for all values of the band-gap gradient. It is important that, for the most interesting case of $\gamma \gtrsim 1$, this excess decreases as the band-gap gradient increases, which follows, in particular, from expression (17). An important specific feature of the integrated intensity of the negative EL for a graded-gap structure with a blocking contact at the wide-gap face consists in the steady decrease to zero of the difference $I_0 - |I|$. In contrast, a similar difference
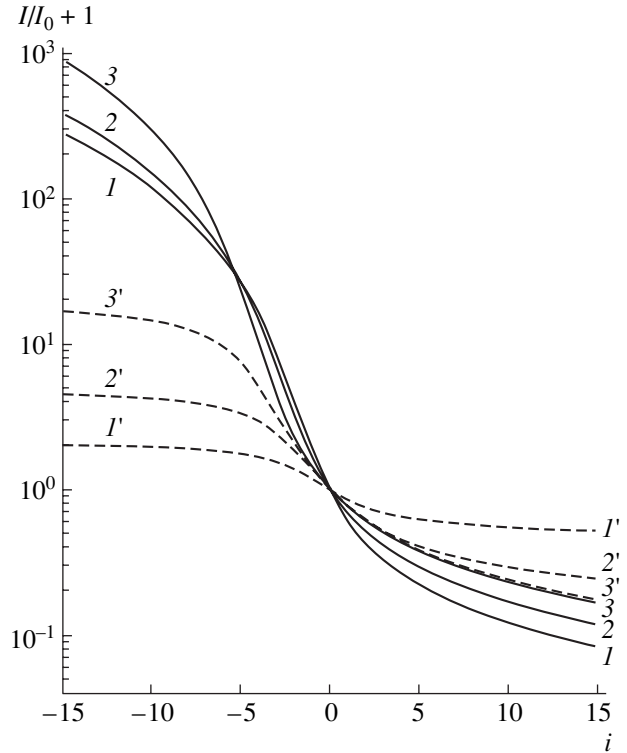

Fig. 2. The current dependences of the integrated electroluminescence intensity for a graded-gap structure with the blocking contact on the wide-gap face (solid lines) and with two ohmic contacts (dashed lines) at $E_g(0) = 16kT$, $\bar{d} = 2$, and $\gamma = (1, 1')$ 1, $(2, 2')$ 2, and $(3, 3')$ 4.

$I_0 - |I^*|$ for a graded-gap structure with two ohmic contacts tends asymptotically to a nonzero value [4]. It can be shown that, in the case of very high currents ($i \gg \gamma\exp(\gamma\bar{d})$, $\bar{d}$, $\bar{d}^{-1}$), the ratio between the above differences is inversely proportional to i, i.e.,

$$\frac{I_0 - |I|}{I_0 - |I^*|} = \frac{4kTE_g^3(d)}{E_g^4(0)} \frac{\gamma}{i} \exp(\gamma\bar{d}). \quad (19)$$

The current dependences of the integrated EL intensities (see Fig. 2) illustrate clearly the quantitative advantage that can be attained if the ohmic contact on the wide-gap face of the graded-gap structure is replaced by the blocking contact, especially in the case of excitation of the positive EL. As can be seen from Fig. 2, in the region of intermediate magnitudes of negative currents ($|i| \propto \gamma$), the integrated intensity of the positive EL decreases as the band-gap gradient increases, in contrast to the case of high currents. This behavior is caused by the fact that, in this range of currents, the most pronounced counteraction of the internal electric field to spatial redistribution of charge carriers takes place.

3.2. The Case of a Graded-Gap Structure with a Blocking Contact on the Narrow-gap Face

For this type of a graded-gap structure, the spectral dependence of the EL intensity in the range $E_g(d)/h \leq \nu \leq E_g(0)/h$ can be derived using formula (5) and Eqs. (6) and (8); as a result, we obtain the expression

$$I_\nu = \frac{i}{i\gamma + 1}\left[\frac{\exp(-\delta^-\xi_0)\{\exp(\delta^{-1}\bar{d})\sinh[\delta^*(\xi_0 - \bar{d})] + \gamma\varphi(\xi_0 - \bar{d})\}}{\varphi(-\bar{d})} - \gamma\right]I_\nu^0, \qquad (20)$$

where the notation used is the same as in formula (9).

As for the recombination radiation in the spectral region $\nu \geq E_g(0)/h$, the EL intensity is equal to zero as a result of the absence of the excess charge-carrier concentration at the wide-gap face with an ohmic contact in the conditions of strong absorption of light.

The characteristic feature of EL in a graded-gap structure with a blocking contact on the narrow-gap face is the fact that it is possible to excite simultaneously both the positive and negative EL; this means that the emission spectra include "zero" points at which the sign reversal of the EL intensity occurs. It is worth noting that the "zero" points are also characteristic of the spectra of the photomagnetic [14] and photovoltaic [15] effects in thin graded-gap layers. An analysis of expression (20) shows that the "zero" points are present necessarily in the EL spectra excited at $i > 0$. At the same time, these points can exist in the case of the opposite direction of the current ($i < 0$) only if the following inequality is satisfied:

$$\frac{2}{\gamma}\exp\left[\frac{(\gamma + |i| - \sqrt{(|i| - \gamma)^2 + 4})\bar{d}}{2}\right] \qquad (21)$$
$$\leq |i| - \gamma + \sqrt{(|i| - \gamma)^2 + 4}.$$

The range of currents at which inequality (21) is satisfied widens with increasing band-gap gradient and extends to the regions of high currents at $\gamma \ll |i| \leq \exp(\gamma\bar{d})/\gamma$.

Let us consider briefly the asymptotic properties of the EL spectra in the region of high currents defined by the inequalities $||i| \gg \exp(\gamma\bar{d})/\gamma$, $\bar{d}$, $\bar{d}^{-1}$. If the direction of the electric current is positive, the recombination radiation includes an extended portion ($0 \leq \xi_0 < \bar{d}(1 + \gamma/i) - 2i^{-1}\ln i$) of negative EL with the intensity

$$I_\nu = -\left[1 - \left(1 - \frac{\xi_0}{i}\right)\exp(-\gamma\xi_0)\right]I_\nu^0 \qquad (22)$$

and a narrow portion ($\bar{d} - 2i^{-1}\ln i < \xi_0 \leq \bar{d}$) with a sharp variation in the intensity:

$$I_\nu = \left[i^2\left(1 + \frac{2\gamma}{i}\right)\exp[i(\xi_0 - \bar{d}) - \gamma\bar{d}] - 1\right]I_\nu^0; \qquad (23)$$

in this region, negative EL is replaced by positive EL at $\xi_0 \approx \bar{d}(1 + \gamma/i) - 2i^{-1}\ln i$.

In the region of high negative currents, the recombination radiation manifests itself as negative EL in the entire spectral region of excitation (positive EL is not observed since inequality (21) is not satisfied); the dependence of the negative-EL intensity on the frequency of light is described by the expressions

$$I_\nu = -\left[1 + \frac{1}{|i|\gamma} \right. $$
$$\left. - \frac{1}{|i|\gamma}\left(1 + \frac{\gamma}{|i|} + \frac{\xi_0}{|i|}(\xi_0 - \bar{d})\right)\exp[\gamma(\bar{d} - \xi_0)]\right]I_\nu^0 \qquad (24)$$

at

$$|i|^{-1}[\ln|i\gamma| - \gamma\bar{d}] < \xi_0 \leq \bar{d}$$

and

$$I_\nu = -[1 - \exp(-|i|\xi_0)]I_\nu^0 \qquad (25)$$

at

$$0 \leq \xi_0 < |i|^{-1}[\ln|i\gamma| - \gamma\bar{d}].$$

The spectral dependences of the EL intensity for a graded-gap structure with a blocking contact on the narrow-gap face in the region of intermediate currents ($|i| \gtrsim \gamma$) are shown in Fig. 3. It can be seen that an appreciable increase in the absolute value of the EL intensity in the long-wavelength region is attained if the ohmic contact on the narrow-gap face is replaced by the blocking contact; however, the EL intensity is much lower in the short-wavelength portion of the spectrum in the case of the blocking contact. The current dependences of the zero-point position in the EL spectrum (Fig. 3, inset) indicate that the most significant shift of this point as the current increases occurs in the range of relatively low currents.

The recombination radiation excited by a high current ($|i| \gg \exp(\gamma\bar{d})/\gamma$, $\bar{d}$, $\bar{d}^{-1}$) that flows towards the narrow-gap face ($i > 0$) in the case of $E_g(d) \gg kT$ and $\exp(\gamma\bar{d}) \gg 1$ has the integrated intensity

$$I = \left[i\gamma\left(1 + \frac{\gamma}{i} + \frac{3kT}{E_g(0)} - \frac{3kT}{E_g(d)}\right)\exp(-\gamma\bar{d}) - 1\right]I_0, \qquad (26)$$
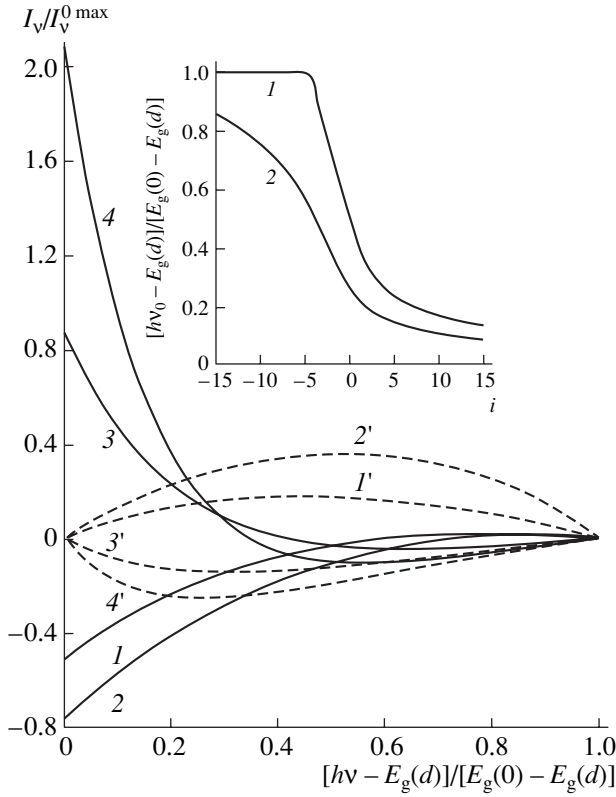
Fig. 3. Spectral dependences of the electroluminescence intensity for a graded-gap structure with a blocking contact on the narrow-gap face (solid lines) and with two ohmic contacts (dashed lines) at $E_g(0) = 16kT$, $\gamma = 1$, $\bar{d} = 2$, and the dimensionless current density $i = (1, 1')$ –1, $(2, 2')$ –2, $(3, 3')$ 1, and $(4, 4')$ 2. In the inset, we show the dependences of the zero-point position on the dimensionless current density at $\gamma = (1)$ 1 and (2) 2.

Fig. 4. Dependences of the integrated intensity of the positive (solid lines) and negative (dashed lines) electroluminescence for a graded-gap structure with a blocking contact on the narrow-gap face and the integrated intensity of electroluminescence for a graded-gap structure with two ohmic contacts (dash–dotted lines) on the dimensionless current density at $E_g(0) = 16kT$, $\bar{d} = 2$, and $\gamma = (1, 1', 1'')$ 1 and $(2, 2', 2'')$ 2.

$$I = -\left[1 - \left(\frac{E_g^4(0) - E_g^4(d)}{4kTE_g^3(d)}\right)\exp(-\gamma\bar{d}) + \frac{\gamma}{i}(2\ln i - \gamma\bar{d})\right]I_0 \quad (27)$$

for the positive and negative EL, respectively.

As follows from the expressions obtained, the integrated intensity of the positive EL at high currents decreases as the band-gap gradient increases; this intensity exceeds that for a graded-gap structure with two ohmic contacts if the band-gap gradient is small ($\gamma\bar{d} \approx 1$). At the same time, the absolute value of the integrated intensity of the negative EL decreases steadily as the band-gap gradient increases and remains smaller than that for a graded-gap structure with two ohmic contacts [4].

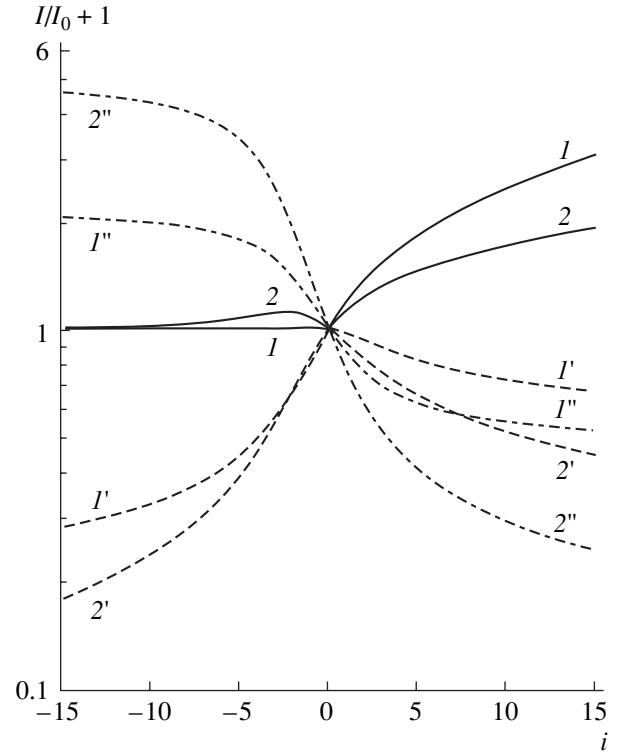The integrated intensity of negative EL excited by high negative currents in a graded-gap structure with the blocking contact on the narrow-gap face is given by the expression

$$I = -\left[1 - \frac{1}{|i|\gamma}\left(\frac{E_g^4(0) - E_g^4(d)}{4kTE_g^3(d)} - 1\right) - \frac{\gamma}{|i|}\exp(-\gamma\bar{d})\right]I_0; \quad (28)$$

i.e., as the current and the band-gap gradient increase, the negative-EL intensity tends to the value $-I_0$ whose magnitude exceeds that of the limiting value of the negative-EL integrated intensity for a graded-gap structure with two ohmic contacts.

The current dependences of integrated intensities for the positive and negative EL were obtained by numerical integration of expression (20) as applied to a CdHgTe graded-gap structure with $E_g(0) = 0.4$ eV at $T = 290$ K and are shown in Fig. 4. It can be seen that, with negative currents, the graded-gap structure with a blocking contact on the narrow-gap face is a more efficient source of recombination radiation with negative contrast than the structure with two ohmic contacts.

4. CONCLUSION

In this study, we used the model of a uniformly doped graded-gap semiconductor structure with blocking and ohmic contacts in the case of linear coordinate dependence of the band gap and strong absorption of light to calculate analytically the intensity of electroluminescence (EL) emitted from the wide-gap face of the structure. It is shown that the presence of a blocking contact on the wide-gap face of the graded-gap structure brings about an appreciable increase in the EL efficiency (especially for positive EL) compared to the case of the structure with two ohmic contacts. As a result of replacing the ohmic contact with a blocking contact, the spectrum of positive EL changes radically so that the spectral peak becomes located at the photon energy corresponding to the maximum band gap in the graded-gap structure. The distinguishing feature of the emission spectra for a graded-gap structure with the blocking contact on the narrow-gap face consists in the fact that the portions of the positive and negative EL are present in the spectra and are separated by the "zero" point whose position depends on the values of the electric current and band-gap gradient. The ohmic contact also plays an important role in the structures under study; this contact exhibits a high generation–recombination activity and is conducive to effective accumulation of charge carriers in the semiconductor bulk for one direction of the current and to a pronounced depletion of the carriers for the other direction of the current. In order to illustrate the systematic features of EL that are inherent in the type of the graded-gap structure under consideration, we chose the CdHgTe alloy with varying composition and with a band gap equal to 0.4 eV at the wide-gap face. At the same time, it is worth noting that numerical calculations are required to predict accurately the electroluminescent properties of the graded-gap structure based on CdHgTe; these calculations should include consideration of both the non-linear mechanisms of the charge-carrier recombination and the realistic values of the coefficient of light absorption.

REFERENCES

1. Zh. I. Alferov, Usp. Fiz. Nauk **172**, 1072 (2002).
2. G. Kremer, Usp. Fiz. Nauk **172**, 1091 (2002).
3. V. G. Savitskiĭ and B. S. Sokolovskiĭ, Ukr. Fiz. Zh. **25**, 1919 (1980).
4. B. S. Sokolovskiĭ, Fiz. Tekh. Poluprovodn. (St. Petersburg) **29**, 1657 (1995) [Semiconductors **29**, 862 (1995)].
5. B. S. Sokolovs'kiĭ, Ukr. Fiz. Zh. **39**, 327 (1994).
6. V. G. Savitskiĭ and B. S. Sokolovskiĭ, Zh. Prikl. Spektrosk. **62**, 222 (1995).
7. W. van Roosbroeck and W. Shockley, Phys. Rev. **94**, 1558 (1954).
8. A. S. Volkov and G. V. Tsarenkov, Fiz. Tekh. Poluprovodn. (Leningrad) **11**, 1709 (1977) [Sov. Phys. Semicond. **11**, 1004 (1977)].
9. V. I. Ivanov-Omskiĭ, B. T. Kolomiets, and V. A. Smirnov, Dokl. Akad. Nauk SSSR **161**, 1308 (1965) [Sov. Phys. Dokl. **10**, 345 (1965)].
10. P. Berdahl, V. Malytenko, and T. Morimoto, Infrared Phys. **29**, 667 (1989).
11. C. T. Elliott, Philos. Trans. R. Soc. London, Ser. A **359**, 567 (2001).
12. N. N. Berchenko, V. E. Krevs, and V. G. Sredin, *Semiconductor Solid Solutions and Their Applications* (Voenizdat, Moscow, 1982) [in Russian].
13. *Properties of Narrow Gap Cadmium-based Compounds*, Ed. by P. Capper (INSPEC, London, 1994).
14. S. G. Petrosyan, Fiz. Tekh. Poluprovodn. (Leningrad) **11**, 886 (1977) [Sov. Phys. Semicond. **11**, 522 (1977)].
15. B. S. Sokolovskiĭ, Fiz. Tekh. Poluprovodn. (St. Petersburg) **30**, 1006 (1996) [Semiconductors **30**, 535 (1996)].

Translated by A. Spitsyn

Mössbauer Study of the Ge Two-Electron Donor Centers in PbSe

E. I. Terukov*^ and É. S. Khuzhakulov**

Ioffe Physicotechnical Institute, Russian Academy of Sciences, Politekhnicheskaya ul. 26, St. Petersburg, 194021 Russia
^e-mail: Eug.Terukov@mail.Ioffe.ru
**Tashkent Regional Pedagogical Institute, Dmitrov st. 4, Angren, Tashkent Region, 702500 Uzbekistan*
Submitted March 30, 2005; accepted for publication April 15, 2005

Abstract—Mössbauer emission spectroscopy at ^{73}As(^{73}Ge) is used to show that the charge state of the ^{73}Ge antisite defect formed in the anion sublattice after the radioactive transformation of ^{73}As is independent of the position of the Fermi level. In contrast, the ^{73}Ge center in the cation sublattice of PbSe is an electrically active substitutional impurity. For the n-type samples, the spectrum corresponds to the neutral state of the donor center (^{73}Ge^{2+}), and for the p-type samples, the spectrum corresponds to the doubly ionized state (^{73}Ge^{4+}) of this center. © 2005 Pleiades Publishing, Inc.

Interest in the problem of the behavior of two-electron centers with negative correlation energy in semiconductors is associated with the possibility of explaining the anomalously high superconducting transition temperatures of semiconductors with these centers using the model of bielectrons located in the Bose condensate at the lowest energy level of impurity centers [1]. However, despite the successful use of these notions, no two-electron centers with negative correlation energy were observed in semiconductors by direct experimental methods. They are introduced into the theoretical models via a priori assumptions. The only exclusion is the Sn impurity in lead chalcogenides where these centers were identified by Mössbauer spectroscopy for ^{119}Sn [2].

Another evident candidate for identifying two-electron centers with negative correlation energy by Mössbauer spectroscopy is the Ge impurity in lead chalcogenides. In its physicochemical properties, Ge is very similar to Sn, and the spectral characteristics of ^{73}Ge are among the best of all Mössbauer isotopes. However, the use of the absorption variant of Mössbauer spectroscopy to identify the charge state of the Ge impurity atoms in lead chalcogenides is almost impossible because of the low energy of the isomeric transition in ^{73}Ge (~13 keV) and the large absorption coefficient of the corresponding photons by Pb. In this case, it is more promising to use the emission variant of Mössbauer spectroscopy. Nemov *et al.* [3] showed by the example of the ^{119}Sn impurity that the emission variant of Mössbauer spectroscopy allows one to stabilize the impurity atoms at unconventional lattice sites. For example, metal Sn can be located in the anion sublattice of lead chalcogenides [4].

In this study, the emission variant of Mössbauer spectroscopy at ^{73}As(^{73}Ge) was used to identify the neutral and ionized two-electron Ge centers in PbSe. Taking into account the fact that the recoil energy of the ^{73}Ge daughter atoms after the radioactive decay of the ^{73}As parent atoms does not exceed the energy of the atoms' displacements from the lattice site, we could expect that the parameters of the emission Mössbauer spectra for ^{73}As(^{73}Ge) will be associated with the ^{73}Ge atoms located at the As sites.

The ^{73}As radioactive isotope was obtained by irradiating a single-crystal target with a proton beam. The target was made of the ^{74}Ge isotope enriched to 98%. The required isotope was obtained by the reaction ^{74}Ge(p,2n)^{73}As with the subsequent isolation of carrier-free preparation ^{73}As by the "dry chemistry" method [5].

The Mössbauer sources PbSe:^{73}As were prepared by alloying the PbSe samples with the carrier-free preparation ^{73}As so that the concentration of the As atoms was ~10^{17} cm^{-3}. The starting samples of PbSe were degenerate in both the *n*- or *p*-type states. In the first case, the samples had an excess of Pb, so that the electron concentration was $n \approx 10^{18}$ cm^{-3}; in the second case, there was an excess of Se and the hole concentration was $p \approx 10^{18}$ cm^{-3}. The Mössbauer spectra for ^{73}Ge were measured at room temperature using an SM-2201 commercial spectrometer. The specific feature of Mössbauer spectroscopy at ^{73}Ge is the unusually large isomer shifts. As a result, it is virtually impossible to detect the charge states Ge^0, Ge^{2+}, and Ge^{4+} in one experimental spectrum. Therefore, when measuring the experimental spectra PbSe:^{73}As, we used the procedure suggested and implemented by Nemov *et al.* [6]. The spectra were recorded using absorbers in the form of the Ge metal film to detect the spectral lines corresponding to the Ge^0 center, in the form of the GeSe fine-crystalline film to detect the spectral lines corresponding to the Ge^{2+} centers, and in the form of the GeSe$_2$ fine-crystalline film to detect the spectral lines corresponding to the Ge^{4+} centers. The surface density by the ^{73}Ge isotope for all absorbers was 10 mg/cm^2, and the enrichment with the ^{73}Ge isotope was 90%. The typical
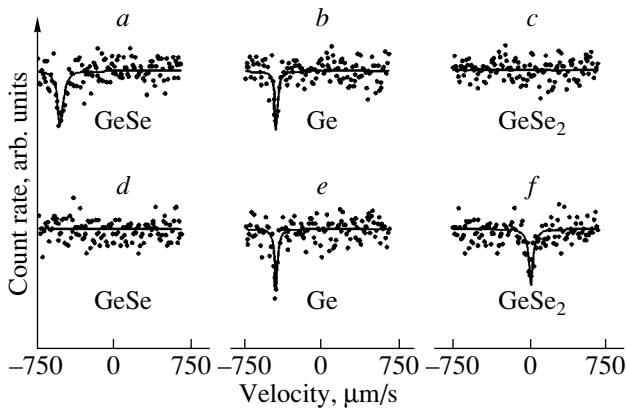
Emission Mössbauer spectra of the sources n-PbSe:^{73}As (a, b, c) and p-PbSe:^{73}As (d, e, f) at 295 K with absorbers ^{73}GeSe (a, d), ^{73}Ge (b, e), and ^{73}GeSe$_2$ (c, f).

spectra of the n- and p-PbSe:^{73}As sources with the mentioned absorbers are shown in the figure. The results of processing the experimental spectra are given in the table.

The spectra of the n-type samples with the GeSe and Ge absorbers consist of individual lines (see figure, spectra a, b). The spectrum with absorber Ge (spectrum of type I) features an isomer shift that is expected for Ge-containing intermetallic compounds; this shift should be attributed to the ^{73}Ge^0 centers in the anion sublattice of PbSe with the nearest surrounding consisting of the Pb atoms. It is evident that the ^{73}Ge^0 atoms are formed from the ^{73}As parent atoms that are located in the anion sublattice of PbSe. The spectrum with the GeSe absorber (spectrum of type II) exhibits an isomer shift that is expected for the compounds of divalent Ge and should be attributed to the ^{73}Ge^{2+} centers in the cation sublattice of PbSe with the nearest surrounding consisting of Se atoms. It is evident that the ^{73}Ge^{2+} ions are formed from the ^{73}As atoms located in the cation sublattice of PbSe.

The spectra of the p-type samples with the Ge and GeSe$_2$ absorbers are also individual lines (see figure,

spectra e, f). The spectrum with the Ge absorber has parameters close to the parameters of the type-I spectrum and should be attributed to the ^{73}Ge^0 centers formed from the ^{73}As atoms located in the anion sublattice of PbSe. The spectrum with the GeSe$_2$ absorber (spectrum of type III) has an isomer shift that is expected for the compounds of tetravalent Ge and should be attributed to the ^{73}Ge^{4+} centers formed from the ^{73}As atoms located in the cation sublattice of PbSe.

The ^{73}Ge center in the cation sublattice of PbSe, which corresponds to type II and III spectra, is the iso-electron substitutional impurity. The charge state of this center depends on the conductivity type of the material. In particular, the Ge atoms are stabilized in the Ge^{2+} state in the n-type material and in the Ge^{4+} state in the p-type material. This behavior indicates that the Ge isoelectron impurity in PbSe is electrically active and plays the role of the two-electron donor. For the n-type samples, the spectrum corresponds to the neutral state of the donor center, and for the p-type samples, it corresponds to the doubly ionized state. The absence of resonance absorption in spectra c and d in the figure also indicates that the Ge atoms are electrically active in the cation sublattice of PbSe.

The ^{73}Ge^0 center in the anion sublattice of PbSe, which corresponds to the type-I spectrum, is the antisite defect. Consequently, the isomer shift of type-I spectrum is independent of the conductivity type of the material, and the charge state of the antisite defect is independent of the position of the Fermi level.

It is noteworthy that the widths of all three spectra substantially exceed the doubled natural width of the spectral line ^{73}Ge, i.e., the instrumentation-induced width ~14 μm/s. This fact indicates that the cubic symmetry of the local surrounding of the ^{73}Ge daughter atoms is distorted. This distortion can be caused by the noncentral location of the impurity atom due to the difference in the sizes of the substituted ions (Pb^{2+}, Se^{2-}) and the substituted ions of germanium.

Parameters of the emission Mössbauer spectra at ^{73}As(^{73}Ge) in PbSe

Conductivity type	Absorber	Impurity center	S, μm/s	G, μm/s
n	Ge	^{73}Ge^0	−590	52
	GeSe	^{73}Ge^{2+}	−700	93
	GeSe$_2$	^{73}Ge^{4+}		
p	Ge	^{73}Ge^0	−602	49
	GeSe	^{73}Ge^{2+}		
	GeSe$_2$	^{73}Ge^{4+}	23	73
Errors			±12	±5

Note: S is the location of the centroid of the source relative to the absorber spectrum, and G is the spectral half-width at the half-height.

REFERENCES

1. S. A. Nemov and Yu. I. Ravich, Usp. Fiz. Nauk **168**, 817 (1998) [Phys. Usp. **41**, 735 (1998)].
2. F. S. Nasredinov, S. A. Nemov, V. F. Masterov, and P. P. Seregin, Fiz. Tverd. Tela (St. Petersburg) **41**, 1897 (1999) [Phys. Solid State **41**, 1741 (1999)].
3. S. A. Nemov, P. P. Seregin, Yu. V. Kozhanova, and N. P. Seregin, Fiz. Tekh. Poluprovodn. (St. Petersburg) **37**, 1414 (2003) [Semiconductors **37**, 1367 (2003)].
4. N. P. Seregin, P. P. Seregin, S. A. Nemov, and A. Yu. Yanvareva, J. Phys.: Condens. Matter **15**, 7591 (2003).
5. S. I. Bondarevskiǐ, V. V. Eremin, and N. P. Seregin, in *Basic Research in Technical Universities: Proceedings of V All-Russia Conference on Problems of Science and Higher School* (St. Petersburg, 2001), p. 121 [in Russian].
6. S. A. Nemov, P. P. Seregin, S. M. Irkaev, and N. P. Seregin, Fiz. Tekh. Poluprovodn. (St. Petersburg) **37**, 279 (2003) [Semiconductors **37**, 263 (2003)].

Translated by N. Korovin

Electron Exchange between Neutral and Ionized Germanium Centers in PbSe

E. I. Terukov* and É. S. Khuzhakulov**

*Ioffe Physicotechnical Institute, Russian Academy of Sciences, St. Petersburg, 194021 Russia
**Tashkent Regional State Pedagogical Institute, Angren, 702500 Uzbekistan
Submitted April 12, 2005; accepted for publication April 25, 2005

Abstract—It is shown that the charge state of the antisite ^{73}Ge defect formed in the anion sublattice of PbSe as a result of radioactive transformation of ^{73}As does not depend on the Fermi level position. In contrast, the ^{73}Ge center in the cation sublattice of PbSe is an electrically active substitutional impurity: the electron energy spectrum corresponds to the neutral state of the donor center (Ge^{2+}) in the n-type samples and to the doubly ionized states of this center (Ge^{4+}) in the p-type samples. For partially compensated samples, fast electron exchange between the neutral and ionized donor centers is observed. © 2005 Pleiades Publishing, Inc.

The discovery of superconductivity in the alloys based on lead chalcogenides, whose temperatures of the transition to the superconducting state, T_c, are extraordinarily high [1], has awakened interest in the problem of the behavior of double-electron centers with negative correlation energy in these materials, since the possibility of interpreting the anomalously high T_c values in the context of the bielectron model must not be ruled out [2]. In lead chalcogenides, however, centers with negative correlation energy have not been identified by any direct experimental methods. The sole exception is the tin dopant atoms for which such centers were identified by means of emission Mössbauer spectroscopy for the ^{119}Sn isotope in PbS and PbSe [3].

In this study, emission Mössbauer spectroscopy for the ^{73}As(^{73}Ge) isotope is used to assess the electrical activity of the substitutional germanium dopant in PbSe and to observe the electron exchange between the neutral and ionized states of the Ge donor center.

The radioactive ^{73}As isotope was obtained by the reaction ^{74}Ge(p, 2n)^{73}As. For setting aside the carrier-free ^{73}As preparation, a germanium film that contained ~98% of the ^{74}Ge isotope was irradiated with protons and then kept for three months, following which the film was placed in an evacuated quartz cell whose end, with the target, was heated in a tube furnace at 900 K for five hours. Upon breaking-down the quartz ampoule, ~80% ^{73}As atoms were found to be adsorbed in the inner walls of the cell. The carrier-free ^{73}As preparation was washed off with a solution of nitric acid [4].

The Mössbauer PbSe:^{73}As sources were obtained by fusing the PbSe samples together with the carrier-free ^{73}As preparation and by doping the polycrystalline PbSe samples by diffusion of radioactive ^{73}As in evacuated quartz cells at 700°C. In the samples obtained by fusion, the concentration of the arsenic atoms was ~10^{17} cm^{-3}. Initially, the samples were degenerate and

exhibited either n- or p-type conductivity, with the concentrations of electrons and holes $n \approx 10^{18}$ cm^{-3} and $p \approx 10^{18}$ cm^{-3}, respectively. For the samples doped by diffusion, the initial concentration of holes was $p \approx 10^{18}$ cm^{-3}.

The Mössbauer spectra of ^{73}Ge were recorded using an SM-2201 commercial spectrometer at the temperatures of 80 and 295 K. Since it is impossible to detect the charge states Ge^0, Ge^{2+}, and Ge^{4+} in the same experimental spectrum of ^{73}Ge, the spectra were recorded with the use of different absorbers, such as a single crystal Ge film, a fine-grained crystalline GeSe film, or a fine-grained crystalline GeSe$_2$ film for the spectra corresponding to the Ge^0, Ge^{2+}, or Ge^{4+} centers, respectively. For all of the absorbers, the surface density of the ^{73}Ge isotope was 10 mg/cm^2 and the enrichment with the ^{73}Ge isotope amounted to 90%. The typical spectra of the PbSe:^{73}As source produced by diffusion doping are shown in Fig. 1 for the temperatures of 80 and 295 K. The positions of the centroids of all of the experimental spectra are listed in the table.

At first, we consider the data for the PbSe:^{73}As samples produced by fusion.

The spectra of the n-type sample recorded with the GeSe and Ge absorbers consist of individual lines while, if recorded with the GeSe$_2$ absorber, the spectrum is not observed (see table). With the Ge absorber, the spectrum (type-I spectrum) has a centroid typical of the Ge-based intermetallic compounds and refers to the ^{73}Ge^0 centers located in the anion sublattice of PbSe. In this case, the ^{73}Ge^0 atoms are formed as a result of radioactive decay of the ^{73}As atoms located in the anion sublattice of PbSe. With the GeSe absorber, the spectrum (type-II spectrum) has a centroid typical of the compounds involving divalent germanium and refers to the ^{73}Ge^{2+} centers in the cation sublattice of PbSe (the ^{73}Ge^0 atoms are formed as a result of radioactive decay
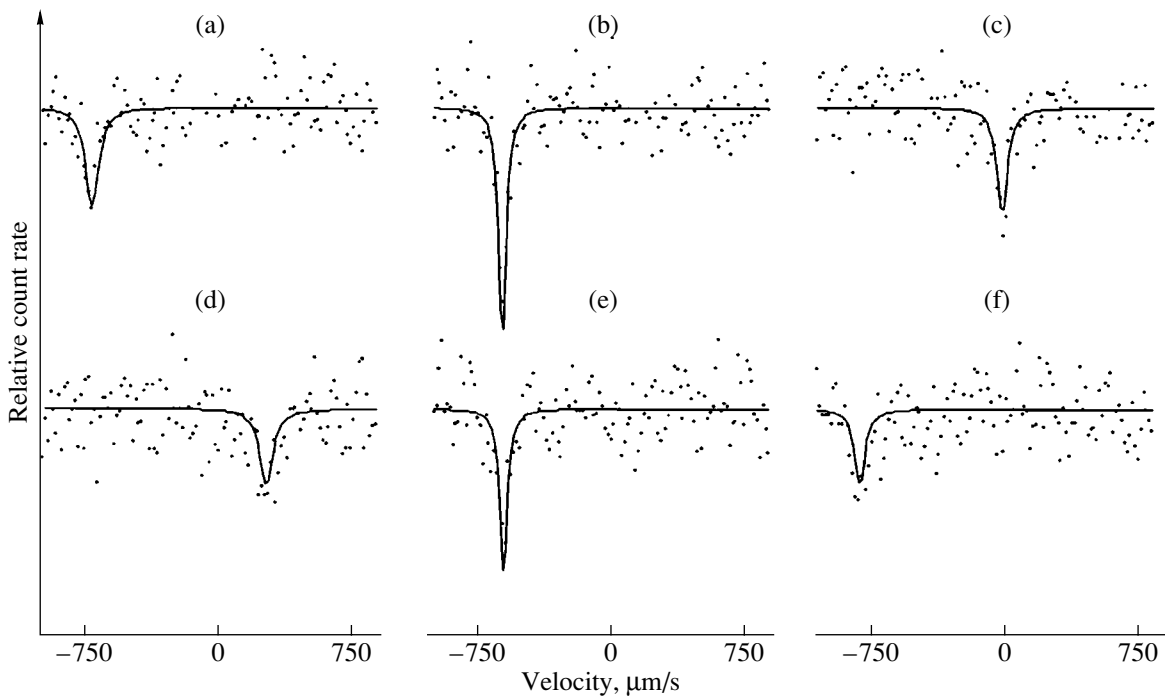
Fig. 1. The emission Mössbauer spectra of the p-PbSe:^{73}As source at (a, b, c) 80 K and (d, e, f) 295 K recorded with the (a, d) ^{73}GeSe, (b, e) ^{73}Ge, and (c, f) ^{73}GeSe$_2$ absorbers.

of the ^{73}As atoms located in the cation sublattice of PbSe). The centroids of all of these spectra vary slightly with temperature.

The spectra of the p-type sample recorded with the Ge and GeSe$_2$ absorbers consist of separate lines as well, while, if recorded with the GeSe absorber, the spectrum is not observed (see table). With the Ge absorber, the spectrum is similar to the type-I spectrum and refers to the ^{73}Ge^0 centers in the anion sublattice of PbSe. With the GeSe$_2$ absorber, the spectrum (type-III spectrum) has a centroid typical of the compounds involving quadrivalent germanium and refers to the

^{73}Ge^{4+} centers in the cation sublattice of PbSe (in this case, the ^{73}Ge^{4+} atoms are formed as a result of radioactive decay of the ^{73}As atoms located in the cation sublattice of PbSe). The centroids of all of these spectra vary slightly with temperature.

The dopant germanium center in the cation sublattice of PbSe (spectra of types II and III correspond to this center) is a substitutional isoelectron dopant. The charge state of this center depends on the type of conductivity of the material, which suggests that this center is a double-electron donor: in the n-type samples, the type-II spectrum corresponds to the neutral state of the

The position of the centroid S of the emission Mössbauer spectra for PbSe: ^{73}As at 80 and 295 K

Source. Method of synthesis	Absorber	Type of spectrum	Dopant center	S, μm s^{-1}, 80 K	Figure	S, μm s^{-1}, 295 K	Figure
n-PbSe: ^{73}As, fusio	Ge	I	^{73}Ge^0	−590		−580	
	GeSe	II	^{73}Ge^{2+}	−700		−695	
	GeSe$_2$		^{73}Ge^{4+}				
p-PbSe: ^{73}As, fusion	Ge	I	^{73}Ge^0	−602		−595	
	GeSe		^{73}Ge^{2+}				
	GeSe$_2$	III	^{73}Ge^{4+}	23		73	
p-PbSe: ^{73}As, diffusion	Ge	I	^{73}Ge^0	−615	1b	−605	1e
	GeSe	II	^{73}Ge^{2+}	−722	1a	270	1d
	GeSe$_2$	III	^{73}Ge^{4+}	42	1c	−762	1f
Errors, %				±12		±10	

center, and in the *p*-type samples, the type-III spectrum corresponds to the doubly ionized state of the center. The lack of the spectra for the *n*-type sample with the $GeSe_2$ absorber and for the *p*-type sample with the GeSe absorber suggests that germanium atoms in the cation sublattice of PbSe are electrically active. The Ge dopant center in the anion sublattice of PbSe (type-I spectrum) is an antisite defect. As follows from the independence of the isomer shift of the type I spectrum from the type of conductivity of the material, the charge state of the antisite defect does not depend on the position of the Fermi level.

We now consider the data for the $PbSe{:}^{73}As$ samples produced by diffusion doping.

Under the conditions of diffusion annealing, the selenium content, i.e., the position of the Fermi level, changed. The duration of annealing was chosen so that the Mössbauer spectra involved the lines of divalent and quadrivalent germanium simultaneously. This means that, in this case, the Fermi level was in the energy region close to the germanium levels.

The spectra recorded with the Ge absorber (type-I spectra) consist of separate lines (see Figs. 1b, 1e) and should be ascribed to the $^{73}Ge^0$ centers in the anion sublattice of PbSe. The centroid of the type-I spectrum varies only slightly with temperature (see table). The spectra recorded with the GeSe (type-II spectra, Figs. 1a, 1d) and $GeSe_2$ absorbers (type-III spectra, Figs. 1c, 1f) consist of separate lines as well. The lines should be assigned to the electrically active germanium donor centers in the cation sublattice of PbSe. With increasing temperature, the lines of the $^{73}Ge^{2+}$ and $^{73}Ge^{4+}$ states approach each other, which suggests an increase in the rate of electron exchange between the neutral and ionized germanium centers with temperature.

It should be noted that a similar effect was observed for the tin dopant atoms in intrinsic PbSe [2]. However, the degree of convergence of the Mössbauer spectral lines for ^{119}Sn was much larger than that for ^{73}Ge. In other words, the frequency of electron exchange increases more steeply for the tin dopants than for the germanium dopants.

REFERENCES

1. S. A. Nemov, R. V. Parfeniev, D. V. Shamshur, *et al.*, Physica C (Amsterdam) **333**, 31 (2000).
2. S. A. Nemov and Yu. I. Ravich, Usp. Fiz. Nauk **168**, 817 (1998) [Phys. Usp. **41**, 735 (1998)].
3. N. P. Seregin, P. P. Seregin, S. A. Nemov, and A. Yu. Yanvareva, J. Phys.: Condens. Matter **15**, 7591 (2003).
4. S. I. Bondarevskiĭ, V. V. Eremin, and N. P. Seregin, in *Proceedings of International Conference on Ecological Problems and Ways of Their Solution in XXI Century: Education, Science, Engineering* (St. Petersburg, Russia, 2000), p. 82.

Translated by É. Smorgonskaya

Characterization of Photonic Crystals Based on Opal–Semiconductor Composites by Bragg Reflection Spectroscopy

G. M. Gadzhiev*, V. G. Golubev, D. A. Kurdyukov**, A. B. Pevtsov**,
A. V. Sel'kin**, and V. V. Travnikov**^**

*Institute of Physics, Dagestan Scientific Center, Russian Academy of Sciences, Makhachkala, 367003 Russia
**Ioffe Physicotechnical Institute, Russian Academy of Sciences, St. Petersburg, 194021 Russia
^e-mail: travn@spectr.ioffe.ru
Submitted April 25, 2005; accepted for publication May 4, 2005

Abstract—The Bragg reflection spectra of photonic crystals based on the opal–semiconductor (GaP, GaN) composites are studied. An approach is developed which provides a means for characterizing the opal-like structures. The approach is based on examination of the Bragg reflection spectral features and of the conditions for multiwave Bragg diffraction. The shape of the Bragg spectra is analyzed in the context of the approximation of a periodic planar-layered medium taking into account sintering and axial compression of the a-SiO$_2$ spheres that constitute the three-dimensional opal lattice. The diameters and the coefficient of compression of the spheres are determined with regard to the spectroscopic structural invariant suggested in the study for defining the conditions for observation of multiwave Bragg diffraction at the system of the {111} planes. © 2005 Pleiades Publishing, Inc.

1. INTRODUCTION

Photonic crystals are spatially periodic structures in which the permittivity is modulated with a period comparable with the wavelength of light. Special interest in these crystals is motivated by new possibilities of controlling the light that appear due to the photonic band gaps (PBGs) in the corresponding structures [1]. Particular attention is focused on the photonic crystals with three-dimensional (3D) translation symmetry, since it is these crystals that make it possible to gain a full PBG energy range in which light propagation is impossible for all directions inside the photonic crystals [2].

Among the 3D photonic crystals, the opal–semiconductor composites are of particular importance [3]. The spatial structure of these composites is defined by the symmetry of opals. The face-centered cubic (fcc) lattice of opals consists of closely packed amorphous silicon oxide (a-SiO$_2$) spheres. Between the (a-SiO$_2$) spheres, there exists a sublattice of voids accessible to impregnation with foreign materials. Introduction of various semiconductors into the voids provides a means for producing photonic crystals, in which the properties of the 3D structure of opal can be combined with the optical and electrical properties of semiconductors. The voids can be filled with different semiconductors, and the degree of filling can be varied to provide the conditions for appropriate changes in the properties of the photonic crystals. By etching the a-SiO$_2$ spheres to remove them from the composites, the inverted structures, which consist of only the semiconductor materials, can be produced.

As a rule, the semiconductor materials in the voids of opals are synthesized at rather high temperatures. Heating of the samples can be accompanied by additional sintering of the a-SiO$_2$ spheres (an increase in the intersphere contact area) and by changes in their shape (e.g., transformation of the spheres into ellipsoids). As a result of anisotropic sintering and deformation of the spheres, the point symmetry and, hence, the optical properties of the photonic crystals can change [4–6]. In addition, one should expect manifestations of frequency dispersion of the permittivity of the semiconductor introduced in the voids in the optical properties of the synthesized structures, especially in the spectral range of the fundamental absorption edge of the built-in material. In this context, a demand arises for a closer examination of the mechanisms of formation of the optical spectra of the opal–semiconductor composites taking into account the dielectric properties of the semiconductors and the possible modification of the fcc structure of the opals.

In this paper, we demonstrate new possibilities for predicting the properties of the photonic-crystal structures. The diagnostics involves studies of the spectra of Bragg reflection (BR) from the opal–semiconductor composites. The experimental data are analyzed taking into account the optical properties of the semiconductors and possible strain-induced changes in the fcc lattice of the opal matrix. We study artificial opals with voids in which the wide-gap GaN and GaP semiconductors are synthesized and inverted structures consisting only of GaN.
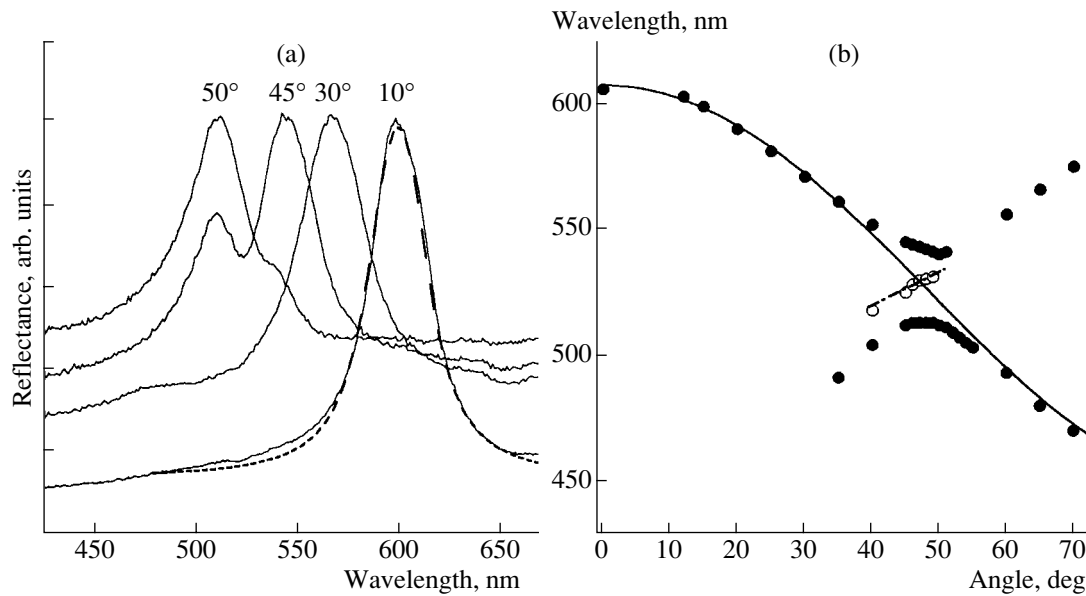
Fig. 1. The opal–GaN composites. (a) Experimental Bragg reflectance spectra at different angles of incidence (solid lines) and the theoretical reflectance spectrum at the angle of incidence 10° (dashed line). (b) The angular dependence of the spectral position of the Bragg reflectance peaks (closed circles), the spectral positions of the minima of the doublets (open circles), and the calculated peak positions of the Bragg reflectance at the (111) planes parallel to the sample surface (solid line).

2. EXPERIMENTAL

The initial matrices for fabrication of the photonic crystals were synthetic opals in which the voids between the spheres can account for up to a 26% fraction of the total volume. The diameter of the spheres was about 260–270 nm, as preliminarily estimated from the measurements using a scanning electron microscope. The samples to be studied were prepared as wafers ~5 × 5 × 0.5 mm in size. The wafers were cut in such a way that the face of the sample with a larger area was the reflecting (111) surface. The semiconductors were synthesized directly in the voids of the opal according to technology similar to that described in [7–9]. The temperature of synthesis was 950°C for GaN and 800°C for GaP. For producing the inverted structures, the opal matrix was etched off from the composite using an aqueous solution of hydrofluoric acid.

The examination of the BR spectra is one of the simplest direct methods of study of the band structure of photonic crystals. The peaks of reflectance arise as a result of the Bragg diffraction of light at the families of crystallographic planes of the photonic crystal and correspond to the photon energies and wave vector directions for which light propagation inside the ideal photonic crystal is forbidden. The important characteristic of a photonic crystal is its PBG ΔE_{gap}. This parameter depends on the amplitude of spatial modulation of the permittivity depending, in turn, on the dielectric contrast of the constituent materials of the photonic crystal. For sharp-contrast structures, the PBG ΔE_{gap} is evaluated sometimes from the experiment as the width ΔE at the half-maximum of the BR band [10]. In order to

compare the photonic-crystal properties of different composites, it is convenient to use the relative width of the reflectivity band, $\Delta E/E_0$, measured in the case of normal incidence of light on the system of the corresponding crystallographic planes (E_0 is the energy corresponding to the peak position in the reflectance spectrum).

The BR spectra of the samples are shown in Figs. 1a, 2a, and 3a. The spectra are recorded in the s light polarization at different angles of incidence measured with respect to the normal to the sample (111) surface. In the spectral measurements, the samples were oriented so that the wave vectors of the incident light and reflected light were lying in the plane that goes through the Γ, U, L, and K points of the Brillouin zone of the fcc lattice.

The introduction of semiconductors into the voids of opals with a sufficiently high degree of filling involves an increase in the dielectric contrast. As a result, the PBG becomes wider; consequently, the relative width of the observed reflectance bands increases. In the case of normal incidence of light, the relative width $\Delta E/E_0$ is 0.047 for the pure opal, 0.051 for the opal–GaN composite, 0.11 for the inverted GaN opal, and 0.16 for the opal–GaP composite. The character of the angular dependence of the BR spectra of the composites is substantially modified compared to those of the initial opals. In the reflectance spectra of the opal–GaN composite and the inverted structure obtained on its basis, additional peaks located at shorter wavelengths appear with an increasing angle of incidence θ (at angles close to $\theta \approx 30°$), as shown in Figs. 1 and 2. The intensity of these peaks increases gradually with θ, so that, in the range of $\theta \approx 35°$–55°, the spectra take the
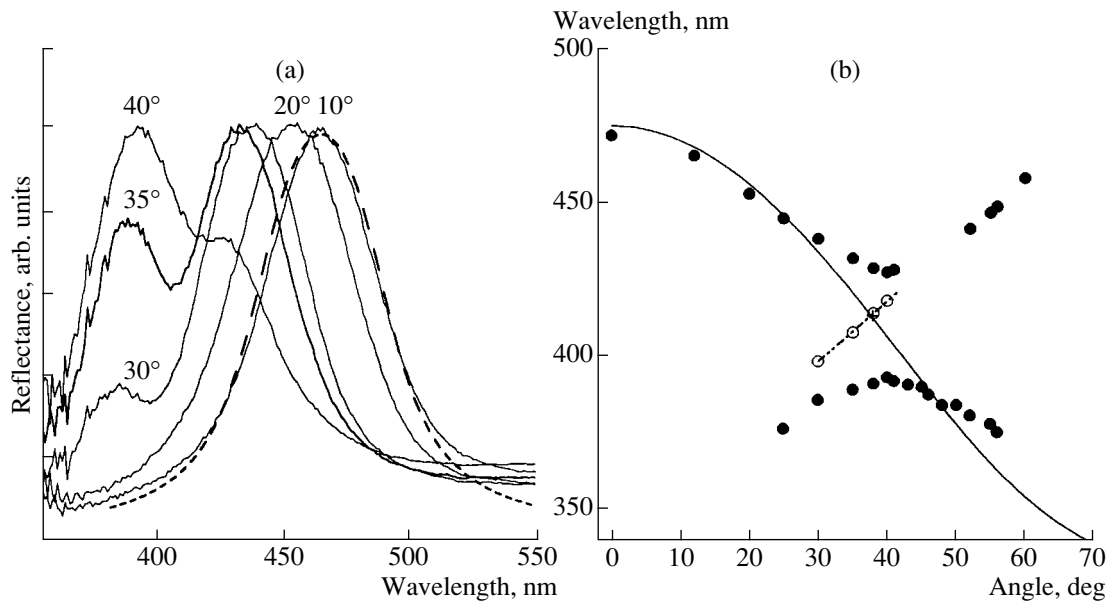
Fig. 2. The GaN-based inverted structures. (a) Experimental Bragg reflectance spectra at different angles of incidence (solid lines) and the theoretical reflectance spectrum at the angle of incidence 10° (dashed line). (b) The angular dependence of the spectral position of the Bragg reflectance peaks (closed circles), the spectral positions of the minima of the doublets (open circles), and the calculated peak positions of the Bragg reflectance at the (111) planes parallel to the sample surface (solid line).

shape of a well-pronounced doublet. As the angle of incidence increases further, the intensity of the peak at longer wavelengths decreases, and only the peak (at shorter wavelengths) remains in the spectra. The dependences of the spectral position of the BR peaks on the angle of incidence (Figs. 1b, 2b) can be divided into two branches separated from each other by the "avoiding crossing area" [11].

For the opal–GaP composites, the major peaks in the angular range up to $\theta \sim 70°$ shift only slightly closer to each other. In this case, the reflectance bands observed at the minimal and maximal angles θ overlap appreciably (see Fig. 3).

For analyzing the angular dependences of the BR peak positions, the well-known Bragg formula

$$\lambda = 2d_{111}\sqrt{\varepsilon_0 - \sin^2\theta} \tag{1}$$

is commonly used. Here, λ is the wavelength corresponding to the reflectance peak, d_{111} is the period of the crystal lattice along the [111] direction, θ is the angle of incidence, and ε_0 is the average permittivity of

the opal-like structures. The permittivity ε_0 is defined by the permittivities ε_a and ε_b of the materials of spheres and voids, respectively, and by the factor of filling of the structure with the spheres, f_0:

$$\varepsilon_0 = \varepsilon_a f_0 + \varepsilon_b(1 - f_0). \tag{2}$$

The value of f_0 can vary from sample to sample because of different degrees of sintering of the spheres with each other in different samples. At the same time, to make the structure sufficiently rigid, the filling factor f_0 should be larger than $f_{00} \approx 0.74$, which is the filling factor for the closely packed fcc structure of spheres in point contact.

In Figs. 1b, 2b, and 3b, solid lines are plotted using formula (1) with the corresponding parameters listed in the table (see below). In contrast to the case of pure opals [12], the angular dependences of the spectral position of the BR peaks for the composite structures differ substantially from the dependences calculated by formula (1).

The doublet structure appearing in the reflectance spectra in the case of inclined incidence is due to mul-

Table

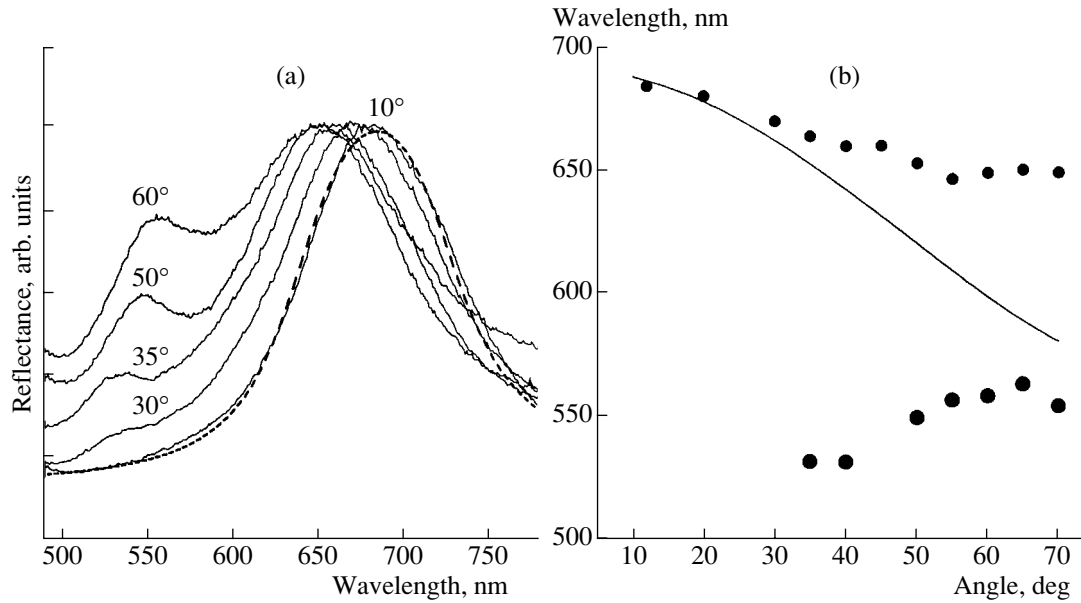| Sample	Experimental data			Adjustable parameters					
	λ_*, nm	θ_*, deg	$\Delta E/E_0$	a_{00}, nm	χ	η	f_m	ε''	$\Delta E_{gap}/E_0$
Opal–GaN	530	47	0.063	277	0.05	0.90	0.67	0.092	0.051
Inverted opal–GaN	413	38	0.117	271	0.05	0.91	0.7	0.090	0.11
Opal–GaP	–	–	0.174	271	0.03	0.92	0.87	0.24	0.126

Fig. 3. The opal–GaP composites. (a) Experimental Bragg reflectance spectra at different angles of incidence (solid lines) and the theoretical reflectance spectrum at the angle of incidence 10° (dashed line). (b) The angular dependence of the spectral position of the Bragg reflectance peaks (closed circles) and the calculated peak positions of the Bragg reflectance at the $(\bar{1}11)$ planes parallel to the sample surface (solid line).

tiwave Bragg diffraction (MBD), i.e., simultaneous diffraction at the system of at least two intercrossing crystallographic planes [11]. The effects of multiwave X-ray diffraction were previously studied in detail for conventional (atomic) crystals [13]. In photonic crystals, the interaction of the electromagnetic field with the 3D periodic medium is enhanced due to the sharper dielectric contrast and, as a consequence, deeper modulation of the permittivity. The observed deviation of the angular dependence of the BR peak positions from the dependence described by Bragg's formula (1) is apparently due the MBD effects. Thus, the MBD effects limit the potential of characterizing the opal–semiconductor composites by relation (1).

3. THEORETICAL MODEL

In describing the experimental BR spectra, we consider a photonic crystal as a 3D lattice, with dielectric spheres located at the sites. The model involves the effects of sintering (interpenetration) of the structural units, i.e., spheres, and their possible axial deformation along the [$\bar{1}11$] direction of structural growth. Because of this deformation, the spheres are transformed into ellipsoids.

We denote the axes of the ellipsoids as $D_\parallel$ and $D_\perp$, assuming that the ellipsoids are spheroids in shape. Let the axis $D_\parallel$ be the rotational axis orthogonal to the reflecting surface of the structure. The distance a_{00} between the centers of neighboring spheroids in point contact, which are located in the lateral plane, is $D_\perp$. The period of the structure along the direction orthogo-

nal to the surface, L, is defined as $L = d_{111} = \sqrt{2/3}\, D_\parallel$. As a result of interpenetration (sintering) of the spheroids, the distance a_{00} decreases by the quantity Δa_{00} and the period L, by the quantity ΔL. If the relative changes in the parameters a_{00} and L are characterized by the sintering factor $\chi = \Delta a_{00}/D_\perp = \Delta L/L$ (isotropic sintering), the factor of filling of the structure with spheroids, f_0, in the case of not-so-hard sintering, takes the following form [14]:

$$f_0 = \frac{\pi}{3\sqrt{2}} \frac{1 - 3\chi^2(3 - \chi)}{(1 - \chi)^3}. \qquad (3)$$

Due to the ellipsoidal shape of the structural units of the lattice, the O_h symmetry of the structure is reduced to the D_{3d} symmetry. This corresponds to axial strain of the cubic lattice along the [$\bar{1}11$] direction (parallel to the normal to the surface in the case under consideration). Such strain can be described quantitatively by the coefficient of anisotropic compression $\eta = D_\parallel/D_\perp$.

The BR spectra were calculated theoretically in the approximation of a periodic planar-layered medium [14–16]. In the context of this approximation, the periodic 3D medium is considered as a continuous medium in the XY plane parallel to the outer layer of spheres (orthogonal to the [$\bar{1}11$] direction aligned with the z axis), with the permittivity averaged over the XY plane. Since the averaging is carried out only over the coordinates X and Y, the permittivity becomes the periodic function $\varepsilon_s(Z)$ of only one spatial variable Z.

In the model, the surface effects were accounted for by truncating the outer spheroids and by formulating the Maxwell boundary conditions for the cutting planes

at the front (v) and the rear surfaces (u) of the photonic-crystal wafer. In order to describe these effects quantitatively, we introduced the cut-off coefficients $\zeta_v = 2\Delta l_v/D_\parallel$ and $\zeta_u = 2\Delta l_u/D_\parallel$, where Δl_v and Δl_u are the shifts of the cutting planes with respect to the outer planes tangent to the outer spheroids before cutting.

The observed reflectance bands span a considerable part of the visible spectrum, in which the permittivities of the GaP and GaN semiconductors introduced in the structures vary noticeably with frequency. For this reason, when calculating the permittivity profiles $\varepsilon_s(Z)$, we used the data on the frequency dependences $\varepsilon_m = \varepsilon_m(\omega)$ of these materials [17, 18]. In addition, we accounted for the possibility of incomplete filling of the voids of opals with the semiconductor material. This was done by introducing the volume fraction of the material in the voids, f_m, and by calculating the effective permittivity of the voids, $\varepsilon_b = \varepsilon_{\text{eff}}$, in the Maxwell–Garnett approximation [19]. This approximation implies a statistically uniform filling of the voids with foreign nanoclusters. The permittivity of the a-SiO$_2$ spheres in the opal–semiconductor composites was taken as $\varepsilon_a = 1.98$ [16]. For the inverted structure, we assumed $\varepsilon_a = 1$ (the permittivity of free space). In order to take into account in the theory the hardly controllable absorption and scattering processes, which are unavoidable because of imperfections in the samples, the imaginary part ε'' was added to the permittivity $\varepsilon_s(Z)$.

The reflectance spectra were calculated quantitatively by the method of the transfer matrix, with the filling function approximated by a stepwise function: within each period L, the dielectric medium was considered as a multilayered structure, which consisted of a system of N ($N > 100$) uniform dielectric sublayers identical in thickness. In the calculations, the quantities a_{00}, η, χ, f_m, ε'', and ζ_v were used as the parameters of the problem (since we considered bulk samples, the influence of their rear surface and hence the quantity ζ_u was negligible).

The doublet structure of the BR spectra observed in the case of inclined incidence of light is related to the MBD at the system of intercrossing crystal planes [11]. In the situation under consideration, the basic system of planes is the set of (111) planes of growth that are parallel to the PC surface. The other planes involved in the MBD cross the planes of growth at some angle. The crystal planes from the {111} set that are not parallel to the sample surface can serve as such inclined planes (denoted by ($\bar{1}11$)). It is the conditions of resonant scattering at the (111) and ($\bar{1}11$) planes in combination that provide the multiwave character of Bragg diffraction in the spectral region of the lowest PBG of the opal-like photonic crystal [14].

If the modulation of the permittivity is negligible (the "empty" lattice approximation), the dispersion relations for the Bloch modes are written as

$$\omega = (c/\sqrt{\varepsilon_0})\sqrt{(\mathbf{K} - \mathbf{G}_{hkl})^2}, \tag{4}$$

where $\mathbf{K}$ is the Bloch wave vector and $\mathbf{G}_{hkl}$ ($|\mathbf{G}_{hkl}| \equiv G_{hkl}$) are the vectors of the reciprocal lattice with the indices hkl commonly introduced to describe the systems of "atomic" (hkl) planes. Simultaneous solution of Eqs. (4) for diffraction with regard to the umklapp processes for the wave vector, i.e., changes in the wave vector by the vectors of the reciprocal lattice $\mathbf{G}_{000} = 0$ and $\mathbf{G}_{111}$ ($|\mathbf{G}_{111}| \equiv G_{111}$), yields the component of $\mathbf{K}$ along the [111] direction (Z axis)

$$K_Z = G_{111}/2, \tag{5}$$

which defines Bragg's law (1) with the period $d_{111} = a_{00}\eta\sqrt{2/3}$.

At certain angles of incidence θ, the Bloch mode $\omega = \omega_{\bar{1}11}(K_Z)$ formed by the inclined ($\bar{1}11$) planes is mixed, due to the periodic modulation of $\varepsilon(\mathbf{r})$ along the [$\bar{1}11$] direction, with the damped Bloch states $\omega = \omega_{111}(K_Z)$ within the "111" PBG. As a result, Bragg's law breaks down at $K_Z \approx G_{111}/2$, and the energy spectrum is renormalized, so that the states related to the energy transfer inside the crystal appear in the vicinity of $\omega = \omega_{\bar{1}11}(G_{111}/2)$. As a consequence, a sharp decrease in the reflectance occurs at and around this frequency. This decrease is responsible for the gap in the BR band and hence for the doublet structure of the spectrum [14].

The most pronounced deviation from condition (1) occurs at the angle of incidence θ_* such that the dispersion curve for the mode $\omega = \omega_{\bar{1}11}(K_Z)$ intersects precisely the middle of the "111" PBG. The wavelength λ_* corresponding to the intersection point is defined by the expression [14]

$$\lambda_* = \frac{4a_{00}\sqrt{3}}{4 - \eta^{-2}}\sin\theta_*. \tag{6}$$

The values of λ_* and θ_* can be determined from the experiment, approximating the angular shift of the reflectance peaks at small angles of incidence ($\theta < 45°$) by Bragg's relation (1) and then extrapolating the theoretical curve (1) to the range of $\theta \approx \theta_*$. Then the intersection of Bragg's curve (1) with the experimental curve that describes the dependence of the gap position in the doublet structure of the reflectance spectrum on the angle of incidence should correspond to the values of λ_* and θ_* [20]. When analyzing the experimental spectra, we used precisely this method of determination of λ_* and θ_*. The resulting values of λ_* and θ_* for all of the samples are listed in the table. Evaluation of λ_*

and θ_* from the MBD spectra provides a means for additional structural characterization of photonic crystals. It should be emphasized that relation (6) used here is, in essence, a spectroscopic structural invariant for a photonic crystal.

4. DISCUSSION

Figures 1a, 2a, and 3a (dashed lines) show the theoretical spectra for small (10°) angles of incidence of light. The calculations were carried out with variations in the basic parameters of the theory a_{00}, η, χ, f_m, ε'', and ζ_v. It should be noted that, in fitting the theory to the experimental data, it was possible to obtain only one optimal set of the above parameters, since the analysis of the experimental curves required that a rather large body of qualitative and quantitative characteristics of the spectra be correlated in the context of one unified model. The parameters that provide the best fit of the theory to the experiment are listed in the table.

The planar approximation used for describing quantitatively the experimental spectra corresponds to the model of a one-dimensional photonic crystal. In the context of this approximation, the analysis of the BR spectra does not allow for finding the parameters a_{00} and η separately. By fitting of the BR spectra, we can determine only the spatial period $d_{111} = a_{00}\eta\sqrt{2/3}$ that involves the product $a_{00}\eta$. In order to determine the values of a_{00} and η separately, we used the structural invariant (6) that defines a relation between η and the experimentally measured quantities λ_* and θ_*. Thus, the MBD study presents a unique way of characterizing the actual 3D structure of photonic crystals.

The observed reflectance bands noticeably differ from each other in shape and, in particular, in the character of the asymmetry, i.e., in the relationship between the BR intensities in the long- and short-wavelength parts of the reflectance bands. In the calculations, the band asymmetry can be varied by varying the factor ζ_v that efficiently accounts for the influence of the boundary conditions on the spectra.

The calculated values of the parameter η suggest a rather strong anisotropic compression of the a-SiO$_2$ spheres. As already mentioned, such compression results in a change in the symmetry of the fcc lattice of the opal-like photonic crystals and can substantially affect the features of the band structure established for these photonic crystals to date (see, e.g., [21]).

The sintering factors χ for opals impregnated with semiconductors are larger than the corresponding factors for the initial opals. The maximum value of χ for the opal–GaN composite is most likely due to the highest temperature of synthesis (~950°C). This should result in the highest degree of penetration of the spheres into each other.

The calculated values of the parameter f_m suggest that the degree of filling of the voids of the opals is above 50%. With such a degree of filling and with the technology used here [7–9], the deposition of the semiconductor as continuous films on the surface of the a-SiO$_2$ spheres [22] is improbable. As a result, the model of statistically uniform filling of the voids by the nanoclusters of the introduced material, as assumed in the calculations, is reasonably justified.

In the table, the relative widths $\Delta E_{gap}/E_0$ evaluated from the calculations for the samples at the angle of incidence 10° are presented. The values of ΔE_{gap} were determined from the calculations as the frequency regions in which the reflectivity was 100% at $\varepsilon'' = 0$. The calculated widths $\Delta E_{gap}/E_0$ and the experimentally measured widths $\Delta E/E_0$ are in good agreement. Thus, the PBG width can be determined with a satisfactory accuracy by measuring the width of the BR band at the half-maximum.

As mentioned above, the angular dependence of the BR spectra of the opal–GaP photonic crystal is substantially different from the data for the other composites. This gives no way, in particular, for determining the quantities λ_* and θ_* from the experiment. The experimentally measured values of λ_* and θ_* correspond to relations (1) and (6) satisfied together. Since the maximum external angle θ cannot be larger than 90°, the value of ε_0 corresponding to the conditions of the invariant (6) is found to be limited (see [14]). In the case of $\eta = 1$, the maximum value $\varepsilon_0 = 3$ corresponds to the condition that the combined diffraction at the parallel and inclined {111} planes occurs in the conditions of grazing external incidence. For $\varepsilon_0 > 3$, Bragg's conditions for these sets of planes can be satisfied in combination only for the waves excited by some sources inside the crystal. For the opal–GaP composite, $\varepsilon_0 \approx 3$, and the conditions for MBD cannot be satisfied, at least with the angles of incidence used in the experiments ($\theta < 70°$).

5. CONCLUSIONS

In this study, the BR spectra of three-dimensional photonic crystals based on opal–semiconductor composites are examined. Spectroscopic methods are suggested for characterization of the composites, including the determination of their optical and geometric parameters. The characterization is based on the analysis of the shape of the BR spectra and on the use of spectroscopic structural invariants controlled by multiwave diffraction in the opal-like structures. The BR spectral contours are analyzed in the context of the approximation of a periodic planar-layered medium, with the permittivity averaged along the directions parallel to the surface. The analysis is carried out with regard to the special features of the opal-like structures, such as sintering of the constituent a-SiO$_2$ spheres and axial compression of these spheres. The planar approximation makes it possible to estimate the period of the photonic crystal only in the direction orthogonal to the surface. The period depends on both the diameter and the degree of compression of the a-SiO$_2$ spheres. The values of the

diameters of the spheres and of the degree of anisotropic compression are determined from the relations that define the conditions for resonant multiwave diffraction at the sets of crossing {111} planes (parallel and inclined to the sample surface).

ACKNOWLEDGMENTS

REFERENCES

1. *Photonic Crystals and Light Localization in the 21st Century*, Ed. by C. M. Soukoulis (Kluwer, Dordrecht, 2001), NATO Adv. Study Inst. Ser., Ser. C: Math. Phys. Sci., Vol. 563.

2. K. M. Ho, C. T. Chan, and C. M. Soukoulis, Phys. Rev. Lett. **65**, 3152 (1990).

3. V. N. Astratov, V. N. Bogomolov, A. A. Kaplyanskii, *et al.*, Nuovo Cimento D **17**, 1349 (1995).

4. A. Reynolds, F. López-Tejeira, D. Cassgne, *et al.*, Phys. Rev. B **60**, 11422 (1999).

5. G. Subramanta, R. Biswas, K. Konstant, *et al.*, Phys. Rev. B **63**, 235111 (2001).

6. K. P. Velikov, T. van Dillen, A. Polman, and A. van Blaaderen, Appl. Phys. Lett. **81**, 838 (2002).

7. V. Yu. Davydov, V. G. Golubev, N. F. Kartenko, *et al.*, Nanotechnology **11**, 291 (2000).

8. G. Gajiev, V. G. Golubev, D. A. Kurdyukov, *et al.*, Phys. Status Solidi B **231**, R7 (2002).

9. G. M. Gadzhiev, V. G. Golubev, M. V. Zamoryanskaya, *et al.*, Fiz. Tekh. Poluprovodn. (St. Petersburg) **37**, 1449 (2003) [Semiconductors **37**, 1400 (2003)].

10. M. S. Thijssen, R. Sprik, J. E. G. Wijnhoven, *et al.*, Phys. Rev. Lett. **83**, 2730 (1999).

11. H. M. van Dril and W. Vos, Phys. Rev. B **62**, 9872 (2000).

12. C. Lopez, A. Blanco, H. Miguez, and F. Meseguer, Opt. Mater. **13**, 187 (1999).

13. S.-L. Chang, *Multiple Diffraction of X-rays in Crystals* (Springer, Berlin, 1984; Mir, Moscow, 1987).

14. A. V. Sel'kin, in *Proceedings of 12th International Symposium on Nanostructures: Physics and Technology* (St. Petersburg, Russia, 2004), p. 111.

15. Yu. A. Vlasov, M. A. Kaliteevski, and V. V. Nikolaev, Phys. Rev. B **60**, 1555 (1999).

16. G. Golubev, D. A. Kurdyukov, A. B. Pevtsov, *et al.*, Fiz. Tekh. Poluprovodn. (St. Petersburg) **36**, 1122 (2002) [Semiconductors **36**, 1043 (2002)].

17. D. E. Aspnes and A. A. Studna, Phys. Rev. B **27**, 985 (1983).

18. G. Yu, G. Wang, H. Ishikawa, *et al.*, Appl. Phys. Lett. **70**, 3209 (1997).

19. J. S. Maxwell Garnett, Philos. Trans. R. Soc. London **203**, 385 (1904).

20. A. V. Sel'kin, A. Yu. Bilibin, A. Yu. Men'shikova, *et al.*, in *Proceedings of Conference on Fundamental Problems in Optics-2004* (St. Petersburg, 2004), p. 97.

21. J. F. Galisteo-Lopez, F. Garsia-Santamaria, D. Golmayo, *et al.*, Photon. Nanostruct. Fundam. Appl. **2**, 117 (2004).

22. F. Garsia-Santamaria, M. Ibisate, I. Rodrigues, *et al.*, Adv. Mater. **15**, 788 (2003).

Translated by É. Smorgonskaya

On the Effect of Transverse Quantum Confinement on the Electrical Characteristics of a Submicrometer-Sized Tunnel MOS Structure

M. I. Vexler, I. V. Grekhov^, and A. F. Shulekin

Ioffe Physicotechnical Institute, Russian Academy of Sciences, St. Petersburg, 194021 Russia
^e-mail: mega@pulse.ioffe.rssi.ru
Submitted March 10, 2005; accepted for publication March 25, 2005

Abstract—The changes in the characteristics of the Al/SiO$_2$/n-Si MOS structure as a result of a decrease in its transverse dimensions in the range from micrometers to several nanometers are studied. The characteristics are simulated with regard to quantum confinement of the motion of carriers in the plane orthogonal to the direction of tunneling. For making the model more illustrative, the MOS structure is considered as an injector (tunnel MOS emitter) of a bipolar transistor. It is shown that the reduction in size does not produce radical changes in the electrical characteristics of the device, but results in some decrease in the collector current and, most notably, in the gain. The results are important as such and, at the same time, in the context of scaling of field-effect transistors, since the transistor involving a tunnel MOS emitter provides one of the practically interesting operation modes of the conventional field-effect transistor. © 2005 Pleiades Publishing, Inc.

1. INTRODUCTION

The adoption of extremely thin dielectric layers is one of the conditions for miniaturization of the components of submicrometer-scale integrated circuits [1]. As was shown by Momose *et al.* [2], quantum-mechanical tunneling through the gate insulator does not impose a principal restriction that excludes the use of thin dielectric layers appropriate for tunneling in metal–oxide–semiconductor field-effect transistors (MOSFETs).

However, the tunneling current through the dielectric, i.e., the gate current, presents a phenomenon to be studied in detail. Actually, tunneling causes an increase in standby power consumption, losses in the transistor channel, and an acceleration of degradation. As a result, quantitative description of the behavior of the structure becomes more difficult.

When studying the charge transport through the insulator (e.g., when testing the stability of the oxide) in field-effect transistors (FETs), researchers commonly try to provide conditions for a uniform gate current flow. For this purpose, the drain is connected to the source, and gate-to-substrate and gate-to-source voltages are applied. The application of voltage only to the substrate is inadequate to satisfy the above conditions, since no inversion can be attained because of the tunnel leakage of minority carriers (see, e.g., [3]).

If we are dealing with a structure involving an appropriate-for-tunneling thin dielectric layer (2–3 nm thick) on an *n*-Si wafer, the FET operates, under the above-indicated conditions, in fact as a bipolar transistor with a tunnel MOS emitter, although this fact is typically not mentioned. The gate serves as an emitter, the substrate as a collector. The drain and source are contacts to the induced base. The gain depends on the degree of asymmetry of tunneling of electrons (majority carriers) and holes. The base current is the current that flows through the source–drain to maintain the proper biases at the terminals.

Bipolar transistors with tunnel MOS emitters have already been known for a rather long time [4] and, with large-sized emitters, have been studied in detail [4, 8]. Until recently, however, these transistors were studied separately from FETs in which thicker dielectric layers were used. In the present new situation, the study of bipolar tunnel transistors becomes interesting also for better understanding of the processes in FETs.

The aim of this study is to investigate how the characteristics of a tunnel MOS structure are modified when the linear dimension L of the structure is decreased in the submicrometer region. The modifications can be due to the effect of quantum confinement on the motion of carriers in the plane orthogonal to the direction of tunneling.

2. MODEL: GENERAL DESCRIPTION

For definiteness, we concentrate on the behavior of the Al/SiO$_2$/n-Si MOS structure fabricated as a mesa of an $L \times L$ section. The oxide thickness is taken to be $d = 2.5$ nm (Fig. 1). The dimension L is not presumed to be large, so that, in general, the quantum-confinement effect in the transverse xy plane should not be disregarded. The positive (collector) voltage $V = U_{CE}$ is
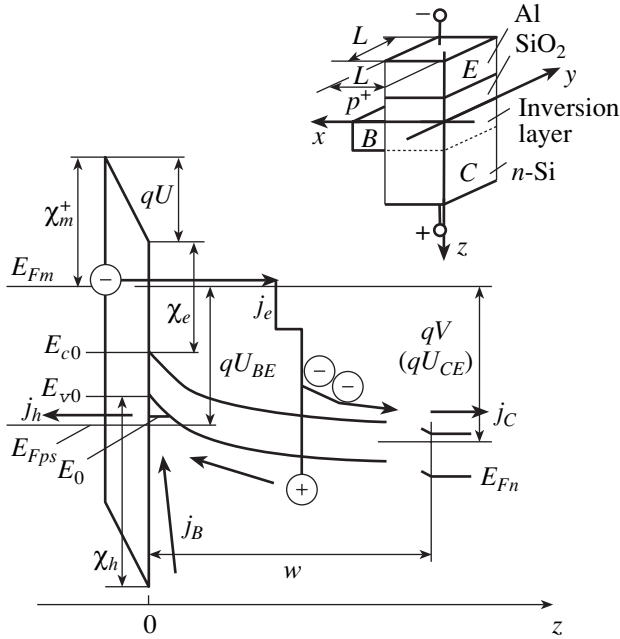
Fig. 1. The energy-band diagram of a transistor with a MOS emitter. The inset shows the structure of the transistor involving (*E*) the emitter, (*B*) base, and (*C*) collector.

applied to the Si wafer. As a result, an inversion *p*-type layer is induced near the Si/SiO$_2$ interface.

In studying the MOS structures, band bending in the metal is commonly disregarded, so that the motion of carriers in the metal, as well as the motion of electrons in the conduction band of Si, is assumed confined only in the *xy* plane; the motion in the direction of tunneling, *z*, is assumed to be infinite. At the same time, the motion of holes in the inversion layer is quantum-confined in all directions. As a result, we have a quantum dot, in which the states are described by the combinations of the following wave functions:

$$\psi = \psi_{FH}(z)\sin\left(\frac{\sqrt{2m_{hs}E_x}}{\hbar}x\right)\sin\left(\frac{\sqrt{2m_{hs}E_y}}{\hbar}y\right),$$

$$\psi_{FH} = \sqrt{\frac{b^3}{2}}z\exp\left(-\frac{bz}{2}\right). \tag{1}$$

We consider here only the ground state in *z* and describe it by the Fang–Howard function ψ_{FH} [9]. The other states can be disregarded at $L \gg z_{inv}$, where $z_{inv} \approx 2$ nm is the typical width of the inversion layer in the *z* direction. The energies of the levels in the inversion layer are as follows:

$$E_{hs} = E_0 + (E_x + E_y) = E_0 + E_\perp^{n_x, n_y}$$

$$= E_0 + \frac{\pi^2\hbar^2}{2m_{hs}L^2}(n_x^2 + n_y^2), \quad n_x, n_y = 1, 2, 3, \ldots, \tag{2}$$

where m_{hs} is the hole mass in Si assumed, for simplicity, to be isotropic, similarly to the electron mass m_{es} in Si. The concentration of holes per unit area in the *xy* plane is

$$N_s = \frac{2}{L^2}\sum_{n_x, n_y}\left(\exp\frac{E_0 + E_\perp^{n_x, n_y} - E_{Fps}}{kT} + 1\right)^{-1}, \tag{3}$$

where the energy E_0 and the energy of the quasi-Fermi level for holes E_{Fps} are counted downward from the top of the valence band E_{v0}, *T* is temperature, and *k* is the Boltzmann constant. The allowed energies of electrons in the metal are given by a similar formula

$$E_{em} = E_z + E_{\perp m}^{n_x, n_y} = E_z + \frac{\pi^2\hbar^2}{2m_m L^2}(n_x^2 + n_y^2), \tag{4}$$

where the component of the energy E_z is counted upward and m_m is the electron mass in the metal. It should be noted that, at $L \longrightarrow \infty$, the levels relevant to the transverse direction merge together. In this case, we are dealing with the well-known situation of a large-area structure.

We now present the basic results of the theory of large-area tunnel transistors [4–7]. These results are used in this study. The parameter *b* of the wave function ψ_{FH} is calculated as

$$b = \left[\frac{12q^2 m_{hs}}{\varepsilon_0\varepsilon_s\hbar^2}\left(\frac{11}{32}N_s + N_d w\right)\right]^{1/3}. \tag{5}$$

Here, *w* is the width of the depletion layer, ε_s is the permittivity of Si, ε_0 is the electrical constant (the permittivity of free space), and N_d is the concentration of donors in Si. The energy of the ground state E_0 is represented by the following formula:

$$E_0 = \left(\frac{3}{2}\right)^{5/3}\left[\frac{q^2\hbar}{\sqrt{m_{hs}}\varepsilon_0\varepsilon_s}\right]^{2/3}\frac{N_d w + (55/96)N_s}{[N_d w + (11/32)N_s]^{1/3}}. \tag{6}$$

Once the band diagram has been calculated for a given collector voltage (U_{CE}) and a given base voltage (U_{BE}) [7], the tunneling currents of electrons (j_e) and holes (j_h) can be determined. Below, this problem is discussed separately. With j_e and j_h, it is possible to determine the currents that flow, under these conditions, through the device terminals (emitter, collector, and base):

$$j_E = j_e + j_h, \tag{7}$$

$$j_C = j_e M - j_{diff}, \tag{8}$$

$$j_B = j_h + j_{diff} - j_e(M - 1). \tag{9}$$

Here, M is the collector multiplication factor that accounts for both Auger ionization in Si by initially hot electrons, $P(E_e)$, and impact ionization:

$$M = [1 + P(E_e)][1 + \gamma]$$
$$= \left[1 + P\left(qU + \frac{q^2 N_s}{3\varepsilon_0\varepsilon_s b}\right)\right][1 + \gamma]. \tag{10}$$

The dependence of the quantum yield of Auger ionization, $P(E_e)$, is taken from [10] (the energy E_e is the energy of an electron injected from the Fermi level of the metal, E_{Fm}, after this electron has traversed the inversion layer). The quantum efficiency of impact ionization, γ, is determined for a given field profile [11]. The parameter U is the bias applied to the oxide layer.

The diffusion current of holes, j_{diff}, is calculated as the current of an abrupt, one-sided p–n junction by the following formula:

$$j_{\text{diff}} = \frac{\sqrt{q\mu_p kT}}{\sqrt{\tau_p}}\frac{n_i^2}{N_d^+}\left(\exp\frac{U_{BE} - U_{CE}}{kT} - 1\right). \tag{11}$$

Here, n_i is the intrinsic carrier concentration in Si at a given temperature, N_d^+ is the concentration of ionized donors in the Si bulk, μ_p is the hole mobility (assumed to be a constant equal to 480 cm^2/(V s)), and τ_p is the hole lifetime in the n-type material (taken to be 8 μs). It is clear that, in actual practice, the lifetime τ_p can change in a wide range; for the subject of this study, however, the choice of the exact value of τ_p is of no importance, since this parameter does not affect the values of the tunneling currents and is important only if $U_{BE} > U_{CE}$.

3. TUNNELING CURRENTS IN TRANSVERSE-SIZE-CONFINED MOS STRUCTURES

We assume that the total energy of a particle, E, can be divided into two components: the energy of motion in the direction of tunneling, E_z, and the energy of motion in the transverse xy plane, $E_\perp$. We adopt a simple but extensively used model of tunneling transport. In this model, the probability of tunneling Θ depends only on E_z (see, e.g., [4, 12]), and the quantity being conserved is the energy $E_\perp$, along with the total energy E. For calculating Θ, the Wentzel–Kramers–Brillouin (WKB) method is used [13]. If we imposed the more logical condition of conservation of the transverse wave vector $\mathbf{k}_\perp$ [14], instead of $E_\perp$, more cumbersome calculations would be required, and at the same time, the results would be in many respects less valuable because the SiO$_2$ band structure is inadequately understood.

The current of electrons from the metal to the conduction band of Si at $V \gg kT$ can be written as

$$j_e = \frac{q}{2\pi\hbar}\int\limits_0^{+\infty}\Theta(E_z, \chi_e + qU, d, m_e^i)dE_z$$
$$\times \int\limits_0^{+\infty}\rho_{\perp,m}\frac{dE_\perp}{\exp[(E_z + E_\perp - E_{Fm})/kT] + 1}, \tag{12}$$

where $\rho_{\perp,m}$ is the density of states in the xy plane on the side of the barrier structure from which the particle tunnels, i.e., in the metal. The energies E_z and E_{Fm} are counted upward from the bottom of the conduction band, E_{c0}.

The current of holes from the inversion layer is written as

$$j_h = \frac{q}{\tau(E_0)}\Theta(E_0, \chi_h, d, m_h^i)$$
$$\times \int\limits_0^{+\infty}\rho_{\perp,hs}\frac{dE_\perp}{\exp[(E_0 + E_\perp - E_{Fps})/kT] + 1}. \tag{13}$$

The energies E_0, E_{Fps}, and E_{Fm} to be substituted in formula (13) are counted downward from E_{v0}; $\tau(E_0)$ is the time interval between the collisions of a hole with the tunneling-barrier wall.

Depending on whether or not the transverse quantum-confinement effect is disregarded, the density of states $\rho_\perp$ (expressed in J^{-1} m^{-2}) in formulas (12) and (13) is written in one of the following manners:

$$\rho_{\perp,m} = \frac{m_{es}}{\pi\hbar^2}, \quad \rho_{\perp,hs} = \frac{m_{hs}}{\pi\hbar^2}; \tag{14}$$

$$\rho_{\perp,m} = \sum_{n_x, n_y}\frac{2}{L^2}\delta(E_\perp - E_{\perp,m}^{n_x, n_y})\frac{m_{es}}{m_m}\nu_s,$$

$$\rho_{\perp,hs} = \sum_{n_x, n_y}\frac{2}{L^2}\delta(E_\perp - E_\perp^{n_x, n_y})\nu_m. \tag{15}$$

The factor ν_s (ν_m) describes the difference between the levels $E_\perp$ in the semiconductor and metal and, thus, effectively accounts for the reduction in the current because of the finite density of states on the side of the barrier structure to which the particle tunnels. This factor can be estimated on the assumption that each level (n_x, n_y) is broadened in energy $E_\perp$ according to the density

$$g(E_\perp) = \frac{1}{2kT}\exp\left(-\frac{|E_\perp - E_\perp^{n_x, n_y}|}{kT}\right). \tag{16}$$

If δ_E is the difference in energy between the level $E_\perp^{n_x, n_y}$ (from which the particle tunnels) and a level on the opposite side with respect to the barrier, then the prob-
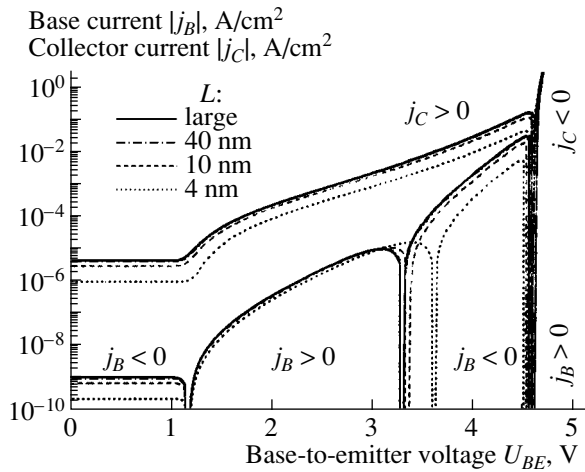
Base current $|j_B|$, A/cm^2
Collector current $|j_C|$, A/cm^2

Fig. 2. The behavior of the currents through the base and collector at different transverse dimensions of the emitter L. $N_d = 10^{16}$ cm^{-3} and $d = 2.5$ nm.
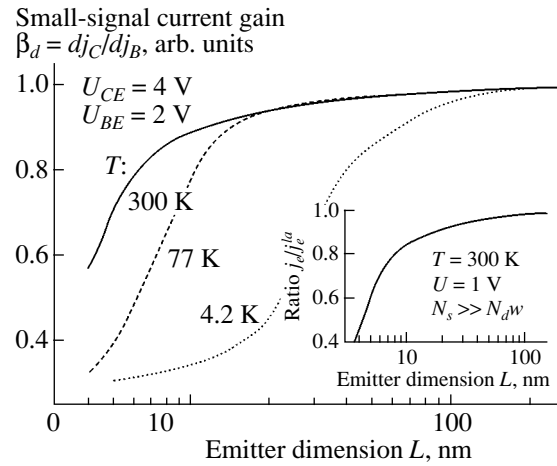
Small-signal current gain
$\beta_d = dj_C/dj_B$, arb. units

Fig. 3. Dependences of the small-signal gain on the emitter size L at different temperatures. $N_d = 10^{16}$ cm^{-3} and $d = 2.5$ nm. The inset shows the dependence of the electron tunneling current on the emitter size.

ability that tunneling is impossible because of this difference is $1 - \exp(-\delta_E/2kT)$. We now assume that, on the other side with respect to the barrier, the levels are separated from each other by the energy

$$E^* = s(mL^2/\pi\hbar^2)^{-1}. \tag{17}$$

Let Δ be the difference in energy between $E_\perp^{n_x, n_y}$ and the adjacent level on the other side ($s \approx 3$ is the degree of degeneracy). Then, the probability of "overlapping" that affects the tunneling is expressed as

$$P_{\text{overl}} = 1 - \prod_{i = -\infty}^{+\infty} \left[1 - \exp\left(-\frac{|\Delta + iE^*|}{2kT} \right) \right]. \tag{18}$$

The quantity Δ is uniformly distributed in the range from zero to $E^*/2$. Therefore, the factor that describes the difference between the transverse levels $E_\perp$ is defined as

$$\nu = \frac{2}{E^*} \int_0^{E^*/2} P_{\text{overl}}(\Delta) d\Delta. \tag{19}$$

When treating the tunneling of electrons into Si, we replace the effective mass m in formula (17) by m_{es} and now denote ν by ν_s; when treating the transport of holes from Si, we take the mass m_m and introduce $\nu = \nu_m$. For all temperatures and sizes other than $T \longrightarrow 0$ and $L \longrightarrow 0$, the factor ν is close to unity: $\nu \sim 1$ (for example, at $T = 77$ K and $L = 10$ nm, we have $\nu_m \approx 0.99$).

In the calculation, we took the following values of the effective masses and barrier heights: $m_e^i = 0.42m_0$ [15], $m_h^i = 0.37m_0$ [16], $m_m = m_0$, $m_{hs} = 0.5m_0$, $m_{es} = 0.4m_0$, $\chi_m^+ = \chi_e = 3.16$ eV, and $\chi_h = 4.63$ eV.
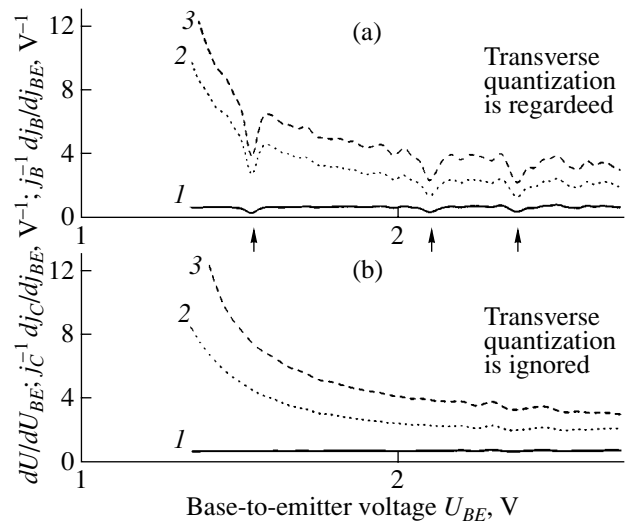

Fig. 4. Derivative of the parameters (*1*) dU/dU_{BE}, (*2*) $j_C^{-1} dj_C/dU_{BE}$, and (*3*) $j_B^{-1} dj_B/dU_{BE}$ calculated (a) taking into account and (b) disregarding transverse quantum confinement. $d = 2.5$ nm; $L = 10$ nm; and $T = 4.2$ K. (a) Arrows indicate the quantum features of the dependences. Small irregularities in the curves appear due to the limited accuracy of the calculations.

4. RESULTS AND DISCUSSION

Figure 2 shows the dependences of the base current (j_B) and the collector current (j_C) on the base–emitter voltage (U_{BE}) for several values of the transverse dimension L. The collector voltage is assumed to be fixed. The features in the dependence $j_B(U_{BE})$ and the change of the sign of j_B are due to the internal source of holes. Actually, at low U_{BE}, the holes are supplied by the diffusion current j_{diff} and, in part, by impact ioniza-
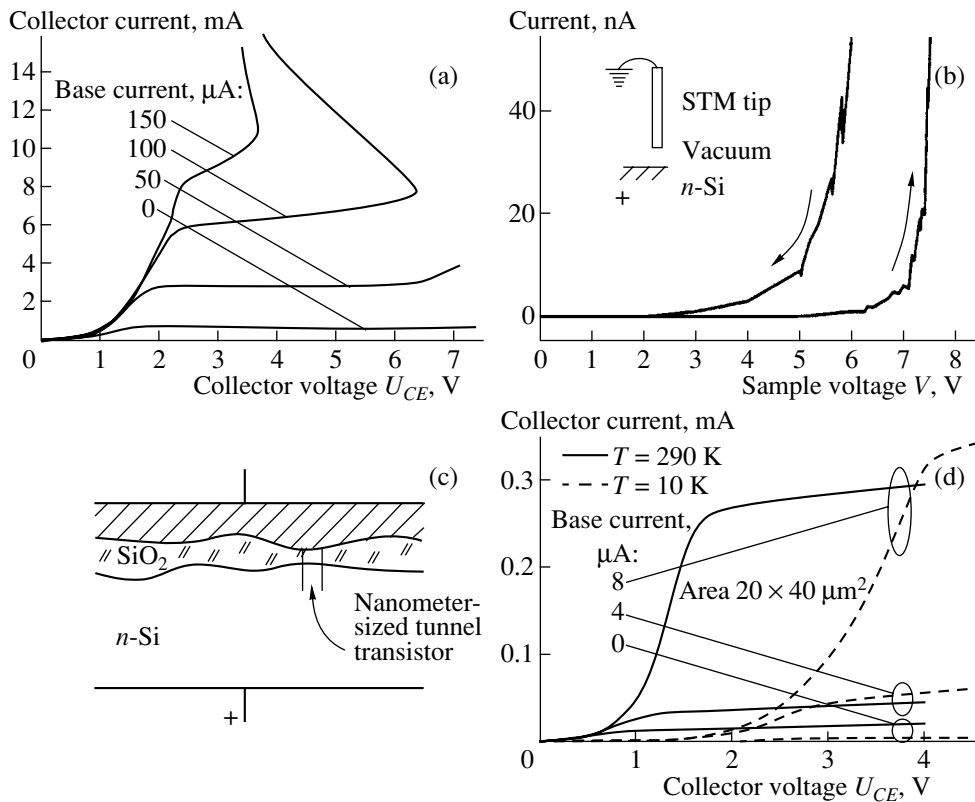
Fig. 5. Experimental data on the behavior of transistors that include the tunnel MOS emitters: (a) switching of a large-area transistor [16], (b) switching of the contact of a scanning tunnel microscope [18], (c) a MOS structure including an oxide layer nonuniform in thickness as an array of nanometer-sized tunnel transistors, and (d) confirmation of the ability of a bipolar tunnel transistor to operate at low temperatures [8].

tion (γ) and, at $U_{BE} > 3.5$ V, by Auger ionization (P) [17]. The sharp increase in j_B and the decrease in j_C (with the change of sign) at $U_{BE} > 4.5$ V are due to the component j_{diff}: in this case, the base–collector junction is found to be biased in the forward direction.

It can be seen that a decrease in the emitter size L is followed by a decrease in the currents j_B and j_C. This effect is most pronounced at $L < 10$ nm; it originates from the decrease in the effective two-dimensional density of states on both sides of the barrier as L decreases. In addition, with decreasing L, the voltage across the oxide layer, U, decreases at a given U_{BE} and produces a decrease in the tunneling current as well. For a smaller thickness of the oxide layer d and $N_d \sim 10^{14}$–10^{17} cm^{-3} (these values are typical of tunnel transistors), the dependences exhibit similar behavior.

In Fig. 3 (see the inset), the dependence of the tunneling current of electrons j_e on the dimension L at a fixed value of the voltage U is plotted. The current j_e is normalized to the corresponding current for a large-area emitter, j_e^{la}. The dependence shown in Fig. 3 illustrates the "net" effect of the decrease in size more clearly compared to that in Fig. 2. The condition $N_s \gg N_d w$, in which the voltage U is produced by the charge of the inversion layer only, is chosen for definiteness. In

this case, if the voltage U (rather than U_{BE}) is fixed, the dependence of j_h on L is controlled only by the factor ν_m and found to be weak at 300 K.

With decreasing L, the decrease in j_C is more pronounced than the change in j_B (at $U_{BE} \approx 2$–3 V). The cause of this effect is the fact that, for a fixed voltage U_{BE}, the decrease in U with decreasing L is not large. In this case, the two-dimensional concentration of holes involved in tunneling varies only slightly, in spite of the quantum-confinement effect (under the condition $N_s \gg N_d w$, this concentration varies similarly to U). In contrast, the current j_e decreases more substantially, since the number of tunneling electrons (with energies from E_{c0} to E_{Fm}) decreases due to the effect of transverse quantum confinement upon $E_\perp$. Together, these circumstances define a reduction in the gain of the transistor. It should also be noted that the factor ν_s for transport from the metal is smaller than ν_m ($m_m > m_{es}$). This circumstance produces an additional degradation of the gain at low T. The dependence of the low-signal gain $\beta_d = dj_C/dj_B$ on the dimension L is exemplified in Fig. 3 (to obtain the absolute values, β_d should be multiplied by ~370).

In addition to the above-discussed manifestations of the transverse quantum-confinement effect in the tun-

nel transistor, we note that, when analyzing the quantum effects on the properties of devices, researchers often intuitively expect some stepwise or peaklike features. By differentiating the curves (for $T = 4.2$ K), such kinds of features can be resolved in the case under study as well (Fig. 4). For example, the dependences $j_B^{-1} dj_B/dU_{BE}$ and $j_C^{-1} dj_C/dU_{BE}$ on U_{BE} exhibit downward directed peaks that appear because the dependence $U(U_{BE})$ is nonmonotonic due to successive pinning of the quasi-Fermi level E_{Fps} at the discrete levels in the quantum well.

At present, no detailed experimental data on the behavior of transistors with submicrometer-sized MOS emitters have been obtained. At the same time, there exist a number of facts that are pertinent to the subject under consideration here and, to some extent, support the conclusions of this study (Fig. 5).

The results obtained here correlate well with the available theoretical and experimental data for large-area transistors ([5, 6], etc.). Specifically, it follows from the curve $j_{BE}(U_{BE})$ (Fig. 2) that, for fixed j_B and U_{CE}, there exist three states of the transistor, and two of them are stable. The bistability of a tunnel MOS structure was observed previously in [6, 16] (Fig. 5a).

For extremely small L, there exists an experimental confirmation of the ability of a tunnel transistor to switch. In the corresponding experiment, the tip of a scanning tunnel microscope (STM) served as an emitter [18] (Fig. 5b).

A conventional "large-sized" MOS structure, in which the SiO_2 layer has a noticeable spread in thickness (Fig. 5c), as mentioned, for example, in [19], possibly represents a device that involves one or several nanometer-sized tunnel MOS transistors. With the Gaussian distribution of the SiO_2 thickness over the area, the total area of thin regions is small. However, these regions should make an essential contribution to the current through the structure [20]. According to the results of this study, the current through these regions and, hence, the total current through the device should be lower than that obtained in the model in which the effect of quantum confinement on the energy $E_\perp$ is disregarded.

The effects discussed above become more pronounced with decreasing T. Therefore, of great importance is the available confirmation of the ability of a tunnel transistor to operate at liquid-helium temperatures, although the characteristics of the transistor exhibit some modifications at such low temperatures [8] (Fig. 5d). For bipolar transistors, such an ability is rather nontrivial.

5. CONCLUSIONS

In this study, the behavior of a submicrometer-sized tunnel MOS structure is analyzed. The structure is considered as a bipolar transistor involving a tunnel MOS emitter. It is shown that noticeable changes toward a decrease in the current and small-signal gain appear approximately at $L = 10$–20 nm. This size is only four–

five times smaller than the size of the gate in commercial field-effect transistors. This means that the issue considered in this study is actually a topical problem. The effects revealed here result first of all from the reduction in the effective density of states due to quantum confinement of charge carrier motion in the plane orthogonal to the direction of tunneling. The experimental results thus far obtained in this field count in favor of the model adopted in the study.

REFERENCES

1. *SEMATECH. The International Technology Roadmap for Semiconductors*, http://public.itrs.net/home.htm (2001).
2. H. S. Momose, M. Ono, T. Yoshitomi, *et al.*, IEEE Trans. Electron Devices **43**, 1233 (1996).
3. J. P. Shiely, *Simulation of Tunneling in MOS Devices* (Duke Univ., NC USA, 1999), Chap. 5.5.
4. J. G. Simmons and G. W. Taylor, Solid-State Electron. **29**, 287 (1986).
5. E. Aderstedt, I. Medugorac, and P. Lundgren, Solid-State Electron. **46**, 497 (2002).
6. E. V. Ostroumova and A. A. Rogachev, Fiz. Tekh. Poluprovodn. (St. Petersburg) **33**, 1126 (1999) [Semiconductors **33**, 1027 (1999)].
7. A. F. Shulekin, M. I. Vexler, and H. Zimmermann, Semicond. Sci. Technol. **14**, 470 (1999).
8. I. V. Grekhov, K. Schmalz, A. F. Shulekin, *et al.*, Cryogenics **38**, 613 (1998).
9. T. Ando, A. B. Fowler, and F. Stern, *Electronic Properties of Two-Dimensional Systems* (Am. Phys. Soc., New York, 1982; Mir, Moscow, 1985), Chap. 3.
10. W. E. Drummond and J. L. Moll, J. Appl. Phys. **42**, 5556 (1971).
11. S. Sze, *Physics of Semiconductor Devices*, 2nd ed. (Wiley, New York, 1981; Mir, Moscow, 1984), Vol. 1, Chap. 1.
12. R. Tsu and L. Esaki, Appl. Phys. Lett. **22**, 562 (1973).
13. D. I. Blokhintsev, *Fundamentals of Quantum Mechanics*, 4th ed. (Vysshaya Shkola, Moscow, 1961; Reidel, Dordrecht, 1964), pp. 121, 329.
14. A. Ghetti, A. Hamad, P. J. Silverman, *et al.*, in *Proceedings of SISPAD* (Kyoto, 1999), p. 239.
15. A. Schenk and G. Heiser, J. Appl. Phys. **81**, 7900 (1997).
16. A. Haque and K. Alam, Appl. Phys. Lett. **81**, 667 (2002).
17. S. K. Lai, P. V. Dressendorfer, T. P. Ma, and R. C. Barker, Appl. Phys. Lett. **38**, 41 (1981).
18. L. N. Bolotov, I. V. Makarenko, A. F. Shulekin, and A. N. Titkov, Surf. Sci. **331–333**, 468 (1995).
19. I. V. Grekhov, E. V. Ostroumova, A. A. Rogachev, and A. F. Shulekin, Pis'ma Zh. Tekh. Fiz. **17** (13), 44 (1991) [Sov. Tech. Phys. Lett. **17**, 476 (1991)].
20. R. Khlil, A. El Hdiy, A. F. Shulekin, *et al.*, Microelectron. Reliab. **44**, 543 (2004).

Translated by É. Smorgonskaya

SEMICONDUCTOR STRUCTURES, INTERFACES, AND SURFACES

Simulation of the Capacitance–Voltage Characteristics of a Ferroelectric Material

L. S. Berman

Ioffe Physicotechnical Institute, Russian Academy of Sciences, St. Petersburg, 194021 Russia
Submitted March 15, 2005; accepted for publication March 30, 2005

Abstract—The parameters of a ferroelectric material without initial polarization are simulated. The ferroelectric material is doped with a shallow-level impurity. One of the contacts is represented by the Schottky barrier, and the other contact is ohmic. The variations in the electric field, potential, polarization, and permittivity through the depth of the space charge layer are calculated. It is shown that the value of the permittivity in low fields, $\varepsilon_{\mathrm{eff0}}$, can be determined from the parameters of the experimental hysteresis loop. In low fields ($E < 10^5$ V/cm), the permittivity depends on the field only slightly. Therefore, for ($E < 10^5$ V/cm), the value of $\varepsilon_{\mathrm{eff0}}$ can be used as the average value of $\varepsilon_{\mathrm{eff}}$ in processing the experimental data. The calculation of the dependence of the reverse capacity squared on the potential-barrier height shows that, at low voltages, this dependence is nearly linear. This allows the concentration of shallow dopants to be determined from the dependence. The thickness of the space charge layer and the polarization near the contact are calculated as functions of the potential-barrier height. The results of the simulation can be used in processing the experimental data.
© 2005 Pleiades Publishing, Inc.

1. INTRODUCTION

At present, thin ferroelectric (FE) films are extensively used in electronics in a number of circuits (see, e.g., [1–5]). In this context, simulation of the characteristics of FE materials is a topical problem as its solution allows one to predict the FE parameters and thus avoid rather complicated expensive experiments. In earlier studies [6–9], the behavior of nonideal FEs in various electronic circuits was simulated. The effect of the blocking layer on the FE parameters was simulated in [9–12].

In this study, the parameters of a FE material doped with shallow-level impurities are simulated in detail in the case of the absence of initial polarization. The simulation provides additional data on the FE parameters.

2. FORMULATION OF THE PROBLEM AND CALCULATIONS

We assume that a FE material is doped with shallow donors with the concentration N_d. The polycrystalline structure of the FE material, its inhomogeneity, and structural defects are taken into account using the averaged values of the parameters (e.g., mobility). Let the metal forming the Schottky barrier be deposited on one side of the FE material, and an ohmic contact be formed on the other side. Then, for describing the FE, we can use the well-known relationships of electrostatics

$$D = \varepsilon_0 E + P, \qquad (1)$$

$$\frac{d}{dx}D = \rho = qN_d, \qquad (2)$$

where D is the induction, ε_0 is the permittivity of free space, E is the electric field, P is the polarization, x is the coordinate measured from the interface between the electroneutrality region (ENR) and the space-charge region (SCR), ρ is the space-charge density, and q is the elementary charge.

Differentiating Eq. (1) with respect to x, we obtain, after rearrangements, the following equation:

$$\frac{d}{dx}E = \frac{\rho}{\varepsilon_{\mathrm{eff}}}, \qquad (3)$$

where the effective permittivity of the FE material is

$$\varepsilon_{\mathrm{eff}} = \varepsilon_0 + \frac{d}{dE}P. \qquad (4)$$

We approximate the dependence $P(E)$ by a hyperbolic-tangent function [6]. We assume that the FE material was initially depolarized ($P = 0$) by a certain means, e.g., by decreasing the amplitude of an alternative voltage. Then we have

$$P = P_s \tanh\!\left(\frac{E}{2d}\right). \qquad (5)$$

Here, P_s is the saturation polarization and the parameter d is defined by the expression

$$d = E_c\left[\ln\!\left(\frac{1 + P_r/P_s}{1 - P_r/P_s}\right)\right]^{-1}, \qquad (6)$$
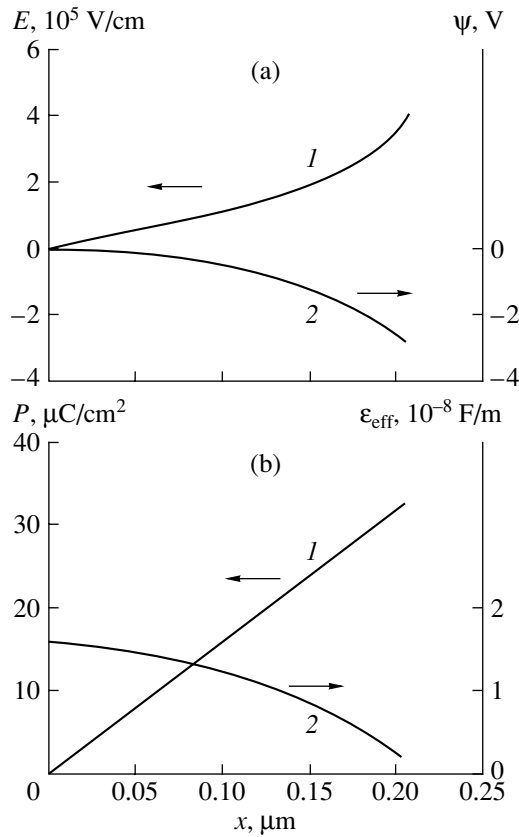
Fig. 1. Variations in the parameters of a ferroelectric material through the depth of the space-charge region for $V + V_{bi} = 2.8$ V. Variations in (a, curve 1) the electric field E (a, curve 2) the potential ψ, (b, curve 1) the polarization P, and (b, curve 2) the effective permittivity ε_{eff} are shown.

where E_c is the coercive field and P_r is the remanent polarization. Differentiating (5) with respect to E, we obtain the following equation:

$$\frac{d}{dE}P = \frac{P_s}{2d[\cosh(E/2d)]^2}. \qquad (7)$$

At the ENR–SCR interface, the electric field, potential, and polarization satisfy the following conditions:

$$E = 0, \quad \psi = 0, \quad \text{and} \quad P = 0. \qquad (8)$$

We now integrate the Poisson equation numerically in the range from the ENR–SCR interface to the metal (Schottky barrier), with the step $\Delta x = w/n$, where w is the SCR width and $n \gg 1$ is an integer. For the first step, we have

$$E_1 = dE_1 = \frac{qN_d w}{\varepsilon_{eff0} n},$$

where $\varepsilon_{eff0} = \varepsilon_0 + P_s/2d$ is the low-field value of ε_{eff} (cf. ε_{eff0} with (4) and (7)). The value of ε_{eff0} can be calculated using the experimental values of P_s and d. The

potential, polarization, and permittivity corresponding to E_1 are as follows:

$$\psi_1 = -E_1 \Delta x, \quad P_1 = P_s \tanh\left(\frac{E_1}{2d}\right),$$

$$\varepsilon_{eff1} = \varepsilon_0 + \frac{P_s}{2d[\cosh(E_1/2d)]^2}.$$

We use the recurrent method: the succeeding values of the parameters are calculated from their preceding values. We calculate the values of E_n, ψ_n, P_n, D_n, and ε_{effn}, where the subscript n refers to the values of the parameters at the interface between the FE material and the metal. Then we determine the voltage across the Schottky diode, V; the charge at the metal contact, Q_m; and the capacitance of the Schottky diode, C, from the following relations:

$$V + V_{bi} = \psi_n, \quad Q_m = -D_n, \quad \text{and} \quad C = \left|\frac{d}{dV}Q_m\right|, \qquad (9)$$

where V_{bi} is the contact potential difference between the metal and the FE material ($V + V_{bi} < 0$).

The result of integration of the Poisson equation can also be represented as follows [13]:

$$V + V_{bi} = -qN_d\int_0^w [\varepsilon_{eff}(x)]^{-1}xdx. \qquad (10)$$

In expression (10), x is counted from the Schottky barrier (rather than from the ENR–SCR interface). Differentiating (10) with respect to w, we obtain

$$\frac{d|V|}{dw} = qN_d\int_0^w \frac{d}{dw}[(\varepsilon_{eff})^{-1}]xdx + qN_dw[\varepsilon_{eff}(w)]^{-1}, (11)$$

where $\varepsilon_{eff}(w)$ is the value of ε_{eff} at the ENR–SCR interface, i.e., in a low field: $\varepsilon_{eff}(w) = \varepsilon_{eff0}$.

At the same time, the following relation is also valid:

$$dD_n = -dQ_m = qN_dAdw, \qquad (12)$$

where A is the area of the FE material.

Hence, we have

$$\frac{1}{C} = \left|\frac{dV}{dQ_m}\right| = \frac{|dV|}{dw}\left|\frac{dw}{dQ_m}\right|.$$

After rearranging, we obtain

$$\frac{A}{C} = \frac{w}{\varepsilon_{eff0}} + \int_0^w \frac{d}{dw}[(\varepsilon_{eff})^{-1}]xdx. \qquad (13)$$

The integral in expression (13) is calculated numerically, with the dependence $\varepsilon_{eff}(x)$ obtained previously (see above and Fig. 1).
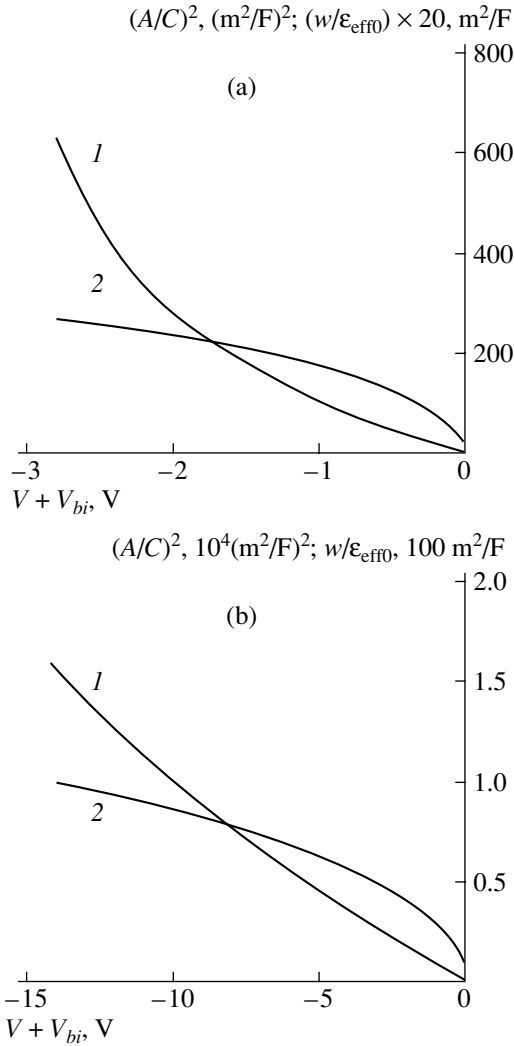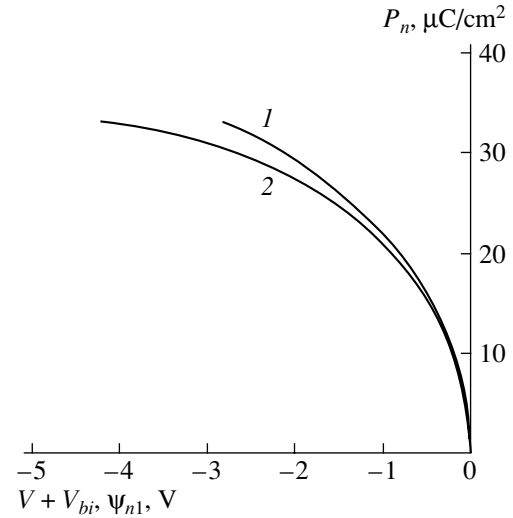
Fig. 3. The dependences of the polarization near the contact P_n on (1) the barrier height $V + V_{bi}$ and (2) the potential ψ_{n1}.

Fig. 2. The dependences of the quantities (1) $(A/C)^2$ and (2) w/ε_{eff0} on the barrier height $V + V_{bi}$. The concentration of shallow dopants N_d is (a) 10^{19} and (b) 10^{18} cm^{-3}.

3. RESULTS AND ANALYSIS

In the calculations, we used the following values of the parameters: $P_s = 35$ μC/cm^2, $P_r = 25$ μC/cm^2, $E_c = 2 \times 10^5$ V/cm, $N_d = 10^{18}$ and 10^{19} cm^{-3}, and $A = 1$ mm^2.

Figure 1 shows the variations in the electric field, potential, polarization, and permittivity through the depth of the SCR at $V + V_{bi} = -2.8$ V. The field increases with the depth in the SCR, ranging up to the value 4×10^5 V/cm at the contact; this value is close to the breakdown field [1].

The polarization P increases from zero to 33 μC/cm^2 close to the saturation value. As the field increases from zero to 4×10^5 V/cm, the parameter ε_{eff} decreases almost by a factor of 10; the sharp decrease in ε_{eff} near the contact correlates with a sharp increase in the field. In low fields, however, the permittivity ε_{eff} varies only slightly. For example, at $E = 8 \times 10^4$ V/cm, the decrease

in ε_{eff} is only 15%. Therefore, the value of ε_{eff0} can be used in the processing of the low-field data.

Figure 2 shows the dependences of $(A/C)^2$ on $V + V_{bi}$ for $N_d = 10^{19}$ and 10^{18} cm^{-3} (the other parameters are the same as before). We set the minimum value of $|V + V_{bi}|$ as 0.5 V. The dependences of $(A/C)^2$ on $V + V_{bi}$ are almost linear in the range $-1.0 \leq (V + V_{bi}) \leq -0.5$ V for $N_d = 10^{19}$ cm^{-3} and in the range $-5 \leq (V + V_{bi}) \leq -0.5$ V for $N_d = 10^{18}$ cm^{-3}. Based on this result, we use, for the above-indicated ranges, the following well-known relation for the Schottky diode involving a linear insulator [14]:

$$N = \left[\frac{(A/C_1)^2 - (A/C_2)^2}{|V_2 - V_1|} 0.5 q \varepsilon_{eff0} \right]^{-1}, \qquad (14)$$

where N is the concentration of shallow dopants and V_1, V_2, C_1, and C_2 are, respectively, the voltages and capacitances at the boundaries of the ranges. We compare the value of N obtained from expression (14) with the initial value N_d. For example, for $N_d = 10^{19}$ cm^{-3}, we have the following calculated values: $V_1 + V_{bi} = -0.51$ V, $V_2 + V_{bi} = -1.0$ V, $C_1 = 0.15$ F/m^2, and $C_2 = 0.10$ F/m^2. From expression (14), we obtain $N = 7.1 \times 10^{18}$ cm^{-3}.

Similarly, for $N_d = 10^{18}$ cm^{-3}, we have the following calculated values: $V_1 + V_{bi} = -0.52$ V, $V_2 + V_{bi} = -1.05$ V, $C_1 = 0.05$ F/m^2, and $C_2 = 0.035$ F/m^2. From (14), we obtain $N = 9.8 \times 10^{17}$ cm^{-3}.

Thus, expression (14) can be used in data processing for determining the concentration of shallow donor dopants.

Figure 2 also shows the dependence of w/ε_{eff0} (the first term in expression (13)) on $V + V_{bi}$. With the known value of ε_{eff0}, we can determine the dependence of the SCR width on the potential-barrier height.

Figure 3 shows the calculated dependence of P_n at the interface between the FE material and the metal on $V + V_{bi}$ for $N_d = 10^{19}$ cm^{-3}. The dependence of P_n on ψ_{n1}, where $\psi_{n1} = 0.5 E_n w$ is the average potential in the SCR of the FE material, is also shown.

4. CONCLUSIONS

The parameters of a ferroelectric material without initial polarization are simulated. The ferroelectric material is doped with shallow-level impurities. The variations in the electric field, potential, polarization, and permittivity through the depth of the space-charge region are calculated. It is shown that the low-field permittivity ε_{eff0} can be determined from the parameters of the experimental hysteresis loop. In low fields, the permittivity depends on the field only slightly. Therefore, at $E < 10^5$ V/cm, the value of ε_{eff0} can be used in data processing as the average value of the permittivity ε_{eff}. The dependence of C^{-2} on the potential-barrier height $V + V_{bi}$ is calculated; at low voltages, this dependence is nearly linear. This makes it possible to determine approximately the concentration of shallow dopants in the space-charge region.

The dependences of the space charge region width and of the polarization near the contact on the barrier height are calculated.

The results of the simulation can be used in processing the experimental data.

ACKNOWLEDGMENTS

REFERENCES

1. J. F. Scott, Ferroelectr. Rev. **1**, 2 (1998).

2. I. Grekhov, L. Delimova, I. Liniichuk, *et al.*, Integr. Ferroelectr. **43**, 175 (2002).

3. H. Ishiwara, J. Semicond. Technol. Sci. **1**, 1 (2001).

4. J. F. Scott, Jpn. J. Appl. Phys. **38**, 2272 (1999).

5. P. W. Bloom, R. M. Wolf, J. F. M. Cillessen, and M. P. K. M. Krijn, Phys. Rev. Lett. **38**, 2107 (1994).

6. S. L. Miller, R. D. Nasby, J. R. Schwank, *et al.*, J. Appl. Phys. **68**, 6463 (1990).

7. S. L. Miller, J. R. Schwank, R. D. Nasby, and M. S. Rodgers, J. Appl. Phys. **70**, 2849 (1991).

8. S. L. Miller and P. J. McWhorter, J. Appl. Phys. **72**, 5999 (1992).

9. L. S. Berman, Fiz. Tekh. Poluprovodn. (St. Petersburg) **35**, 200 (2001) [Semiconductors **35**, 193 (2001)].

10. A. K. Tagantsev, M. Landivar, E. Colla, and N. Setter, J. Appl. Phys. **78**, 2623 (1995).

11. P. K. Larsen, G. T. M. Dormans, D. J. Taylor, and P. T. van Veldhoven, J. Appl. Phys. **76**, 2405 (1994).

12. L. S. Berman, Fiz. Tekh. Poluprovodn. (St. Petersburg) **39**, 332 (2005) [Semiconductors **39**, 313 (2005)].

13. L. S. Berman, *Introduction to the Physics of Varactors* (Nauka, Moscow, 1968; Israel Program for Scientific Translations, Jerusalem, 1970).

14. S. M. Sze, *Physics of Semiconductor Devices*, 2nd ed. (Wiley, New York, 1981; Mir, Moscow, 1984), Vol. 1.

Translated by É. Smorgonskaya

Estimation of the Energy Characteristics of the 3*C*-SiC/2*H*-, 4*H*-, 6*H*-, and 8*H*-SiC Heterojunctions

S. Yu. Davydov^, A. A. Lebedev, and O. V. Posrednik

Ioffe Physicotechnical Institute, Russian Academy of Sciences, St. Petersburg, 194021 Russia
^e-mail: Sergei.Davydov@mail.ioffe.ru
Submitted February 7, 2005; accepted for publication March 31, 2005

Abstract—Based on the assumption that the electron affinity of the SiC polytypes is linearly dependent on the degree of hexagonality, the offsets of the conduction band and valence band at the point of contact between the cubic 3*C*-SiC polytype and the hexagonal *NH*-SiC ($N = 2, 4, 6$, and 8) polytypes are determined. In the model of a triangular quantum well, the energy of the ground state, ε_0, is estimated. It is shown that the position of the energy level ε_0 can be adequately controlled only by doping the wide-gap *n-NH*-SiC polytype with shallow donors. © 2005 Pleiades Publishing, Inc.

1. In the last few years, interest in the heterostructures and superlattices fabricated on the basis of different silicon carbide polytypes has grown [1]. Most of the attention has been concentrated on the 3*C*/6*H* [2, 3] and 3*C*/4*H* SiC-based heterojunctions [4]. In such structures, a two-dimensional electronic quantum well (QW) containing at least one localized state is formed at the contact in the region of the narrow-gap component (3*C*-SiC) of the system. The basic energy characteristics of a heterojunction are the offsets of the conduction band, ΔE_C, and of the valence band, ΔE_V [5]. A two-dimensional (2D) QW is characterized by the position of the local levels ε_0, ε_1, etc., measured from the bottom of the well (actually, the energies ε_0, ε_1, etc., are the edges of the corresponding 2D subbands; however, the term "level" will be used below for simplicity). The system as a whole is characterized by the Fermi level E_F or, more precisely, by the chemical potential. As a rule, the level ε_0 is below the Fermi level, while the level ε_1 is above the Fermi level. In this paper, we report the estimates of the quantities ΔE_C, ΔE_V, and ε_0 for heterojunctions formed by the 3*C*-SiC and 2*H*-, 4*H*-, 6*H*-, and 8*H*-SiC polytypes.

In the context of the Shockley–Anderson model [5], the quantity ΔE_C is defined by the difference between the electron affinities of the cubic polytype, $\chi(3C)$, and of the corresponding hexagonal polytype, $\chi(NH)$, where $N = 2, 4, 6$, and 8. However, the problem is that the values of the electron affinities are determined with inadequate accuracy. For example, Andreev *et al.* [6] used the value $\chi(6H) = 4.4$ eV [6], while Bazack [7] reported $\chi(6H) = 3.3$–3.7 eV and $\chi(3C) = 4.0$ eV. At the same time, the values $\chi(3C) = 4.8$ eV and $\chi(2H) = 4.1$ eV are given in the handbook [8]. Here, we proceed in the following manner: we assume that

$$\chi(NH) = \chi(3C) - aD, \qquad (1)$$

where $D = n_k/(n_k + n_h)$ is the degree of hexagonality [9, 10] (n_k and n_h are the numbers of occupied cubic and hexagonal sites in the lattice) and a is a coefficient. For 3*C*-SiC, $D = 0$; for 2*H*-SiC, $D = 1$. It is worth noting that scaling of the characteristics of the polytypes in the parameter D is not a new approach (see, e.g., [9–11]). Figure 1 (curve *1*) shows the band gap E_g versus D for different polytypes. The values of D were taken from [10]. The values of E_g for the 3*C* (2.40 eV) and 2*H* (3.33 eV) polytypes were taken from [12]; for the 4*H* (3.23 eV) and 6*H* (3.0 eV) polytypes, from [13]; and for the 8*H* (2.86 eV) polytype, from [14]. It can be seen
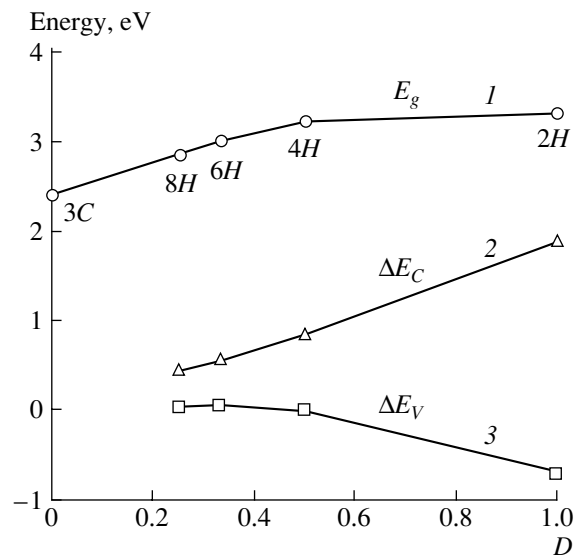

Fig. 1. (*1*) The band gap E_g of the SiC polytypes and (*2, 3*) the offsets of (*2*) the conduction bands, ΔE_C, and (*3*) valence bands, ΔE_V, for heterojunctions formed by different hexagonal SiC polytypes in contact with the cubic 3*C*-SiC polytype versus the degree of hexagonality D.
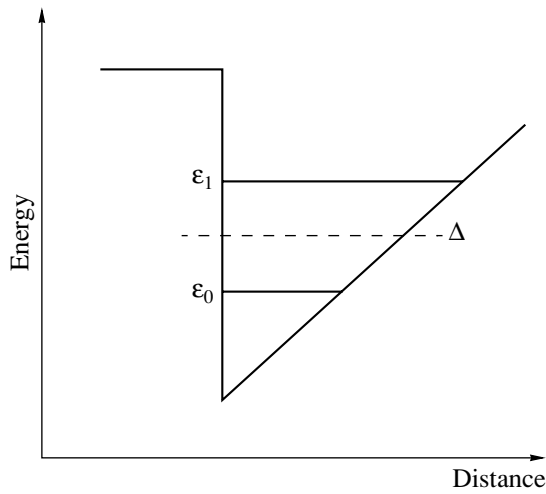
Fig. 2. A two-dimensional quantum well. The energy levels ε_0, ε_1, and Δ correspond to the edges of the ground subband and the first subband and to the Fermi level with respect to the bottom of the well.

from Fig. 1 that, in the range from $D = 0$ (3*C*) to $D = 0.5$ (4*H*), the band gap E_g is a linear function of the degree of hexagonality D. The exciton band gap exhibits a similar behavior [1].

According to the Shockley–Anderson model [5] and Eq. (1), we obtain

$$\Delta E_C = aD. \qquad (2)$$

With $\Delta E_C = 0.55$ eV determined for the 3*C*/6*H* junction in [3] ($D(6H) = 0.33$ [10]), we have $a \approx 1.67$ eV. The results of the calculation by formula (2) are shown in Fig. 1 (curve *2*). Curve *3* in Fig. 1 represents the values of ΔE_V calculated by the formula

$$\Delta E_V = \Delta E_g - \Delta E_C, \qquad (3)$$

where $\Delta E_g = E_g(NH) - E_g(3C)$.

From Fig. 1 (curve *3*) it follows that, for all polytypes with the exception for 2*H*, the value of ΔE_V is not larger than 0.05 eV. For 2*H*-SiC, the offset of the valence bands is $\Delta E_V = -0.70$ eV. It is worth noting that, for the 3*C*-SiC/6*H*-SiC heterojunction, the estimates $\Delta E_C = 0.55$ eV and $\Delta E_V \le 0.5$ eV in [2, 3] are in rather good agreement with $\Delta E_C = 0.70$ eV and $\Delta E_V = 0.10$ eV [1, 4]. For the 3*C*-SiC/4*H*-SiC heterojunction, the estimations yield $\Delta E_C = 0.83$ eV and $\Delta E_V = 0$ eV, whereas Fissel [1] reports the values 0.99 and 0.05 eV for ΔE_C and ΔE_V, respectively. If we substitute the value $\Delta E_C = 0.70$ eV for 3*C*-SiC/6*H*-SiC [1, 4] into expression (2), we obtain $a = 2.12$, which yields $\Delta E_C = 1.06$ eV for the 3*C*-SiC/4*H*-SiC in excellent agreement with $\Delta E_C = 0.99$ eV reported in [1]. Consequently, the representation of the electron affinity in the form of expression (1) is quite reasonable.

Thus, in the 3*C*-SiC/4*H*-, 6*H*-, and 8*H*-SiC heterojunctions, a quantum well in the conduction band is

formed on the narrow-gap 3*C* polytype side of the interface. At the same time, the offset of the valence bands in these polytypes is extremely small or, in the case of the 3*C*/4*H* interface, is nonexistent. At the 3*C*/2*H* interface, wells are formed in both the 3*C*-SiC conduction band and the 2*H*-SiC valence band. The electrons are localized in the interfacial layer of 3*C*-SiC, and the holes are localized in the layer of 2*H*-SiC.

2. We now estimate the energy of the local level, ε_0. In this case, the model of a triangular well [15, 16] with an infinitely high wall is commonly considered (Fig. 2). The condition for the infinitely high wall can be assumed to be satisfied, if $\Delta E_C \gg \varepsilon_0$, which is commonly the case. For the ground state ε_0, we have [16, 17]

$$\varepsilon_0 \approx 1.856\left(\frac{e^2 F^2 \hbar^2}{m^*}\right)^{1/3}, \qquad (4)$$

where F is the electric-field strength on the 3*C*-SiC side of the *NH*/3*C* interface (we consider the well in the conduction band), m^* is the electron effective mass in the 3*C*-SiC polytype, e is the elementary charge, and $\hbar$ is Dirac's constant.[1] Thus, the problem is reduced to the determination of the field F.

The value of F can be estimated roughly by the formula [3, 4] as

$$F = U/d, \qquad (5)$$

where U is the contact-potential difference and d is the width of the space charge region in 3*C*-SiC. We now follow [2, 3], in which the contact of *n*-6*H*-SiC with *p*-3*C*-SiC was considered. According to [2, 3], the maximum contact potential difference is

$$U_{max} = \chi(3C) + E_g(3C) - \chi(NH)$$
$$= \Delta E_C + E_g(3C). \qquad (6)$$

Formula (6) yields $U_{max} = 2.78, 2.90, 3.16$, and 3.92 eV for the 8*H*, 6*H*, 4*H*, and 2*H* polytypes, respectively. It is worth noting that the contact-potential differences determined in [2, 3] are 2.65 eV [2] and 2.43 eV [3], respectively.

Furthermore, it can be shown [18] that, in the case of completely ionized shallow donors and acceptors, the electric field is

$$F = \sqrt{\frac{2\pi e p_0 U [p_0 \varepsilon_{st}(3C) + n_0 \varepsilon_{st}(NH)]}{\varepsilon_{st}(3C)\varepsilon_{st}(NH)n_0}}, \qquad (7)$$

where ε_{st} is the static permittivity of the corresponding polytype, n_0 is the concentration of electrons in the bulk of 6*H*-SiC, and p_0 is the concentration of holes in the

---

[1] Every so often, the approximate quasi-classical expression (see, e.g., [15]), which holds well for the excited states ε_1, ε_2, etc., is used instead of formula (4). This may lead to some misunderstanding. For example, using the quasi-classical formula in [3], we obtained $\varepsilon_0 = 0.050$ eV, so that an additional term $\delta \sim 0.01$ eV had to be introduced to fit the results to the experimental value 0.06 eV. However, if we use expression (4), we obtain $\varepsilon_0 = 0.058$ eV, and the additional term is not required.

bulk of $3C$-SiC. According to the data of [12], the values of the static permittivity are $\varepsilon_{st}(3C) = 9.72$ and $\varepsilon_{st}(6H) = 10.03$ and 9.66 in the directions parallel and orthogonal to the crystallographic axis **c**, respectively. We take the averaged value $\varepsilon_{st}^*(6H) = (10.03 \times 9.66^2)^{1/3} = 9.78$. We assume that the value of ε_{st} for the $4H$ polytype is equal to the static permittivity of the $6H$ polytype. As far as we know, there are no data on ε_{st} for $2H$-SiC. Therefore, for further estimations, we set $\varepsilon_{st}(2H) = 9.78$.

As follows from formula (4), for comparison of the values of ε_0 for different heterojunctions, we should compare the corresponding values of $\eta \equiv F^{2/3}$. For definiteness, we assume that all of the NH polytypes are doped to contain equal concentrations of electrons n_0 in the sample bulk. In addition, we assume that the $3C$-SiC samples involved in all of the heterojunctions contain the same concentration of holes p_0. We also disregard the difference between $\varepsilon_{st}(3C) = 9.72$ and $\varepsilon_{st}(NH) = 9.78$. Then we have $\eta \approx U^{1/3}$. With the experimental value $\varepsilon_0 = 0.060$ eV [3] and the quantities U_{max}, we find that $\varepsilon_0 = 0.059, 0.062$, and 0.066 eV for the case of $8H$-, $4H$-, and $2H$-SiC. There are virtually no differences between the energies of the levels ε_0 in the QWs in $3C$-SiC in contact with the $8H$-, $6H$-, and $4H$-SiC polytypes. In the case of $2H$-SiC, the difference is noticeable. However, it should be remembered that experimental data on this polytype are scarce. Nevertheless, from the above analysis, it can be argued that the energy level ε_0 can be controlled efficiently only by doping.

REFERENCES

1. A. Fissel, Phys. Rep. **379**, 149 (2003).
2. A. A. Lebedev, A. M. Strel'chuk, D. V. Davydov, *et al.*, Pis'ma Zh. Tekh. Fiz. **28** (18), 89 (2002) [Tech. Phys. Lett. **28**, 792 (2002)].
3. A. A. Lebedev, A. M. Strel'chuk, N. S. Savkina, *et al.*, Pis'ma Zh. Tekh. Fiz. **28**, 78 (2002) [Tech. Phys. Lett. **28**, 1011 (2002)].
4. A. Fissel, U. Kaizer, B. Schröter, *et al.*, Appl. Surf. Sci. **184**, 37 (2001).
5. T. Bechshtedt and R. Enderlein, *Semiconductor Surfaces and Interfaces. Their Atomic and Electronic Structures* (Akademie, Berlin, 1988; Mir, Moscow, 1990).
6. A. N. Andreev, A. S. Tregubova, M. P. Shcheglov, *et al.*, Fiz. Tekh. Poluprovodn. (St. Petersburg) **29**, 1828 (1995) [Semiconductors **29**, 955 (1995)].
7. M. J. Bazack, Phys. Status Solidi B **202**, 549 (1997).
8. *Physical Quantities. A Reference Book*, Ed. by I. S. Grigor'ev and E. Z. Meĭlikhov (Énergoatomizdat, Moscow, 1991) [in Russian].
9. N. D. Sorokin, Yu. M. Tairov, V. F. Tsvetkov, and M. A. Chernov, Kristallografiya **28**, 910 (1983) [Sov. Phys. Crystallogr. **28**, 539 (1983)].
10. A. A. Lebedev, Fiz. Tekh. Poluprovodn. (St. Petersburg) **33**, 769 (1999) [Semiconductors **33**, 707 (1999)].
11. R. G. Verenchikova, V. I. Sankin, and E. I. Radovanova, Fiz. Tekh. Poluprovodn. (Leningrad) **17**, 1757 (1983) [Sov. Phys. Semicond. **17**, 1123 (1983)].
12. V. I. Gavrilenko, A. M. Grekhov, D. V. Korbutyak, and V. G. Litovchenko, *Optical Properties of Semiconductors* (Naukova Dumka, Kiev, 1987) [in Russian].
13. Yu. Goldberg, M. E. Levinstein, and S. L. Rumyantsev, in *Properties of Advanced Semiconductor Materials GaN, AlN, InN, BN, SiC, SiGe*, Ed. by M. E. Levinstein, S. L. Rumyantsev, and M. S. Shur (Wiley, New York, 2001).
14. G. B. Dubrovskii, A. A. Lepneva, and E. I. Radovanova, Phys. Status Solidi B **57**, 423 (1973).
15. T. Ando, A. B. Fowler, and F. Stern, *Electronic Properties of Two-Dimensional Systems* (Am. Phys. Soc., New York, 1982; Mir, Moscow, 1985).
16. V. Ya. Demikhovskiĭ and G. A. Vugal'ter, *Physics of Quantum-Mechanical Low-Dimensional Structures* (Logos, Moscow, 2000) [in Russian].
17. V. M. Galitskiĭ, B. M. Karnakov, and V. I. Kogan, *Problems in Quantum Mechanics* (Nauka, Moscow, 1992) [in Russian].
18. V. L. Bonch-Bruevich and S. G. Kalashnikov, *Physics of Semiconductors* (Nauka, Moscow, 1977) [in Russian].

Translated by É. Smorgonskaya

SEMICONDUCTOR STRUCTURES, INTERFACES, AND SURFACES

Measurement of Micrometer Diffusion Lengths by Nuclear Spectrometry

N. B. Strokan*, A. M. Ivanov*^, A. A. Lebedev*, M. Syväjärvi**, and R. Yakimova**

*Ioffe Physicotechnical Institute, Russian Academy of Sciences, St. Petersburg, 194021 Russia
^e-mail: alexandr.ivanov@mail.ioffe.ru
**Linköping University, S-581 83 Linköping, Sweden
Submitted April 20, 2005; accepted for publication May 4, 2005

Abstract—A method for determination of diffusion lengths in the range 0.5–50 μm, which corresponds to carrier lifetimes in the nanosecond range, is suggested A calibrated nonequilibrium charge is injected into the base of the reverse-biased diode structure. The injection is provided by alpha particles generated by natural decay in the single-particle counting mode. The nuclear spectrometry technique is used to measure the amount of charge that diffused across the base to the boundary of the electric-field region. The loss of charge during the diffusion is calculated as a function of the depth of alpha particle penetration beyond the electric-field region. The derived power-law functions make it possible to relate the diffusion length with the exponent and numerical factor that describes the loss of charge. The experiment is performed with lightly doped 4*H*-SiC epitaxial films.
© 2005 Pleiades Publishing, Inc.

1. INTRODUCTION

The diffusion length L_D is directly related to the carrier lifetime τ by the well-known expression $L_D = (D\tau)^{1/2}$, where D is the diffusion coefficient. Therefore, in explaining the principles of the method of L_D determination, we will also use the equivalent parameter τ. There exist several methods for determination of L_D and τ. The light-probe technique and conductivity modulation [1] are known for materials, and injection–extraction methods [2], for devices with *p–n* junctions. As applied to measurements of short τ, these methods are generally reliable as far as in the submicrosecond range. At the same time, there exist applications (see, e.g., [3]) demanding the determination of much smaller values. In particular, this refers to devices and materials exposed to radiation. We describe a method that allows measurements of lifetime in a range extending down to nanoseconds in structures with Schottky barriers.

2. SUBSTANTIATION OF THE METHOD

The principal idea of the method is allied to the injection–extraction technique offered in [4]. As follows from the name of this technique, at the first stage, a charge of nonequilibrium carriers is injected into the base of a forward-biased diode. Further, the reverse bias is applied to the diode, and the stage of reverse current with a typical plateau in the plot of the current against time is analyzed. Evidently, the duration of the switching pulse edge must be less than the measured τ. This condition demands using high-frequency instruments in the measurements of small τ. If the experimental conditions are changed so that a static reverse bias is applied to the diode, a short-edge injection pulse is demanded.

At the same time, there exists a fairly simple technique providing "flash" injection of a strictly calibrated amount of charge (which is especially important). This kind of injection occurs upon stopping of nuclear particles in a semiconductor.

We consider the ionization induced by alpha particles in a structure with a reverse-biased Schottky barrier in an *n*-type material. Figure 1 shows the distribution of the ionization energy losses for an alpha parti-
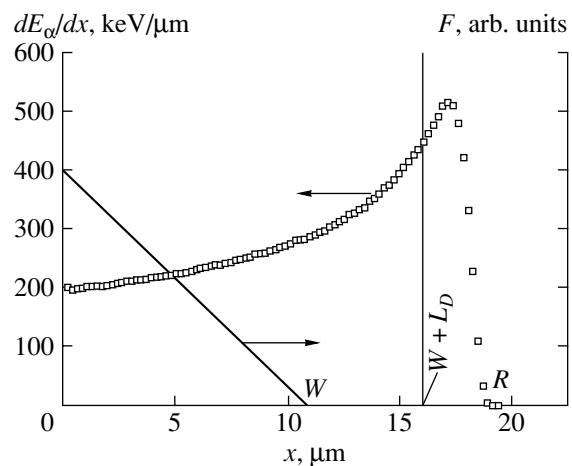

Fig. 1. Specific ionization energy losses for alpha particles in SiC and the electric-field strength in the base of the reverse-biased diode structure. The energy of alpha particles $E_\alpha = 5.4$ MeV; R is the track length; W is the boundary of the field region; and L_D is the diffusion length.

cle, dE_α/dx (proportional to the density of nonequilibrium carriers), and the electric field $F(x)$ along the particle track. The ionization is described by the Bragg curve and increases superlinearly near the end of the particle track (at R). In contrast, the electric-field strength $F(x)$ decreases linearly away from the surface, reaching zero at $x = W$. Therefore, only carriers induced in the region $[0–W]$ are transported to electrodes by fast drift. In the remaining region $[R–W]$, where the ionization peak is located, holes diffuse slowly to the boundary of the field region, experiencing recombination loss and capture by traps.

Let q_0 be the amount of charge generated by a particle, and let q be the recorded charge. Evidently, the loss $\lambda = (q_0 – q)/q_0$ depends on two parameters: the depth of the track penetration beyond the boundary of the field region, $a = R–W$, and the hole diffusion length itself.

We suggest determining the theoretical dependence $\lambda = f(L_D, a)$ and constructing the set of calculated values of this function. In the experiment, we suggest to control the values of a by changing the position of the boundary of the field region, W, via the variation of the bias voltage, and measure the amount of charge q by means of the nuclear spectroscopy technique, using low-frequency electronic devices.

Qualitatively, it is clear that the loss $\lambda = f(L_D, a)$ will be an increasing function of a and will decrease as L_D increases. The final form of this function can be obtained, taking into account the Bragg distribution, by numerical calculation.

3. CALCULATION OF THE RECORDED CHARGE

To determine the function $\lambda = f(a)$ with the parameter L_D, we use the results from [5], where the solution of the diffusion equation for holes in the diode base led to the expression for the loss of charge:

$$\lambda(a) = \frac{\int_0^{R-W} g(x-W)\{1 - \exp[-(x-W)/L_D]\}d\{x-W\}}{\int_0^R g(x)dx}. \quad (1)$$

Here, the function $g(x)$ describes the specific ionization loss of energy by an alpha particle for ionization along the particle track. Figure 1 shows the Bragg function for the energy of the alpha particles used (5.4 MeV), calculated using TRIM code [6].

(i) *For generation equiprobable throughout the volume*, $g(x) = $ const, and formula (1) yields the following well-known expression for the normalized charge at $W = 0$:

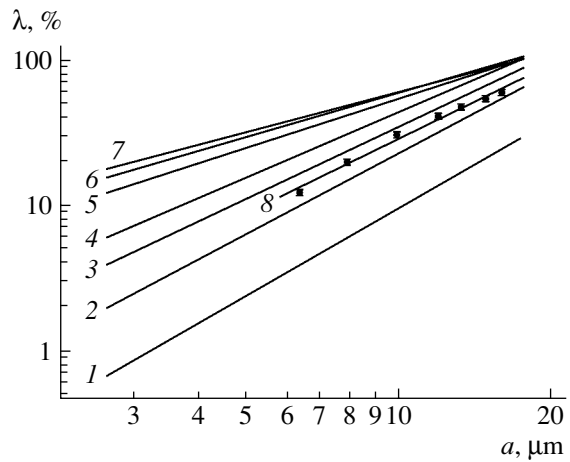$$q/q_0 = (L_D/R)[1 - \exp(-R/L_D)]. \quad (2)$$

Fig. 2. Loss of charge as a function of the length of the part of the alpha particle track that extends beyond the region of the electric field. (*1–7*) Calculation for a diffusion length constant along the sample for $L_D = $ (*1*) 30.0, (*2*) 10.0, (*3*) 5.0, (*4*) 3.0, (*5*) 1.0, (*6*) 0.5, and (*7*) 0.2 μm. (*8*) Experimental data for the 4*H*-SiC film.

Two limiting cases are illustrative. At $R \gg L_D$, when the generation region is larger than the diffusion length, the signal is directly proportional to L_D: $q/q_0 = L_D/R$. In the opposite situation, when $L_D \gg R$, we can assume that the generation of charge occurs at $R/2$, and $q/q_0 \approx 1 - R/2L_D$.

(ii) *To take into account the shape of the Bragg curve*, it is necessary to calculate the integral (1) numerically for a set of L_D values. It is important that, in calculating the integral, it is also possible to take into consideration the coordinate dependence of the parameter L_D. The $L_D = f(x)$ dependence appears, for example, when materials are irradiated with accelerated ions. A considerable increase in the number of primary structural defects near the end of the track is typical of irradiation with ions. Radiation-induced defects are actively involved in carrier capture, and, therefore, L_D becomes a function of coordinate.

As an example, we analyze the data [7] where SiC films were irradiated with 710-MeV Bi ions. The analysis shows that, under the experimental conditions of [7], the number of primary defects, N_{def}, on the film sides differed threefold. The calculated function $N_{def}(x)$ is approximated by a cubic parabola. Assuming that the lifetime τ is determined only by the introduced N_{def}, we obtain the dependence $L_D \propto [N_{def}(x)]^{-1/2}$. In this case, the L_D values on the film sides differ by a factor of $\sqrt{3}$. It seems interesting to determine the sensitivity of our method to the $L_D(x)$ profile using the discussed experiment as an example.

On this basis, integral (1) was calculated for $L_D = 0.1–30$ μm, for two cases: $L_D = $ const, or $L_D \propto [N_{def}(x)]^{-1/2}$, where $N_{def}(x)$ is a cubic polynomial. Figure 2 shows on the log–log scale the set of functions $\lambda = f(a)$ for the
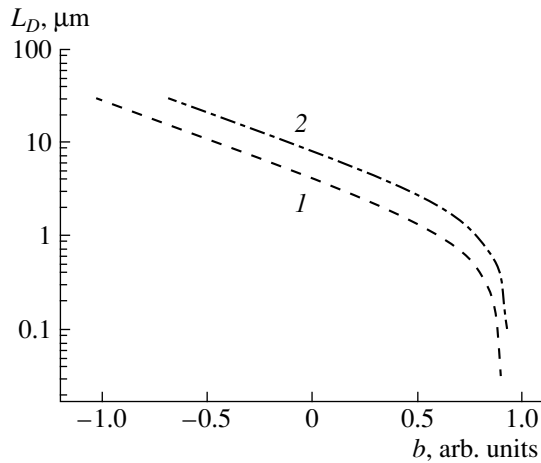
L_D, μm

Fig. 3. Calculated diffusion length of holes as a function of the loss of charge, determined as the intercept on the ordinate axis in Fig. 2. (*1*) L_D is constant along the sample depth; (*2*) L_D decreases away from the surface by the cubic parabolic law.
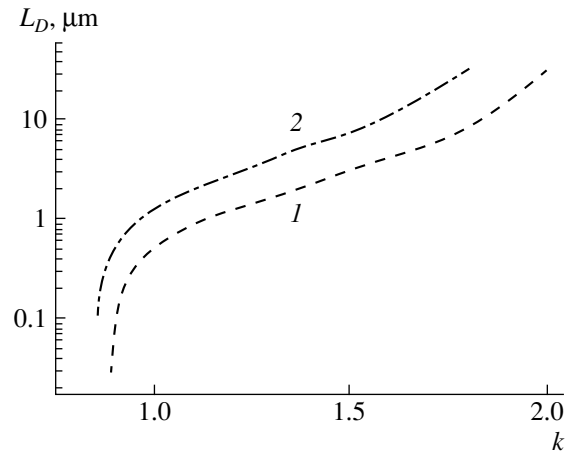

Fig. 4. Calculated diffusion length of holes as a function of the slope of the dependences in Fig. 2. (*1*) L_D is constant along the sample depth; (*2*) L_D decreases away from the surface by the cubic parabolic law.

first case, L_D = const. A similar dependence is obtained also for the case of $L_D(x)$ dependence. In both cases, we obtain a linear relation

$$\log \lambda \ = \ b + k \log a, \qquad (3)$$

which allows us to obtain, having determined the adjustable parameters b and k, the auxiliary dependences of L_D on b and k (see curves *1* and *2* in Figs. 3 and 4, respectively).

First, Figs. 3 and 4 clearly indicate the applicability limits of the method. For the used depth of particle tracks of $R \approx 20$ μm, the lower limit of measurable L_D is $L_D \approx 0.5$ μm, which corresponds to less than a nanosecond τ for holes ($D = 3$ cm²/s).

Second, a significant difference in the b and k values is observed between the cases of L_D = const and an L_D decreasing across the film thickness. In the presented example, the shape of the $L_D(x)$ dependence was predictable. Therefore, in the experiment, it is possible to determine L_D on the sample surface correctly and then calculate the $L_D(x)$ dependence across the film thickness.

4. EXPERIMENTAL

We studied CVD-grown 4*H*-SiC films. The film thickness was 35 μm, the doping level $N_d - N_a = (4–8) \times 10^{14}$ cm⁻³. SiC films with these parameters can be considered as pure. Another no less important indicator of the high quality of the films is the value of $L_D(\tau)$ of minority carriers (holes).

As discussed above, in the SiC films, Schottky barriers were formed with contact layers produced by thermal evaporation in a vacuum of Al and Cr. A nonequilibrium charge was injected by alpha particles in the single-particle counting mode with a rate of ~200 s⁻¹. The charge of a particle entering the sample was

recorded using the standard spectrometric technique, with a time of signal formation of 1–3 μs. The experimental setup included ORTEC units: a model 142 charge-sensitive preamplifier, a model 571 amplifier with a passband formed by *RC* circuits, and a model 419 precision generator.

The amplitude spectrum was analyzed using a 4000-channel RI-161/01 board (developed at the St. Petersburg Institute of Nuclear Physics, Russian Academy of Sciences) coupled to a computer. The scale factor of the channels was determined using ²²⁶Ra alpha decay lines and a precision Si detector (Ioffe Physicotechnical Institute) [8].

In the experiment, the signal E from alpha particles with the energy $E_\alpha = 5.4$ MeV was recorded as a function of the reverse bias U applied to the structure (Fig. 5). The contact potential was assumed to be 1 V. Additionally, the capacitance–voltage characteristic was measured and the size of the field region, W, was determined. A value $N_d - N_a = 6.7 \times 10^{14}$ cm⁻³ was obtained for the concentration of uncompensated donors in the SiC film.

The signal deficiency ($E_\alpha - E$) caused by the loss of charge ($q_0 - q$) was normalized to the energy E_α. For comparison with the results of calculations, the obtained values of $\lambda = (E_\alpha - E)E_\alpha = (q_0 - q)/q_0$ were plotted as a function of $a = R-W$ also on a log–log scale (see Fig. 2).

The experimental results fall into the range of calculated values of $L_D = 5.0–10.0$ μm. For data processing in a more sophisticated way than a simple superposition on the grid in Fig. 2, we used the dependences $L_D(b)$ and $L_D(k)$. According to calculated curves in Figs. 3 and 4, the values of b and k determined from the experiment correspond to the diffusion length $L_D = 6.22$ and 6.08 μm, respectively. Thus, we obtain the average $L_D =$

6.15 μm, which corresponds to the hole lifetime $\tau = 126$ ns at $D = 3.0$ cm^2/s.

5. DISCUSSION

First, several specific features of the method must be noted.

(i) Carrier-capturing centers may be of varied nature. They can manifest themselves not only in recombination, but also in carrier trapping. The suggested method does not distinguish these cases if the time of hole emission from a trapping center is longer than the time of signal formation in the spectrometric circuits. It is important for the method that holes cannot be involved in the diffusion toward the boundary of the electric-field region in the structure.

(ii) A question arises concerning the filling of the capture levels in the experimental conditions. Here, it should be borne in mind that the diameter of the alpha-particle track is 10 μm, so that the track area is a small fraction of the sample surface area. For the sample areas and counting rates used in our experiment, incidence of one more particle at a certain point becomes possible after ~60 s. Therefore, filling of a level (with this level not involved in further capture) can be important only for levels with hole emission times over 1 min. Assuming that the hole capture cross section is 10^{-15} cm^2, we estimate the energy depth of such a level as 0.75 eV.

(iii) It is necessary to note that the value of L_D can be estimated directly from the data presented in Fig. 5 in the following simplified interpretation. The signal from the structure includes two components related to transport of carriers via drift and diffusion in the regions W and L_D, respectively. Therefore, the recorded energy can be presented as the sum:

$$E = (dE_\alpha/dx)_W W + (dE_\alpha/dx)_{L_D} L_D. \qquad (4)$$

Here, subscripts W and L_D indicate that the average value of the ionization loss dE_α/dx should be taken for the W and L_D regions, respectively. Indeed, a prolonged linear portion is observed, owing to the dependence $W \propto U^{1/2}$, before the leveling-off of the dependence in Fig. 5. According to (4), the intercept on the energy axis at $U \longrightarrow 0$ is related to the diffusion charge transport. If the linearly ascending portion is entirely attributed to an increase in $W \propto (N_d - N_a)^{-1/2}$, we can estimate the concentration of uncompensated impurities without capacitance measurements.

The values $L_D = 6.32$ μm and $N_d - N_a = 3.6 \times 10^{14}$ cm^{-3} were obtained from the data presented in Fig. 5. The concentration is markedly underestimated, compared with the value obtained from the capacitance measurements, $N_d - N_a = 6.7 \times 10^{14}$ cm^{-3}. This difference is accounted for by the fact that the linear approximation of data in Fig. 5 attributes the total signal increase to the increase in W. In reality, a considerable additional contribution is made, according to the
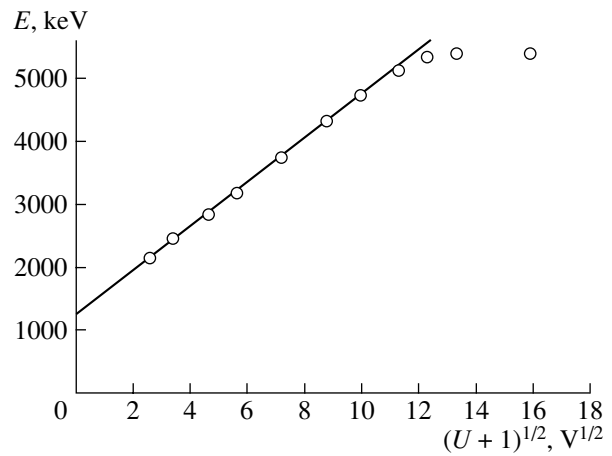

Fig. 5. Signal as a function of the reverse bias applied to the sample. The energy of alpha particles $E_\alpha = 5.4$ MeV, and the assumed contact potential is 1 V. The linear approximation of the initial portion allows the estimation of L_D.

dE_α/dx curve in Fig. 1, by an increase in ionization with the coordinate, which is disregarded in the mathematical processing used.

In the case under consideration, the values of L_D appeared to be close to those obtained in measurements and calculation of the integral (1). Nevertheless, deviations would be expected in the case of larger L_D, when the nonlinearity (the Bragg curve) will also affect the diffusion component of the signal. Furthermore, the extrapolation of the signal to $(U, W) \longrightarrow 0$ hampers the consideration of the possible L_D dependence on the coordinate.

6. CONCLUSION

Several practically important issues should be emphasized.

It is essential that the use of the suggested method does not require that a diode structure should have a high-quality reverse I–V characteristic. The average value of the amplitude spectrum is measured, which allows considerable noise of the reverse current. Therefore, structures with a Schottky barrier can be used, in which case only slight thermal treatment is needed. Schottky barriers are unsuitable for a closely related injection–extraction method because of the uncertainty in the injection coefficient, and more complicated technological operations must be used.

In addition, particles of different energies can be used, for which the variation in the loss of charge will be related to the difference in track lengths. In this mode, it is adequate to use only a single (and possibly small) value of the bias voltage applied to the structure.

In essence, the described method is close to the injection–extraction method, it operates with the charge transferred in the course of spreading of the initially introduced packet of carriers. However, in the sug-

gested method only the amount of charge in some specific "reverse phase" is important, with the shape of the pulse being insignificant. The latter circumstance makes it possible to determine the nanosecond lifetimes using a low-frequency amplifier. We believe that use of alpha particles with lower energies can extend the method to the subnanosecond range.

REFERENCES

1. A. I. Kurnosov, *Materials for Semiconductor Devices and Integrated Microcircuits* (Vysshaya Shkola, Moscow, 1980), p. 327 [in Russian].

2. Yu. R. Nosov, *Switching in Semiconductor Diodes* (Nauka, Moscow, 1968; Plenum, New York, 1969), p. 263.

3. V. V. Tigatov and P. A. Gnatyuk, Fiz. Tekh. Poluprovodn. (St. Petersburg) **39**, 378 (2005) [Semiconductors **39**, 360 (2005)].

4. B. Lax and S. Neustadter, J. Appl. Phys. **25**, 1148 (1954).

5. I. N. Il'yashenko and N. B. Strokan, Fiz. Tekh. Poluprovodn. (St. Petersburg) **30**, 302 (1996) [Semiconductors **30**, 167 (1996)].

6. *Ion Implantation: Science and Technology*, Ed. by J. F. Ziegler (Academic, Orlando, 1984).

7. E. V. Kalinina, G. F. Kholuyanov, G. A. Onushkin, *et al.*, Fiz. Tekh. Poluprovodn. (St. Petersburg) **38**, 1223 (2004) [Semiconductors **38**, 1187 (2004)].

8. V. K. Eremin, E. M. Verbitskaya, N. B. Strokan, *et al.*, Zh. Tekh. Fiz. **56**, 1987 (1986) [Sov. Phys. Tech. Phys. **31**, 1186 (1986)].

Translated by D. Mashovets

SEMICONDUCTOR STRUCTURES, INTERFACES, AND SURFACES

Light-Emitting Si:Er Structures Produced by Molecular-Beam Epitaxy: High-Resolution Photoluminescence Spectroscopy

D. I. Kryzhkov*, N. A. Sobolev**^, B. A. Andreev*, D. V. Denisov**,
Z. F. Krasil'nik*, and E. I. Shek**

*Institute of the Physics of Microstructures, Russian Academy of Sciences, Nizhni Novgorod, 603600 Russia
**Ioffe Physicotechnical Institute, Russian Academy of Sciences, St. Petersburg, 194021 Russia
^e-mail: nick@sobolev.ioffe.rssi.ru

Abstract—The photoluminescence spectra of light-emitting structures based on silicon layers doped with erbium in the course of growth by molecular-beam epitaxy at temperatures ranging from 400 to 700°C are studied at 77 K with a resolution of no worse than 1 cm^{-1}. For the layers grown at the temperatures ≤500°C, the narrow lines related to erbium are dominant in the spectra. The full width at the half-maximum of these lines is no larger than 9 cm^{-1}. In this case, at least two types of centers involving the Er^{3+} ions and carbon impurity are observed. For the layers grown at higher temperatures of epitaxial growth, the broader lines (≥40 cm^{-1}) corresponding to the Er^{3+} ions in the SiO$_x$ precipitates are dominant in the spectra. The dependence of the integrated intensity of photoluminescence of the Er-related centers on the temperature of epitaxial growth is represented by a curve with a peak at 500°C. © 2005 Pleiades Publishing, Inc.

1. INTRODUCTION

One of the most extensively used methods for producing light-emitting silicon single crystal layers doped with erbium is molecular beam epitaxy (MBE). The development and study of the properties of light-emitting Si:Er structures grown by MBE have been reported in a rather large number of papers [1–7]. Much less attention has been given to identification of optically active centers and to the effect of technological conditions on the structure of these centers. In [5], it was established that additional doping with oxygen or carbon impurities at relatively low temperatures of epitaxy (430°C) was accompanied by changes in the intensity and position of the major line in the photoluminescence (PL) spectra of the Er^{3+} ion. In this case, the spectra are represented by rather narrow lines. Markmann *et al.* [5] attribute the changes in the spectral position and intensity of the lines to changes in the type and arrangement of the dopant that is referred to as an activator. In contrast to [5], Serna *et al.* [2] studied the influence of the oxygen dopant on the PL spectra of layers grown at higher temperatures (600°C). A change in the shape of the spectrum, along with an increase in the intensity of the major peak, was observed [2]. However, this experimentally observed transformation of the spectrum was also attributed only to the changes in the arrangement of the oxygen atoms [2]. At the same time, a more comprehensive analysis shows that the experimental spectrum (see Fig. 2 in [2]) looks, to a greater extent, like the spectra of the Er^{3+} ions in SiO$_x$ precipitates in the silicon matrix [8]. When analyzing the radical differ-

ences in the structure of luminescence centers [5, 2], we speculated that these changes correlated with the temperature of growth. This hypothesis was based on the dependence of the structure of the Ho^{3+} ion centers on the temperature of postimplantation annealing of the Si:Ho samples [9]. Based on the available studies [6, 7], in which the Si:Er layers were grown by MBE in a wide temperature range, we cannot confirm or rule out the above hypothesis because the experimental setup used in [6, 7] had an inadequate spectral resolution. The data reported in [7] are of interest due the observation of simultaneous doping with the oxygen and carbon impurities during the MBE growth of the Si:Er layers. The aim of this study is to investigate, with high resolution, the PL spectra of the Si:Er layers grown by MBE at different substrate temperatures and doped with oxygen and carbon dopants.

2. EXPERIMENTAL

The Si:Er layers were grown with the use of a SUPRA-32 (RIBER) setup in vacuum (~8 × 10^{-9} Torr) on the (100)-oriented substrates cut off from an *n*-type silicon crystal grown by the Czochralski method (*n*-Cz-Si). The resistivity of the substrates was ρ = 4.5 Ω cm. Silicon produced by the crucible-free floating-zone method (*n*-FZ-Si) with the resistivity ρ = 2 Ω cm was evaporated using an electron-beam evaporator. Metal Er was evaporated from an effusion cell. The epitaxial growth of the layers was carried out at a constant substrate temperature in the range *T* = (400–700)°C; the
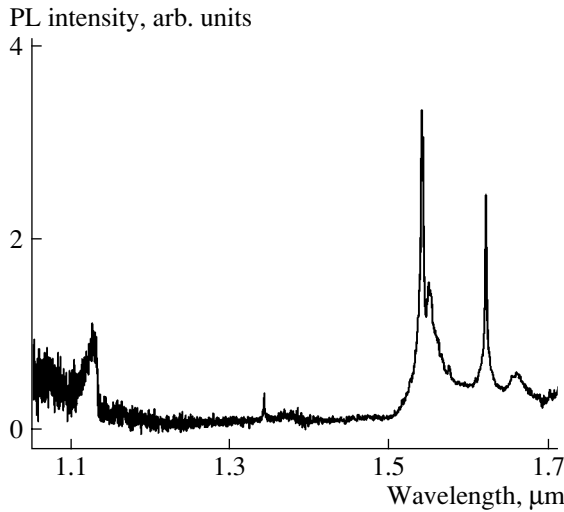
PL intensity, arb. units

Fig. 1. The photoluminescence spectrum of the Si:Er sample grown at the substrate temperature 500°C. The spectral resolution is 2 cm^{-1}.
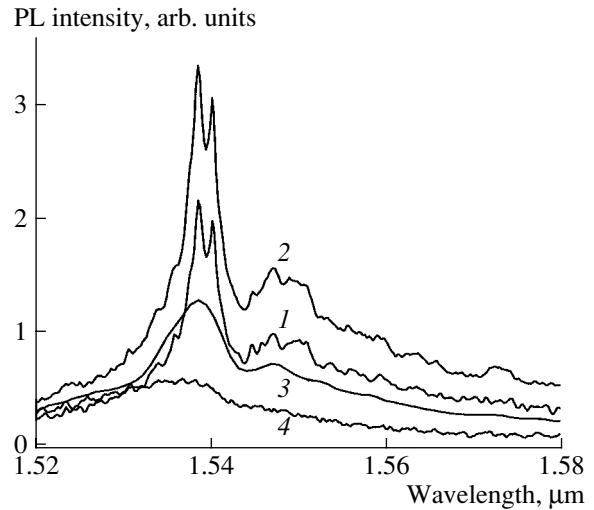
PL intensity, arb. units

Fig. 2. The photoluminescence spectra of the Si:Er samples grown at substrate temperatures T = (*1*) 400, (*2*) 500, (*3*) 600, and (*4*) 700°C. The spectral resolution is 2 cm^{-1}.

deposition rate was about ~0.6 Å/s. The concentration of Er atoms in the epitaxial layer was [Er] $\approx$ 2 $\times$ 10^{19} cm^{-3}, as measured by the Rutherford backscattering spectrometry. As measured by secondary-ion mass spectroscopy, the concentrations of the oxygen and carbon dopants in the epitaxial layer were [O] $\approx$ 2.0 $\times$ 10^{18} cm^{-3} and [O] $\approx$ 3.0 $\times$ 10^{17} cm^{-3}, that is, lower than the concentration of the Er atoms, but much higher that the concentrations in the substrate. The thickness of the epitaxial layers ranged up to 1.3 μm. The conditions of growth of the Si:Er layers to be studied were described in detail in [7].

The PL spectra were measured at a temperature of 77 K with a resolution of no worse than 2 cm^{-1}. A Bomem DA3 Fourier spectrometer operating in the range 5600–10000 cm^{-1} was used for recording the spectra. The spectrometer was equipped with a Ge photodetector whose detectability was no lower that 5 $\times$ 10^{12} cm Hz$^{1/2}$ W^{-1}. The PL was excited by radiation of a 400-mW argon laser at a wavelength of 514 nm.

3. RESULTS AND DISCUSSION

Figure 1 shows the PL spectrum of a sample grown at the temperature of 500°C. Three groups of lines are dominant in the spectrum. A series of lines in the range around 1.54 μm is caused by the radiative transitions of the Er^{3+} ions from the first excited state $^4I_{13/2}$ to the ground state $^4I_{15/2}$. The peak of the PL intensity is recorded at the wavelength λ = 1.538 μm. The line at λ = 1.618 μm is attributed to the complex that involves the oxygen and carbon atoms (the so-called *P* line) [10, 11]. The *P* line is identified unambiguously, as evidenced by its phonon replica at λ = 1.655 μm. The third line at λ = 1.127 μm is the line of a free exciton.

Figure 2 shows the PL spectra recorded with a 2 cm^{-1} resolution for the samples grown at different temperatures. A decrease in the temperature of growth T is followed by drastic changes in the spectra. In fact, if $T \le$ 500°, narrow lines whose full width at the half-maximum (FWHM) is $\le$9 cm^{-1} are observed; if is higher, broad lines (with the FWHM $\ge$40 cm^{-1}) similar to the lines of the Er^{3+} ions in the SiO$_x$-like precipitates [8] are dominant in the spectra. In the spectra of the samples grown at lower temperatures, two lines at λ_1 =1.540 μm and λ_2 = 1.538 μm are dominant. It can be assumed that the first line refers to the erbium–carbon center, since a line at λ_1 = 1.540 μm is dominant also in the spectra of samples that were grown by the crucible-free floating-zone method, had a low oxygen content, and were then implanted with carbon ions [12]. In addition, the 1.540 μm line was observed as a dominant line in the spectra of the Si:Er layers grown by MBE at 430°C with carbon introduced in the chamber [5]. At the same time, the second line observed at λ_2 = 1.538 μm is most likely not related to the erbium–oxygen center, since the erbium–oxygen line at λ = 1.537 μm was dominant in the spectra of MBE layers if oxygen was introduced in the chamber, as was shown in the above-mentioned study [5]. In order to refine the position of the erbium-related lines and identify the possible origin of the second dominant line, we recorded the high-resolution (1 cm^{-1}) PL spectra for the samples grown at low temperatures. For the samples grown at both low temperatures, the spectral positions of the PL lines are the same. The PL spectrum of the sample grown at 500°C is shown in Fig. 3. For convenient comparison of the spectrum with the data in the available publications, the photon energy is expressed in cm^{-1}. Vertical lines with squares indicate the spectral position of the well-
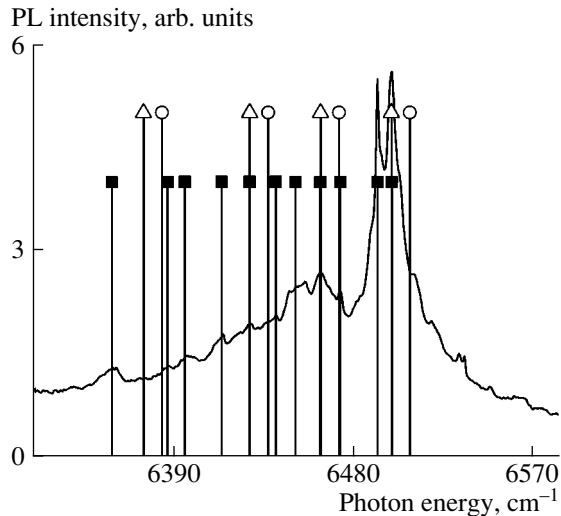
PL intensity, arb. units

Fig. 3. The photoluminescence spectrum of the Si:Er sample grown at the substrate temperature 500°C. The spectral resolution is 1 cm^{-1}. Vertical lines with squares, circles, and triangles indicate the spectral positions of the Er-related lines observed for the sample, of the lines related to the ErO-1 center, and of the ErO-1-related lines shifted to lower energies by 9.3 cm^{-1}, respectively.
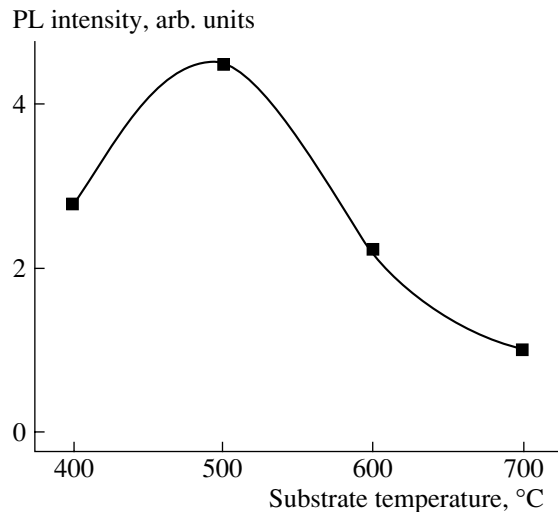
PL intensity, arb. units

Fig. 4. The integrated intensity of photoluminescence of Er-containing centers versus the temperature of epitaxial growth of the Si:Er samples.

resolved lines corresponding to the transitions $^4I_{13/2} \longrightarrow$ $^4I_{15/2}$ of the erbium ions in the sample. Vertical lines with circles indicate the position of the lines of the erbium–oxygen center ErO-1 [13]. The major lines of the ErO-1 center are located at 6508, 6472, and 6437 cm^{-1}; the other lines are of lower intensity and may be undetected. If we shift the lines of the ErO-1 center by 9.3 cm^{-1} (vertical lines with triangles), the first three lines match the 6499, 6463, and 6428 cm^{-1} lines observed in the samples under study. In addition,

the ratio between the intensities of these lines is the same as that of the lines attributed to the ErO-1 center. This effect can be caused by a chemical shift that should appear if the oxygen atoms in the ErO-1 centers are replaced by carbon atoms. The other erbium-related PL lines correspond to some other centers that have not yet been unidentified.

Figure 4 shows the dependence of the integrated intensity of PL of Er-containing centers on the temperature of epitaxial growth. It is reasonable to relate the increase in the PL intensity with temperature to the increase in the rate of quasi-chemical reactions of the Er ions with the dopant activators at the surface of the growing layer. The decrease in the PL integrated intensity at temperatures ≥600°C is apparently due to the fact that one type of the dominant quasi-chemical reactions is replaced by another type. This interpretation is suggested by the appearance of the broad lines in the spectra associated with changes in the nearest surrounding of the Er^{3+} ions (see Fig. 2). It is interesting to note that, as shown in [6], the intensity of electroluminescence of the erbium ions increases with the temperature of MBE growth up to 600°C and then decreases sharply. The authors of [6] argue that the increase in intensity is associated with the increase in the rate of quasi-chemical reactions and the decrease with the formation of the erbium silicide phase. Unfortunately, no data on transformation of Er-related spectral lines are reported in [6].

4. CONCLUSIONS

In summary, the formation of two types of light-emitting centers that are responsible for the narrow and broad PL lines is revealed in the Si:Er layers. The formation of particular centers depends on the MBE temperature that controls the changes in the nearest surrounding of the Er^{3+} ions.

REFERENCES

1. H. Efeoglu, J. H. Evans, T. E. Jackman, *et al.*, Semicond. Sci. Technol. **8**, 236 (1993).

2. R. Serna, J. H. Shin, M. Lohmeier, *et al.*, J. Appl. Phys. **79**, 2658 (1996).

3. J. Stimmer, A. Reittinger, J. F. Nutzel, *et al.*, Appl. Phys. Lett. **68**, 3290 (1996).

4. W.-X. Ni, K. B. Joelsson, C.-X. Du, *et al.*, Appl. Phys. Lett. **70**, 3383 (1997).

5. M. Markmann, E. Neufeld, A. Sticht, *et al.*, Appl. Phys. Lett. **75**, 2584 (1999).

6. C.-X. Du, W.-X. Ni, K. B. Joelsson, *et al.*, Opt. Mater. **14**, 259 (2000).

7. N. A. Sobolev, D. V. Denisov, A. M. Emel'yanov, *et al.*, Fiz. Tverd. Tela (St. Petersburg) **47**, 108 (2005) [Phys. Solid State **47**, 113 (2005)].

8. W. Jantsch, S. Lanzertorfer, L. Palmetshofer, *et al.*, J. Lumin. **80**, 9 (1999).

9. N. A. Sobolev, A. M. Emel'yanov, Yu. A. Nikolaev, *et al.*, Mater. Sci. Eng. B **81**, 176 (2001).

10. N. S. Minaev and A. V. Mudryi, Phys. Status Solidi A **68**, 561 (1981).

11. G. Davies, Phys. Rep. **176**, 176 (1989).

12. F. Priolo, S. Coffa, G. Franzo, *et al.*, J. Appl. Phys. **74**, 4936 (1993).

13. H. Przybylinska, W. Jantsch, Yu. Suprun-Belevich, *et al.*, Phys. Rev. B **54**, 2532 (1996).

Translated by É. Smorgonskaya

SEMICONDUCTOR STRUCTURES, INTERFACES, AND SURFACES

Electrical Properties of *n*-GaN/*p*-SiC Heterojunctions

O. Yu. Ledyaev, A. M. Strel'chuk^, A. N. Kuznetsov, N. V. Seredova, A. S. Zubrilov, A. A. Volkova, A. E. Nikolaev, and A. A. Lebedev

Ioffe Physicotechnical Institute, Russian Academy of Sciences, St. Petersburg, 194021 Russia
^e-mail: Anatoly.Strelchuk@mail.ioffe.ru
Submitted April 26, 2005; accepted for publication May 10, 2005

Abstract—Epitaxial GaN layers were grown by hydride vapor phase epitaxy (HVPE) on commercial (CREE Inc., USA) p^+-6*H*-SiC substrates ($N_a - N_d \approx 7.8 \times 10^{17}$ cm^{-3}) and n^+-6*H*-SiC Lely substrates with a predeposited p^+-6*H*-SiC layer. A study of the electrical properties of the *n*-GaN/*p*-SiC heterostructures obtained confirmed their fairly good quality and demonstrated that the given combination of growth techniques is promising for fabrication of bipolar and FET transistors based on the *n*-GaN/*p*-SiC heterojunctions. © 2005 Pleiades Publishing, Inc.

1. INTRODUCTION

It is known that, owing to their electrical parameters, silicon carbide and gallium nitride are rather promising materials for fabrication of high-power devices, including those for the microwave frequency range. In view of the lack of native single-crystal gallium nitride substrates for homoepitaxial growth, most nitride devices are fabricated by epitaxial deposition on foreign substrates. Sapphire (Al$_2$O$_3$) and silicon carbide are mostly used for this purpose, with silicon carbide being a preferable substrate material for heteroepitaxy of gallium nitride, compared with sapphire. The lattice mismatch between GaN and SiC is ~3.5%, compared to 16% between GaN and sapphire; the thermal expansion coefficients (TEC) of GaN and SiC are rather close to each other, whereas the TEC of sapphire is 1.5–2 times that of GaN (depending on the crystallographic direction). The thermal conductivity of SiC is nearly 10 times that of Al$_2$O$_3$.

The stress at the interface between two materials is commonly reduced, and the nucleation between the substrate and the growing layer, improved, by the growth of thin epitaxial GaN or AlN layers at low temperatures. It has been shown that heterojunctions can be fabricated by the growth of GaN directly on SiC [1–6]. In addition, the possibility of fabricating an *n*-GaN/*p*-6*H*-SiC/*n*-SiC heterobipolar transistor has been demonstrated [7]. According to [7], the transistor had a current gain of ~10^6 and could operate at temperatures as high as ~260°C. However, the attempts of other research groups to reproduce these results have failed, which is possibly due to the high defect density in *p*-6*H*-SiC [4].

2. EXPERIMENTAL

The epitaxial GaN layers under study were grown by hydride vapor-phase epitaxy (HVPE) [8] on commercial (CREE Inc., USA) p^+-6*H*-SiC substrates ($N_a - N_d \approx 7.8 \times 10^{17}$ cm^{-3}) and n^+-6*H*-SiC Lely substrates with a p^+-6*H*-SiC layer ($N_a - N_d \approx 3 \times 10^{18}$ cm^{-3}, thickness ~5 μm) preliminarily deposited by sublimation epitaxy in a vacuum [9]. The epitaxy of GaN was performed directly on a SiC substrate without preliminary growth of any buffer layer [10]. The nominally undoped GaN layers were of the *n*-type and had a concentration of uncompensated donors of ~(2–4) × 10^{17} cm^{-3}. The layer thickness was ~0.8 μm.

The optical properties of the layers were studied by the photoluminescence (PL) method. The luminescence in the layers was excited with a pulsed nitrogen laser (wavelength 337.1 nm, pulse power 2 kW, and pulse-repetition frequency 100 Hz). The PL spectra were measured at 77 K, using a spectrometer with a resolution of about 2 nm. A typical low-temperature PL spectrum of the layers is shown in Fig. 1. The predominant peak in the spectrum corresponds to optical transitions of donor-bound excitons (DBE), which is characteristic of high-quality epitaxial GaN layers. This inference is also supported by the narrow FWHM of this band (41–44 meV). A minor red shift of the DBE band in the layers, relative to that in the PL spectrum of unstrained bulk GaN, was attributed to the effect of tensile stresses in the epitaxial layer in directions perpendicular to the *C* axis [11, 12]. In addition to the DBE band, low-intensity donor–acceptor (D–A) bands of GaN can be observed in the spectra (together with their phonon replicas) at 380–420 nm, as well as a band with a characteristic structure at 440–540 nm. The latter band was interpreted as due to luminescence from the SiC substrate, because the PL in this part of the spectrum coincided with that of the substrate (see Fig. 1).

To study the electrical properties of *n*–*p* heterojunctions, mesa structures with diameters of 100, 200, and 1500 μm were formed by plasmochemical etching of
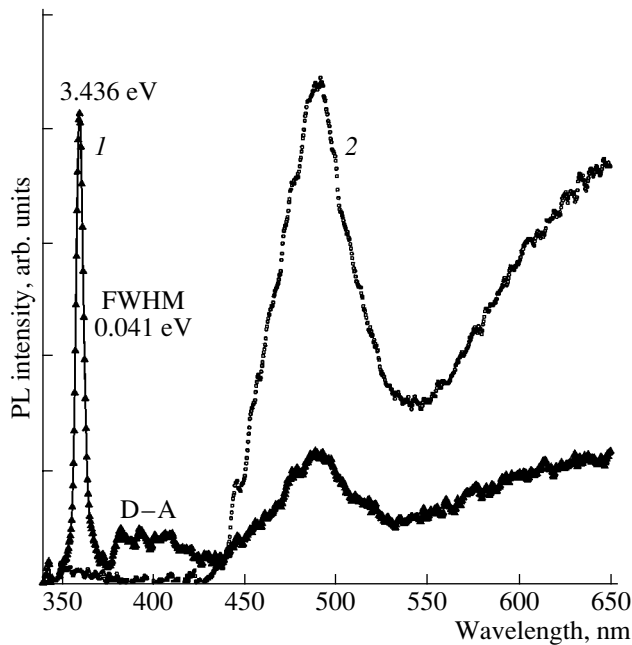
Fig. 1. PL spectra at 77 K: (*1*) GaN/SiC epitaxial structure and (*2*) SiC substrate.

Fig. 2. *C–V* characteristics of an *n–p* GaN/SiC heterostructure. Sinusoidal measurement frequencies: (*1*) 10 and (*2*) 1 kHz.

the epitaxial structures under study in the plasma of Freon-12 gas. Nickel served as a mask in the etching. Nickel was also used to fabricate ohmic contacts to *n*-GaN and *n*-SiC. To obtain an ohmic contact to *p*-SiC, a Ti/Al/Ni alloy was deposited onto the semiconductor surface and then the samples were annealed in a vacuum.

3. RESULTS

The electrical properties of GaN/SiC heterostructures were studied by measuring their current–voltage (*I–V*) and capacitance–voltage (*C–V*) characteristics at room temperature. The *C–V* characteristics of the *n−p* GaN/SiC heterostructures were measured at frequencies of 1 and 10 kHz (Fig. 2). These characteristics were linear in the $(1/C^2)$–(*V*) representation up to reverse voltages of ~12V. The linearity of the characteristics and the coincidence of the concentrations N_d–N_a with the values obtained for the epitaxial GaN layer before formation of a mesa structure indicate that the heterojunction is abrupt and asymmetric. The capacitance cutoff voltage was 2.24 V at a frequency of 1 kHz and 2.28 V at 10 kHz. These values are close to the published data for the contact potential difference for the *n*-GaN/*p*-SiC heterostructure [3].

The *I–V* characteristics obtained were of a clearly pronounced diode type (reverse and forward *I–V* characteristics of the heterostructures are shown in Fig. 3). The maximum reverse voltage depended on the diode area and increased as the area decreased, to become ~60 V for samples with the smallest area. The forward *I–V* characteristics were nonlinear at high currents, and
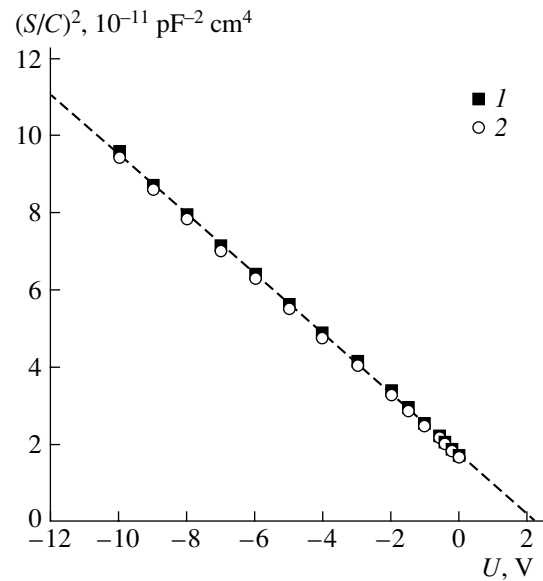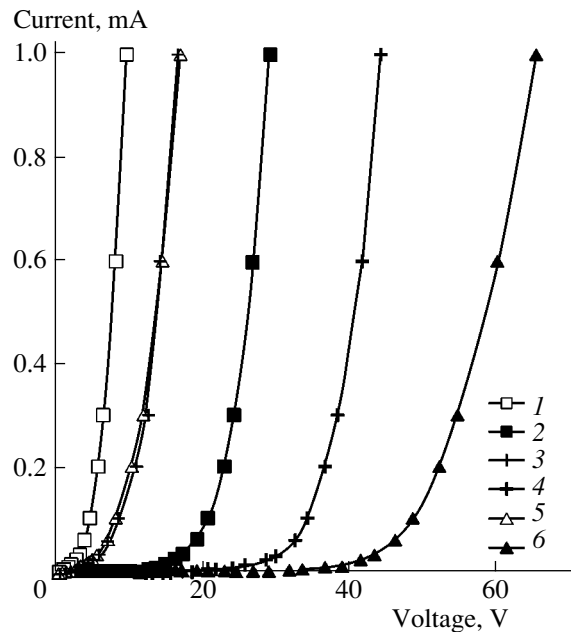

Fig. 3. (*1*, *3*, *5*) Forward and (*2*, *4*, *6*) reverse *I–V* characteristics of *n–p* GaN/SiC heterojunctions with the mesa-structure diameters of (*1*, *2*) 1500, (*3*, *4*) 200, and (*5*, *6*) 100 μm.

the forward voltage drop also depended on the diode area. In the range of low currents (10^{-9}–3×10^{-8} A), the current varied with voltage exponentially: $I = I_0 \exp(qV/nkT)$ (Fig. 4), with an ideality factor $n = 2.5$ (curve *1*) or 2 (curve *3*). A value of $n > 2$ is a characteristic indication of the existence of tunnel currents.
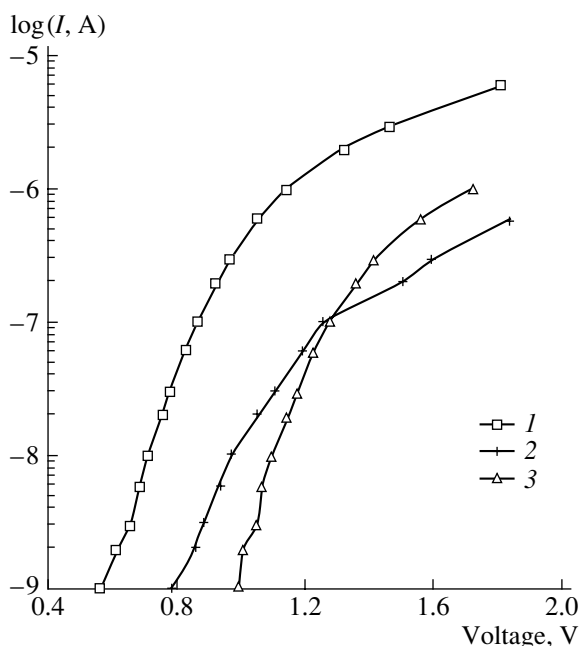
Fig. 4. Forward *I–V* characteristics of *n–p* GaN/SiC hetero-junctions with mesa-structure diameters of (*1*) 1500, (*2*) 200, and (*3*) 100 µm.

4. CONCLUSION

This study did not reveal any noticeable difference between the properties of GaN epitaxial layers grown on p^+-SiC substrates and p^+-SiC/n^+-SiC epitaxial structures. However, the *n*-type substrates are preferable because they have a lower density of structural defects and lower resistivity, compared with *p*-type substrates at the same doping level.

It has been shown previously that the morphology of GaN epitaxial layers strongly depends on the orientation of the SiC substrate and the conclusion that strictly oriented (planar) silicon carbide substrates should be used for growth of GaN/SiC heterojunctions has been advanced [13]. Therefore, the method of sublimation epitaxy in a vacuum, successfully used in this study to grow *p*-6*H*-SiC, seems to be promising because it enables epitaxy on planar 6*H*-SiC substrates, in contrast to the widely used CVD growth technique, which requires a substrate surface misorientation by 3°–4°.

The results of the electrical measurements performed in this study confirm the fairly high quality of the *n*-GaN/*p*-SiC heterostructures obtained. This observation indicates that the given combination of growth techniques is promising for fabrication of bipolar and FET transistors based on *n*-GaN/*p*-SiC heterojunctions.

REFERENCES

1. E. Danielsson, S.-K. Lee, C.-M. Zetterling, *et al.*, IEEE Trans. Electron. Devices **48**, 444 (2001).
2. N. I. Kuznetsov, A. E. Gubenco, A. E. Nikolaev, *et al.*, Mater. Sci. Eng. B **46**, 74 (1997).
3. J. T. Torvik, M. Leksono, J. I. Pankove, *et al.*, Appl. Phys. Lett. **72**, 1371 (1998).
4. J. T. Torvic, C.-H. Qiu, M. Leksono, and J. I. Pankove, Appl. Phys. Lett. **72**, 945 (1998).
5. J. Vacas, H. Lahre'che, T. Monteiro, *et al.*, Mater. Sci. Forum **338–342**, 1651 (2000).
6. E. Danielsson, C.-M. Zetterling, M. Ostling, *et al.*, Mater. Sci. Eng. B **61–62**, 320 (1999).
7. J. I. Pankove, S. S. Chang, H. C. Lee, *et al.*, in *Proceedings of IEDM* (San Francisco, CA, 1994), p. 389.
8. A. E. Nikolaev, Yu. V. Melnik, N. I. Kuznetsov, *et al.*, Mater. Res. Soc. Symp. Proc. **482**, 251 (1998).
9. N. S. Savkina, A. A. Lebedev, D. V. Davydov, *et al.*, Mater. Sci. Eng. B **61–62**, 50 (2000).
10. A. E. Nikolaev, Yu. V. Mel'nik, M. N. Blashenkov, *et al.*, MRS Internet J. Nitride Semicond. Res. **1**, 45 (1996).
11. W. Rieger, T. Metzger, H. Angerer, *et al.*, Appl. Phys. Lett. **68**, 970 (1996).
12. B. Monemar, J. P. Bergman, H. Amano, *et al.*, in *Proceedings of International Symposium on Blue Laser and Light-Emitting Diodes* (Chiba Univ., Japan, 1996).
13. M. Kamp, Opt. Quantum Electron. **32**, 227 (2000).

Translated by M. Tagirdzhanov

SEMICONDUCTOR STRUCTURES, INTERFACES, AND SURFACES

Photosensitivity of Photocells Based on ZnO/CdS/Cu(In, Ga)Se$_2$ Heterostructures and Exposed to γ-ray Radiation

V. V. Emtsev*, Yu. A. Nikolaev*, D. S. Poloskin*, V. Yu. Rud'**^, Yu. V. Rud'*, E. I. Terukov*, and M. V. Yakushev***

*Ioffe Physicotechnical Institute, Russian Academy of Sciences, Politekhnicheskaya ul. 26, St. Petersburg, 194021 Russia
**St. Petersburg State Polytechnical University, Politekhnicheskaya ul. 29, St. Petersburg, 195251 Russia
^e-mail: rudvas@spbstu.ru
***Strathclyde University, G 40 NG, Glasgow, UK
Submitted May 6, 2005; accepted for publication May 12, 2005

Abstract—The effect of irradiation with γ-ray photons (Co^{60}) on photoconversion in the thin-film ZnO/CdS/Cu(In, Ga)Se$_2$ heterostructure photocells exposed to natural and linearly polarized light is studied. It is shown that irradiation of the structures with penetrating γ-ray photons at room temperature affects the photoelectric parameters of thin-film heterostructure photocells only slightly, if at all, at γ-photon doses as high as $\Phi \approx 1.1 \times 10^{18}$ photon/cm^2. It is concluded that the ZnO/CdS/Cu(In, Ga)Se$_2$ heterostructure photocells can be used under the conditions of high-intensity γ-ray radiation. © 2005 Pleiades Publishing, Inc.

Inclusion of electronic analogues of the binary II–VI compounds (the ternary I–III–VI$_2$ ternary diamondlike semiconductors) into the research and development of thin-film photoconverters of solar radiation ensured rapid progress in this very important field. In fact, it is for the thin-film ZnO/CdS/Cu(In, Ga)Se$_2$ heterostructure photocells that the unprecedentedly high quantum efficiency (~19.2%) [1] for this type of photoconverters and an extraordinary high radiation resistance [2–5] were observed. The origin of this very high radiation resistance is not yet understood and is presumably related to annealing of radiation defects formed in Cu(In, Ga)Se$_2$ (CIGS) [2]. As a result, studies of the effect of irradiation with high-energy particles and penetrating photons on the physical properties of I–III–VI$_2$ semiconductors and solar cells based on these semiconductors have expanded rapidly in recent years. This study belongs to this important line of research and is concerned with investigation of the effect of irradiation with γ-ray photons on the photoelectric properties of the thin-film ZnO/CdS/CIGS structures in the cases of exposure to both natural and linearly polarized light.

The studied ZnO/CdS/CIGS thin-film solar cells with an area of ~0.5 mm^2 were grown at IPE (Stuttgart, Germany);[1] these structures are represented schematically in Fig. 1. In the initial (before irradiation) state, the ZnO/CdS/CIGS structures featured a photoconversion quantum efficiency $\eta^{in} \approx 13$–14% (at AM 1.5) and an open-circuit voltage $U^{in} \approx 620$ mV at $T = 300$ K. Irradiation with γ-ray photons was accomplished using a Co^{60} source with an intensity of ~3.2×10^{11} photon/(cm^2 s); during irradiation, the structures were kept under nor-

mal conditions at a temperature no higher than ~30°C. After irradiation of the structures for a given time, we measured the open-circuit photovoltage U^{ir} and the short-circuit current i^{ir}, the spectra of the relative quantum efficiency of the photoconversion $\eta^{ir}(\hbar\omega)$ under exposure to natural and linearly polarized light, and also the dependences of the coefficient of induced photopleochroism P_I on the angle of incidence θ and the energy $\hbar\omega$ of incident photons.

In Fig. 1, we show the typical dependences of the open-circuit photovoltage and the short-circuit photocurrent for a ZnO/CdS/CIGS solar cell on the flux den-
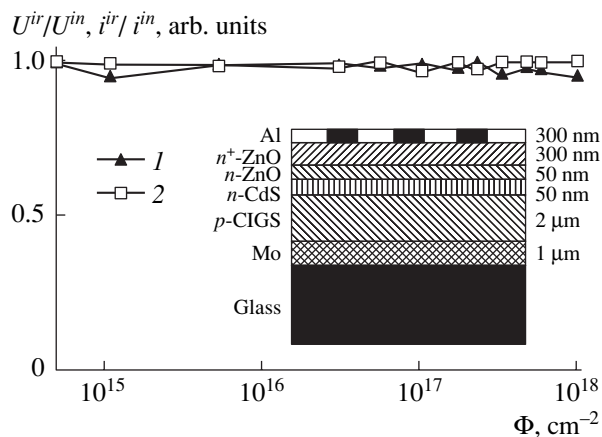

Fig. 1. Dependences of the (*1*) open-circuit photovoltage and (*2*) short-circuit photocurrent for a ZnO/CdS/CIGS heterophotocell on a dose of γ-ray radiation at $T = 300$ K. In the inset, we show the schematic representation of the ZnO/CdS/CIGS structure.

---

[1] We are indebted to Professor H.W. Schock for letting us have the ZnO/CdS/CIGS structures for our studies.

sity Φ of the γ-ray photons incident on this solar cell. It can be seen that the open-circuit photovoltage and the short-circuit photocurrent remain practically unchanged in a wide range of Φ as high as $\sim 1.1 \times 10^{18}$ photon/cm². This circumstance suggests that the thin-film hetero-structure ZnO/CdS/CIGS solar cells can be used under the conditions of high fluxes of γ-ray radiation, in which case irreversible changes in the physical proper-ties of the Si- and GaAs-based photoconverters, which are used widely in semiconductor electronics, occur under the effect of penetrating radiation; as a result, devices based on elemental and binary semiconductors fail [6–8].

The weak effect of irradiation with γ-ray photons on the properties of the ZnO/CdS/CIGS heterostructure photocells initiated detailed measurements of the spec-tra of the relative photoconversion quantum efficiency $\eta(\hbar\omega)$ in a wide range of fluxes of the incident γ-ray photons (Fig. 2). It can be seen that, up to the γ-photon fluxes of $\Phi = 1.1 \times 10^{18}$ photon/cm², not only does the spectral contour not experience any appreciable changes, it also retains its specific details. Indeed, irre-spective of the value of Φ, an increase in η sets in at $\hbar\omega > 0.5$ eV. This increase in the photosensitivity occurs comparatively slowly at photon energies up to $\hbar\omega \approx 1$ eV and can be correlated with the steepness $(\delta\hbar\omega) \approx 4$–5 eV⁻¹; the level of photosensitivity at $\hbar\omega < 1$ eV depends on the value of Φ only slightly. At $\hbar\omega > 1.04$ eV, a rapid exponential increase in the photosensi-tivity in the $\eta(\hbar\omega)$ spectra sets in; this increase can be correlated with a higher transconductance $S^* = 50$–80 eV⁻¹ (see table), which is characteristic of direct band-to-band transitions in the energy spectrum of the CuIn₀.₉Ga₀.₁Se₂ alloy. It can be seen from the table that the values of S^* depend in a complex manner on Φ, which can indicate that the γ-ray radiation affects the broadening of the edges of free bands by the electric fields of the charged defects that control the effect of transitions with the involvement of the tails in the den-sity of states.

The long-wavelength wing of the $\eta(\hbar\omega)$ spectra for the heterophotocells before and after irradiation is lin-earized in the representation $(\eta\hbar\omega)^2 = f(\hbar\omega)$ (Fig. 2), which corresponds to the direct band-to-band optical transitions in quaternary alloys. In accordance with the theory of interband absorption [9], the extrapolation $(\eta\hbar\omega)^2 \longrightarrow 0$ makes it possible to determine the band gap of the CIGS alloys used in the fabrication of the ZnO/CdS/CIGS heterophotocells; we found that $E_G = 1.12$ eV for CIGS at $T = 300$ K. It can be seen from the table that the value $E_G = 1.12$ eV (at $T = 300$ K) deter-mined from the spectra of photoactive absorption in the heterophotocells is found to be insensitive to the inte-grated flux Φ of γ-ray photons and is specified entirely by the alloy composition. Consequently, we can assume that γ-ray radiation does not induce decomposition of the alloy.
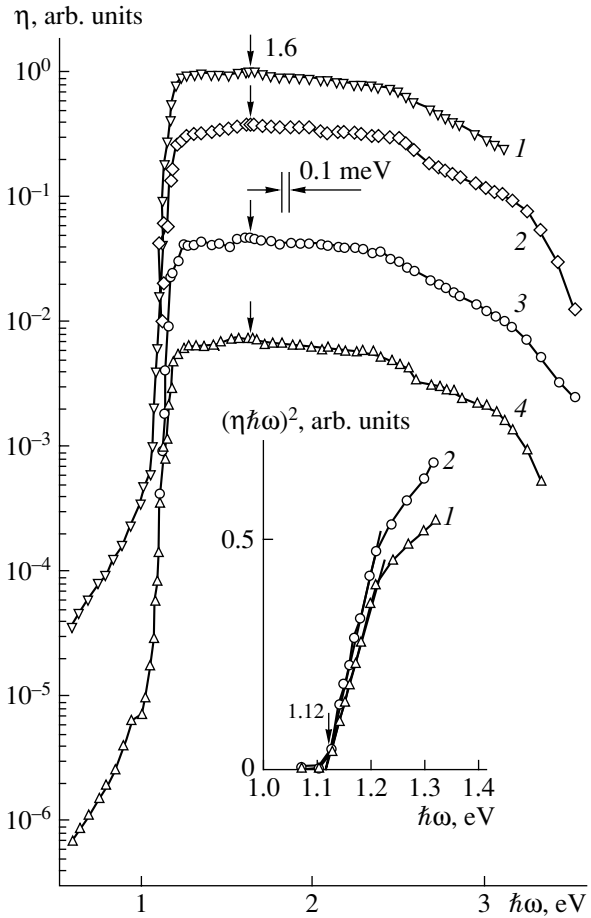
Fig. 2. The spectra of the relative quantum efficiency of photoconversion for a ZnO/CdS/CIGS heterophotocell in relation to a dose of irradiation with γ-ray photons (at $T = 300$ K) $\Phi = $ (*1*) 0, (*2*) 1.8×10^{17}, (*3*) 2.45×10^{17}, and (*4*) 1.1×10^{18} photon/cm². The $\eta(\hbar\omega)$ spectra are shifted along the vertical axis in order to avoid an overlap of the curves. The $(\eta\hbar\omega)^2 = f(\hbar\omega)$ dependences are shown in the inset. Desig-nations of the curves in the inset are the same as in the main panel.

It is clearly seen from the $\eta(\hbar\omega)$ spectra (Fig. 2) that the photosensitivity of the ZnO/CdS/CIGS heteropho-tocells remains high and does not depend on the inte-grated flux of γ-ray photons in a fairly wide range of optical-photon energies, from 1.2 to 2.2 eV. It also fol-lows from the photosensitivity spectra (Fig. 2) and the

Photoelectric properties of the ZnO/CdS/CIGS heterophoto-cells exposed to irradiation with γ-ray photons

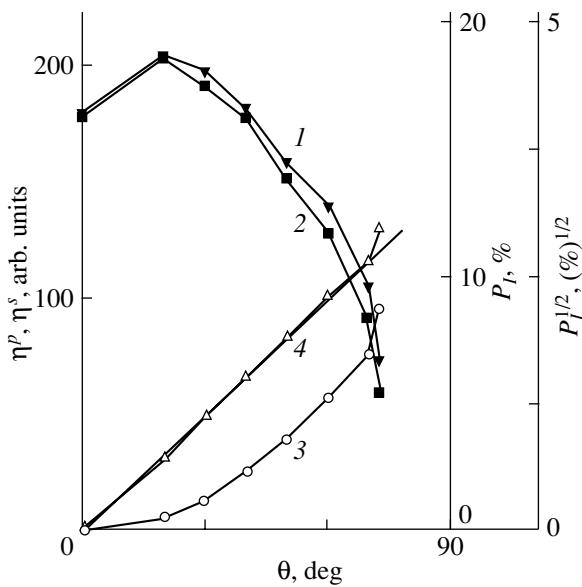| D, photon/cm²	$\hbar\omega^m$, eV	δ, eV	S^*, eV⁻¹	E_G, eV	P_I, % $(\theta = 70°)$
0	1.6	1.46	58	1.12	10
1.8×10^{17}	1.6	1.44	77	1.12	9
2.45×10^{17}	1.6	1.43	58	1.12	9
1.1×10^{18}	1.6	1.44	46	1.12	6

Fig. 3. Dependences of the photoconversion quantum efficiency (curve *1* is for η^P, curve *2* is for η^S) and the induced-photopleochroism coefficient (curve *3* is for P_I and curve *4* is for $(P_I)^{1/2}$) on the angle of incidence of linearly polarized light on the active ZnO surface of the ZnO/CdS/CIGS heterophotocell at $T = 300$ K and $\hbar\omega = 2.07$ eV.

Fig. 4. The spectra of induced photopleochroism for a ZnO/CdS/CIGS heterophotocell in relation to the integrated flux Φ of incident γ-ray photons (at $T = 300$ K) with $\Phi = $ (*1*) 0, (*2*) 2.45×10^{17}, and (*3*) 1.1×10^{18} photon/cm^2. Curve *4* represents the results of the calculation [13] at $\theta = 70°$.

table that the energy position of the absolute maximum in the photosensitivity $\hbar\omega^m = 1.6$ eV does not depend on the integrated flux of γ-ray photons. In addition, it is worth noting that the ratio between the value of the maximum photosensitivity within the CIGS fundamental-absorption band and the photosensitivity of heterophotocells in the region of absorption by point lattice defects was found to be very large, $(1–2) \times 10^4$; it is especially important that this ratio is virtually independent of the value of Φ, at least up to $\Phi = 1.1 \times 10^{18}$ photon/cm^2. This circumstance allows us to assume that, as a result of irradiation of the heterophotocells, the level of photoactive absorption in CIGS with the involvement of deep acceptor centers with the activation energy $E_a \approx 0.5–0.6$ eV and, correspondingly, that the concentration of these centers depends only slightly on the integrated flux of the γ-ray photons. We emphasize that this assumption is consistent with the experimental dependences of U^{ir} and i^{ir} on Φ (Fig. 1, curves *1*, *2*).

Inflection points at $\hbar\omega_1 = 2.5$ eV and $\hbar\omega_2 = 3.1$ eV can also be recognized in the short-wavelength portion of the $\eta(\hbar\omega)$ spectra for both the unirradiated samples (Fig. 2, curve *1*) and the ZnO/CdS/CIGS heterophotocells irradiated with γ-ray photons (Fig. 2, curves *2–4*); the energy positions of these points are consistent with the band gaps of the wide-gap CdS and ZnO films [10]. This circumstance gives grounds to relate the above spectral features to the interband absorption in the II–VI compounds under consideration. The values of the full width δ of the spectra at the half-maximum are also
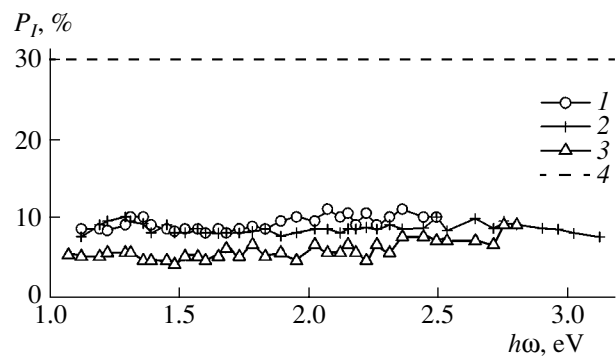
listed in the table; these values are fairly large and virtually do not depend on the γ-photon integrated flux used in our experiments. The fact that the large value of $\delta \approx 1.44$ eV in the studied heterophotocells is virtually insensitive to the γ-ray radiation suggests also that the quality of the interface in the heterophotocells under consideration is high.

If the ZnO/CdS/CIGS heterophotocells are exposed to a linearly polarized light in the entire range of photosensitivity, a maximum is observed in the dependences of the photoconversion quantum efficiency on the angle of incidence θ for the polarization such that the electric-field vector of the optical wave **E** is either parallel (η^p) or perpendicular (η^s) to the plane of incidence of the linearly polarized radiation; this maximum is located at $\theta \neq 0°$ for both polarizations (Fig. 3, curves *1*, *2*). According to [11–13], this specific feature makes it possible to conclude that a decrease in the losses for reflection is attained in a thin-film heterophotocell for light with the *s* and *p* polarizations as a result of the interference-related increase in transmission; as a consequence, a simultaneous increase in η^s and η^p occurs in the vicinity of the pseudo-Bruster angle (Fig. 3, curves *1*, *2*). As can be seen from Fig. 3 (curves *3*, *4*), the angular dependence of the induced-photopleochroism coefficient P_I follows the square law $P_I \propto \theta^2$ in the entire spectral range of photosensitivity of the ZnO/CdS/CIGS structure. In this case, as can be seen from Fig. 3, the experimental dependences of P_I on the optical-photon energy both before and after irradiation of the ZnO/CdS/CIGS structures with γ-ray photons (Fig. 4, curves *1–3*) run much lower than the calculated dependence $P_I(\hbar\omega)$ (Fig. 3, curve *4*). The observed decrease in P_I with respect to the calculated dependence $P_I(\hbar\omega)$ is indicative of the effect of the interference-related increase in transmission by the ZnO film in the entire range of photosensitivity of the ZnO/CdS/CIGS structures. According to [13], the criterion for the complete broadband increase in transmission is equivalent to the

condition $P_I \equiv 0$. Consequently, according to the results of studying the $P_I(\hbar\omega)$ spectra, it is necessary to develop a method for fabricating an antireflection film (so that the condition $P_I \equiv 0$ is satisfied) in order to increase further the photoconversion efficiency. In addition, an important conclusion following from Fig. 4 consists in the statement that not only does severe irradiation of the structures under consideration with the integrated γ-photon flux as high as $\Phi \approx 1.1 \times 10^{18}$ photon/cm^2 not sharpen the dependence $P_I(\hbar\omega)$, in contrast, it shifts the experimental spectrum $P_I(\hbar\omega)$ in the direction $P_I \longrightarrow 0$, which is consistent with dependences of the parameters U^{ir} and i^{ir} on Φ (Fig. 1).

Thus, we found that the photovoltage, short-circuit photocurrent, and induced-photopleochroism coefficient in the ZnO/CdS/CIGS heterophotocells virtually retain their values after irradiation with the integrated γ-photon fluxes as high as $\Phi \approx 1.1 \times 10^{18}$ photon/cm^2, which is indicative of the high radiation resistance of these photoconverters and illustrates their potential for use under conditions of hard penetrating radiation.

REFERENCES

1. O. Landberg, M. Edoff, and L. Stolt, in *Abstract Book: Solar World Congress ISES 2003* (Göteborg, Sweden, 2003), p. 57.

2. A. Jasenek, U. Rau, K. Weinert, *et al.*, Thin Solid Films **287**, 228 (2001).

3. A. Jasenek and U. Rau, J. Appl. Phys. **90**, 650 (2001).

4. K. S. Ramajah, V. S. Raju, A. K. Bhatnagur, *et al.*, Mater. Lett. **45**, 251 (2000).

5. T. Tanaka, T. Ohshima, S. Okada, *et al.*, J. Appl. Phys. **39**, 192 (2000).

6. V. S. Vavilov, N. P. Kekelidze, and L. S. Smirnov, *Effects of Radiation on Semiconductors* (Nauka, Moscow, 1988) [in Russian].

7. *Physical Processes in Irradiated Semiconductors*, Ed. by L. S. Smirnov (Nauka, Novosibirsk, 1977) [in Russian].

8. *Problems in Radiation Technology of Semiconductors*, Ed. by L. S. Smirnov (Nauka, Novosibirsk, 1980) [in Russian].

9. S. M. Sze, *Physics of Semiconductor Devices*, 2nd ed. (Wiley, New York, 1981; Mir, Moscow, 1984).

10. *Physicochemical Properties of Semiconductor Materials: Handbook*, Ed. by A. V. Novoselova (Nauka, Moscow, 1977) [in Russian].

11. V. Yu. Rud', Yu. V. Rud', T. Walter, and H. W. Shock, Inst. Phys. Conf. Ser., No. 152, 971 (1998).

12. V. Yu. Rud', Yu. V. Rud', and H. W. Shock, Solid State Phenom. **67–68**, 971 (1998).

13. F. P. Kesamanly, V. Yu. Rud', and Yu. V. Rud', Fiz. Tekh. Poluprovodn. (St. Petersburg) **33**, 513 (1999) [Semiconductors **33**, 483 (1999)].

Translated by A. Spitsyn

LOW-DIMENSIONAL SYSTEMS

The Tail of Localized States in the Band Gap of the Quantum Well in the In$_{0.2}$Ga$_{0.8}$N/GaN System and Its Effect on the Laser-Excited Photoluminescence Spectrum

M. A. Jacobson, D. K. Nelson, O. V. Konstantinov^, and A. V. Matveentsev

Ioffe Physicotechnical Institute, Russian Academy of Sciences, St. Petersburg, 194021 Russia
^e-mail: Samson@math.ioffe.rssi.ru
Submitted April 18, 2005; accepted for publication May 4, 2005

Abstract—It is established experimentally that the peak in the photoluminescence spectrum of the In$_{0.2}$Ga$_{0.8}$N/GaN heterostructure with a quantum well shifts by ~150 meV as the power density of a nitrogen laser used for excitation is increased from 10 to 1000 kW/cm^2. The large blue shift is interpreted as a manifestation of the tail of the density of localized states in the band gap of the quantum well. It is shown that, in the model of the ideal quantum well in which there is no tail of localized gap states, it is impossible to account for the large blue shift. A phenomenological expression is suggested for the density of states. The expression involves the adjustable parameter, namely, the Urbach energy that characterizes the tails of the density of localized states. By this means, both the long-wavelength edge of the luminescence spectrum and the large blue shift can be described. The quasi-Fermi level of photoelectrons depends on the pump intensity and is selected to fit each experimental curve. A qualitative agreement between the theoretical and experimental spectra is obtained, demonstrating that the model is adequate. From the condition for electrical neutrality, the surface carrier concentration is determined. It is found to be several orders of magnitude higher than the pyroelectric concentration in narrow quantum wells. © 2005 Pleiades Publishing, Inc.

1. INTRODUCTION

In this study, we observed a large blue shift (~150 meV) of the peak in the luminescence spectrum of the In$_{0.2}$Ga$_{0.8}$N/GaN heterostructure with a quantum well (QW) when the power density of the nitrogen laser used for excitation was changed from 10 kW/cm^2 to 1 MW/cm^2. This effect is similar to that first revealed in studying the luminescence of the structures with the In$_{0.2}$Ga$_{0.8}$N QWs between the GaN layers [1]. The large blue shift (LBS) was observed for one of the four samples described in [1] while, for the other three samples, the LBS effect was undetectable. Shapiro *et al.* [1] attributed this shift to the piezoelectric effect in the QW. Figure 1 shows a series of spectral curves obtained by us experimentally at the temperature $T = 80$ K for different excitation-power densities. We associate the LBS with two effects, namely, with the tail of the density of localized gap states in the QW and with the filling of the bands of the well with nonequilibrium charge carriers. The tail of the density of localized states is responsible not only for the LBS but also for the shape of the long-wavelength edge of the luminescence spectrum. In this study, we suggest a phenomenological expression to describe the tail of localized states by the Urbach energy (the parameter U). Figure 2 shows the experimental (dashed line) and theoretical spectra (solid lines) plotted for different values of the Urbach parameter. The lowest solid line refers to the theoretical spectrum obtained in the model of nearly ideal QW ($U = 5$ meV); in this spectrum, broadening of the long-wavelength edge is virtually absent. The specific feature of this curve is the sharp stepwise long-wavelength edge of spontaneous emission that corresponds to the stepwise edge of the density of states in the ideal QW near its bottom. According to the theory, the spectral peak of the spontaneous emission is "retained" against the step and there is no blue shift. With increasing U, at first, only a broadening of the long-wavelength edge is observed and the LBS is lacking. Such behavior was observed in studying photoluminescence (PL) of QWs in the GaN/Al$_x$Ga$_{1-x}$N structures in the case of high-power excitation [2]. In this system, the spectral peak shifted by less than 10 meV when the laser pump intensity was increased by three orders of magnitude. In such kinds of structures, the QW is formed of pure gallium nitride, and the tail of the localized states in the well is likely to be slightly pronounced. With an increase the Urbach parameter, the low-energy edge of the spectrum shifts farther and farther to the longer wavelengths. Fitting the results of calculation to our experimental data, we obtain the Urbach energy $U = 64$ meV. In this case, the shift is observable.

The high-energy slope (the right-hand side) of the spectral band should be seemingly dependent on the temperature-induced broadening of the distribution function of electrons and holes. In this case, however,
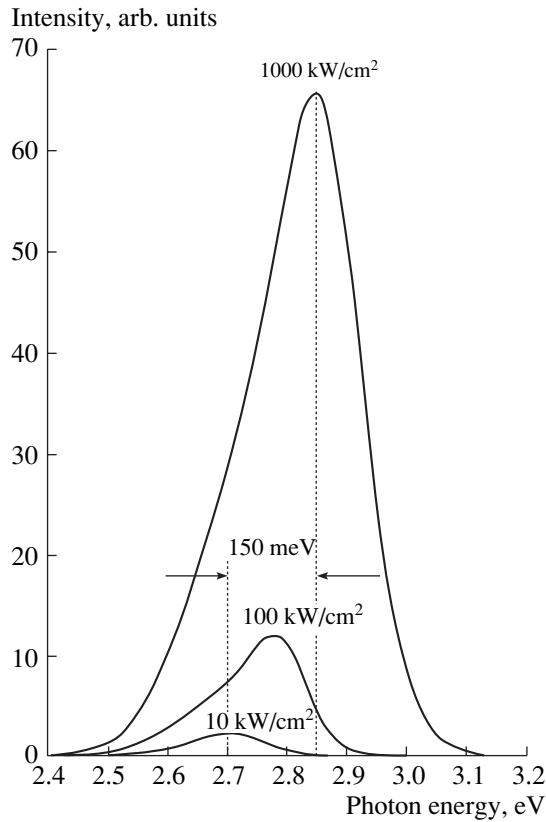
Fig. 1. Experimental photoluminescence spectra of the In$_{0.2}$Ga$_{0.8}$N/GaN heterostructure with a quantum well of width $d = 30$ Å at $T = 80$ K. The excitation power density of the nitrogen laser is indicated. The spacing between dashed vertical lines shows the spectral range corresponding to the large blue shift (150 meV).
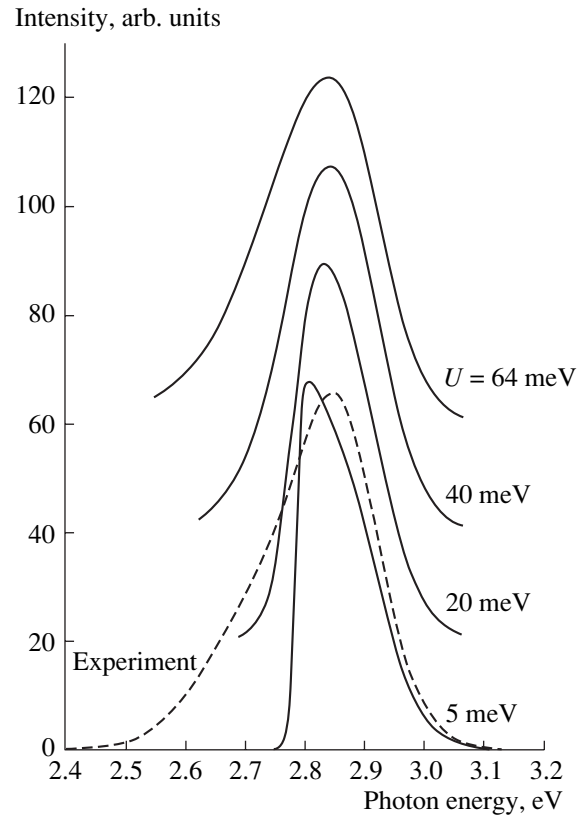

Fig. 2. Photoluminescence spectra of the quantum well obtained (dashed line) experimentally at the pumping power density 1 MW/cm^2 and (solid lines) theoretically with different values of the Urbach parameter U and with a 2.78 eV band gap of the material of the quantum well. Each succeeding curve corresponding to the larger parameter U is displaced with respect to the preceding curve for smaller U by the same upward shift (20 arb. units) along the vertical axis.

the broadening would be small, e.g., <10 meV at the liquid-nitrogen temperature. At the same time, analysis of the experimental data shows that the parameter of broadening of the right-hand slope is larger than the lattice temperature and is equal to 34 meV. In this context, it is interesting to give attention to the parameters of the luminescence line of the GaN "quasi-bulk" single crystal [3]. The room-temperature measurements showed that the full width at the half-maximum of the line was ~80 meV, and about the half-width is accounted for by the short-wavelength slope. Consequently, the "pseudotemperature" broadening is due to some inhomogeneous broadening also in this case. The lower part of the allowed band is likely to be formed by the levels of quantum dots that have a spread in energy and give rise to the pseudotemperature broadening. Figure 3 shows the theoretical spectral curves (solid lines) that are best fitted to the experimental spectral curves (dashed lines). Thus, the introduction of the Urbach parameter U and the pseudotemperature θ made it possible to interpret the two effects, the broadened edges of the spectrum and the LBS.

2. THE THEORY OF SPONTANEOUS EMISSION OF AN IDEAL QUANTUM WELL

For describing theoretically the spectrum of spontaneous emission due to recombination of carriers in a semiconductor QW, the well-known van Roosbroek–Shockley relation is commonly used in studies [4]. This relation is valid for nondegenerate electrons. On high-intensity laser excitation, the degeneracy of electrons is possible. Therefore, the methods of quantum electrodynamics should be used for deriving a correct formula. In quantum electrodynamics, the theory involves the Hamiltonian of a quantum electromagnetic field, the Hamiltonian of the system of electrons of the semiconductor, and the Hamiltonian of the interaction of electrons with the field. In the linear approximation, the Hamiltonian of the interaction is

$$\hat{V} = -\frac{e}{c}\mathbf{A}\hat{\mathbf{v}}. \tag{1}$$
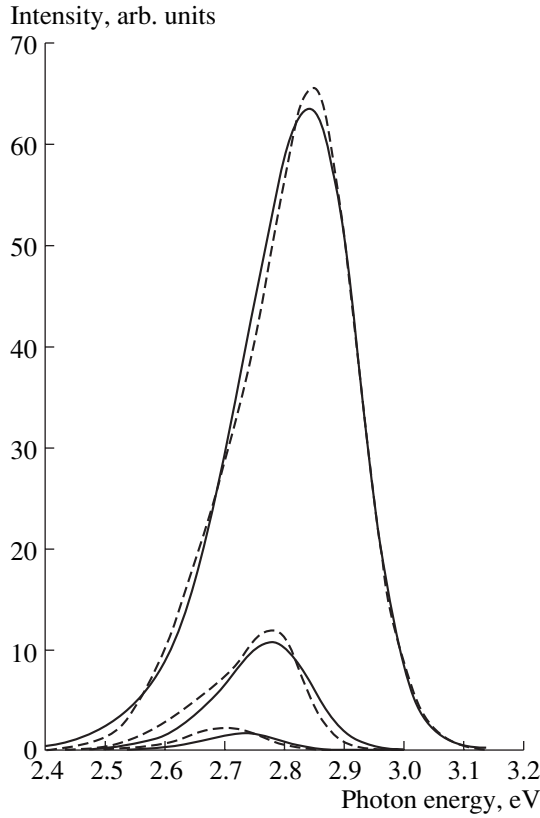
Intensity, arb. units

Fig. 3. Fitting of (solid lines) the theoretical spectra to (dashed lines) the experimental data. The adjustable parameters of the calculation are $U = 64$ meV and $\theta = 34$ meV.

Here, $\hat{\mathbf{v}}$ is the operator of the velocity of electrons and $\mathbf{A}$ is the operator of the quantized vector potential defined as [5]

$$\mathbf{A}(\mathbf{r}, t) = \frac{c}{\sqrt{V}} \sum_{q, \alpha} \sqrt{\frac{2\pi\hbar}{\omega_q}} e^{-i\mathbf{q} \cdot \mathbf{r}} \mathbf{e}_{q, \alpha} [a_{q, \alpha}(t) + a^+_{-q, \alpha}(t)], \quad (2)$$

where V is the volume of the system in which there is a photon of frequency $\omega_q = cq$ and $a_{q\alpha}(t) = a_{q\alpha} e^{-i\omega_q t}$ is the annihilation operator for a photon with the wave vector q and the polarization α. In formula (1), the term containing A^2 is discarded. Using the golden rule of quantum mechanics and (2), we can obtain the following expression for the probability ΔW_{if} of the emission of a photon with the energy $\varepsilon = \hbar\omega_q$ in the range $\Delta\varepsilon$ per second with simultaneous transition of the system of electrons from the state i to the state f:

$$\Delta W_{ij} = \frac{e^2}{\hbar c} \frac{1}{c^2} (\mathbf{e}_{q, \alpha} \mathbf{v})^2_{if} \frac{\Delta\Omega}{2\pi} \delta(E_i - E_f - \varepsilon) \omega_q \Delta\varepsilon. \quad (3)$$

This expression is valid in the dipole approximation. We use the matrix element of the velocity operator to obtain the conservation law for the electron quasi-wave vector k. The energies of an electron in the conduction band and in the valence band, $E_i \equiv E_C(k)$ and $E_f \equiv E_V(k)$, refer to the same value of the electron quasi-wave vector k, since the photon wave vector q can be disregarded. Integration with respect to q is not carried out, since we are concerned with the spectral function of emission of a photon with the specified q, ω_q, which is emitted in the specified direction within the solid angle $\Delta\Omega$. We now turn from the probability of emission of a photon per second, ΔW_{if}, to the rate of emission by a unit volume, $R(\varepsilon)$, in the unit range of photon energies and in the unit solid angle of photon escape [4]:

$$R(k) = \frac{\Delta W_{if}}{\Delta\varepsilon\Delta\Omega} \frac{1}{V}, \quad (4)$$

where V is the emitting volume of the structure. Formula (4) refers to the transition of a single electron with the specified momentum k from the conduction band to the valence band. To obtain the spectral density R integrated with respect to the momenta of all electrons, we must sum (4) over all values of k taking into account the functions of filling of the conduction band states and valence band states by electrons, $f_C(k)$ and $f_V(k)$:

$$R = \sum_k R(k) f_C(k)[1 - f_V(k)]. \quad (5)$$

Substituting the function $R(k)$ into (5) and taking into account (3) and (4), we obtain the spectral density of spontaneous emission integrated over all momenta as follows:

$$R = \frac{e^2}{\hbar c} \frac{\mathscr{A}_0}{\mathscr{A}} \sum_k f_k^{(e)} f_k^{(h)} \frac{|P_{CV}^{(x)}|^2}{m_0^2 c^2} \frac{\omega_q}{2\pi}$$
$$\times \delta(E_C(k) - E_V(k) - \varepsilon) \frac{1}{V}. \quad (6)$$

Here, $\mathscr{A}_0$ is the area of the unit cell in the QW, m_0 is the free-electron mass, and $\mathscr{A}$ is the total area of the QW. The Fermi functions of filling the quantum states with electrons, $f_k^{(e)} \equiv f_C(k)$, and holes, $f_k^{(h)} \equiv [1 - f_V(k)]$, are of the conventional form and involve different quasi-Fermi levels for the conduction and valence bands. Furthermore, $P_{CV}^{(x)}$ is the matrix element of the x component of the momentum operator defined by the following formula:

$$P_{CV}^{(x)} = \frac{-i\hbar}{V_0} \int_{V_0} U_C \frac{\partial}{\partial x} U_V dV. \quad (7)$$

The quantities U_C and U_V are the periodic amplitudes of the Bloch wave function, with the period of the unit cell in the QW. The volume of the unit cell is $V_0 = \mathscr{A}_0 d$, where d is the QW width. The total area of the QW can be used in integration, instead of summation, over all values of the two-dimensional wave vector. The integral along the length of this vector can be taken with the

use of the δ function of energy, if we assume that the dispersion relations in the conduction and valence bands are quadratic and isotropic:

$$E_C(k) = \frac{\hbar^2 k^2}{2m_C} + E_G, \quad E_V(k) = -\frac{\hbar^2 k^2}{2m_V}. \quad (8)$$

The energies are measured from the top of the valence band, and E_G is the band gap. Then the difference in energies is as follows:

$$E_C(k) - E_V(k) = \frac{\hbar^2 k^2}{2m} + E_G, \quad \frac{1}{m} = \frac{1}{m_C} + \frac{1}{m_V}, \quad (9)$$

where m_C and m_V are the effective masses of an electron and a hole, respectively, and m is the reduced mass. After integrating formula (6) with respect to the momentum and taking into account the energy-conservation law, we obtain the following expression for the integrated spectral density:

$$R = \frac{e^2}{\hbar c} \frac{\mathcal{A}_0 m}{\hbar^3} f^{(e)} f^{(h)} \frac{|P_{CV}^{(x)}|^2}{m_0^2 c^2} \frac{\varepsilon}{(2\pi)^2} \Theta(\varepsilon - E_G) \frac{1}{V}. \quad (10)$$

Here $\Theta(\varepsilon - E_G)$ is the unit step function that is equal to unity or zero if its argument is positive or negative, respectively.

The spectral shape of the luminescence line is defined by the factor

$$F(\varepsilon) = f^{(e)} f^{(h)} \varepsilon \Theta(\varepsilon - E_G) \quad (11)$$

that involves the filling functions $f^{(e)}$ and $f^{(h)}$. These functions depend on the photon energy via the arguments

$$\varepsilon_C = (\varepsilon - E_G)\frac{m}{m_C} \quad \text{and} \quad \varepsilon_V = (\varepsilon - E_G)\frac{m}{m_V}. \quad (12)$$

When (12) is substituted in the filling functions, these functions take the following form:

$$f^{(e)} = \frac{1}{e^{(\varepsilon_C - \mu_C)/\theta} + 1}, \quad f^{(h)} = \frac{1}{e^{(\varepsilon_V - \mu_V)/\theta} + 1}. \quad (13)$$

Here, μ_C and μ_V are the quasi-Fermi levels for electrons and holes and θ is the pseudotemperature measured in the units of energy. In the case of the two-dimensional gas in the QW, the quasi-Fermi levels can be calculated analytically. For electrons, we have

$$\mu_C = \theta \ln(e^{\nu_C} - 1), \quad \nu_C = \frac{\pi \hbar^2 N}{m_C \theta}. \quad (14)$$

Here, N is the density of electrons per unit surface area of the QW. An expression similar to (14) can easily be derived for holes. Expression (11) for the shape of the luminescence spectrum involves the stepwise Θ function that is equal to zero, if the photon energy is less than the band gap, or to unity in the opposite case. The abrupt change in intensity in the luminescence spec-

trum is representative of the stepwise change in the density of states in the QW. It should be emphasized that the step function is obtained as a theoretical result that was observed in none of the experimental luminescence spectra. It is assumed that this circumstance is caused by the existence of a tail of the density of local energy levels in the band gap of the QW. The local states are most probably due to random compositional fluctuations in the solid solution of the material of the well. The spectra calculated by formulas (11)–(14) are shown in Fig. 2.

3. THE THEORY ACCOUNTING FOR THE TAIL OF LOCALIZED STATES

In the case of crystalline solids with sharp edges of the band gap, the energies of electrons (ε_c) and holes (ε_V) in formulas (13) should be assumed to be positive. For disordered systems, these energies, if related to localized states in the band gap, are negative. In this case, no rigorous theory exists to derive the densities of localized states consistently, and therefore, some phenomenological expressions should be suggested for these functions [6]. For example, formula (11) can be generalized most simply using the following expression:

$$F(\varepsilon) = f^{(e)} f^{(h)} \varepsilon \frac{1}{e^{(E_G - \varepsilon)/U} + 1}, \quad (15)$$

where the step function $\Theta(\varepsilon - E_G)$ is replaced by the Fermi-type function, with the width of the Urbach tail U. The parameter U is the characteristic Urbach energy that is further considered as an adjustable parameter. The density of states (15) decreases exponentially into the depth of the band gap and tends to unity in the allowed band. Thus, the function (15) that defines the recombination emission spectrum of the QW with the density-of-states tails in the band gap takes the following form:

$$F(\varepsilon) = \frac{1}{e^{(\varepsilon_C - \mu_C)/\theta} + 1} \frac{1}{e^{(\varepsilon_V - \mu_V)/\theta} + 1} \frac{1}{e^{(E_G - \varepsilon)/U} + 1} \varepsilon. \quad (16)$$

The energies $\varepsilon_C = (\varepsilon - E_G)m/m_C$ and $\varepsilon_V = (\varepsilon - E_G)m/m_V$ expressed in terms of the photon energy ε should be substituted in formula (16). Then formula (16) can be written as

$$F(\varepsilon) = \varepsilon g((\varepsilon_C - \mu_C)/\theta)$$
$$\times g((\varepsilon_V - \mu_V)/\theta) g((E_G - \varepsilon)/U), \quad (17)$$
$$g(x) = \frac{1}{e^x + 1}.$$

In addition to formulas (16) and (17), a theory should be developed for determining the chemical potential of electrons and holes in the system involving the tails of the density of localized states. To accomplish this, it is necessary to introduce, along with the optical density of states $g((E_G - \varepsilon)/U)$, the densities of localized states in

Table

μ_C, eV	μ_V, eV	N, cm^{-2}	ε_{max}, eV		$\Delta\varepsilon_{max}$, meV	
			Theory	Experiment	Theory	Experiment
0.130	−0.169	1.09×10^{13}	2.84	2.85	110	150
0.047	−0.220	0.67×10^{13}	2.78	2.77	50	70
−0.016	−0.265	0.43×10^{13}	2.73	2.70	0	0

the conduction and valence bands separately. For this purpose, we use the following substitution:

$$g((E_G - \varepsilon)/U) \longrightarrow g(\varepsilon_C/U)g(\varepsilon_V/U). \qquad (18)$$

It can easily be checked numerically that the results of calculations by formula (17) with and without substitution (18) are virtually the same.

We can now derive the general formula that relates the quasi-Fermi level to the surface concentration N of carriers (e.g., electrons) if there is a tail of localized states. We extend expressions (14) to the case of localized states with the energies $\varepsilon_C < 0$. Then, the quasi-Fermi level is involved in the filling function $f(\varepsilon_C)$ in the expression for N as follows:

$$N = \frac{N_C}{\theta} \int_{-\infty}^{\infty} g(\varepsilon_C/U) f(\varepsilon_C) d\varepsilon_C, \qquad (19)$$

where N_C is the density of states defined according to (14). We now discuss the approximate integration in (19). The integrand in (19) has a maximum at a certain value of the integration variable, namely, at

$$\varepsilon_{Cmax} = \mu_C \frac{U}{U + \theta}. \qquad (20)$$

When the integration variable is smaller than ε_{Cmax}, the integrand can be assumed to be equal to $g(\varepsilon_C)$, and when the variable is larger than ε_{Cmax}, the integrand is equal to $f(\varepsilon_C)$. Thus, we obtain the approximate expression for the integral in (19) as follows:

$$N = N_C \frac{U + \theta}{\theta} \ln\left[1 + \exp\left(\frac{\mu_C}{U + \theta}\right)\right]. \qquad (21)$$

This formula can be used for both electrons and holes (in the latter case, N_C should be replaced with N_V). The chemical potential of electrons is a parameter to be varied for obtaining the best fit of the theoretical spectrum to the experimental data. In this case, formula (21) is used for determining the chemical potential of holes

that is found to be negative for all of the curves. The peak of the spectrum of spontaneous emission is close to the maximum (20) of the integrand in (19), although the peak is shifted to the left-hand side due to the effect of holes. The increase in the spectral function and the shift of its peak are almost entirely due to the changes in the electron distribution function with increasing the chemical potential of electrons. For illustration, we present a table that lists the chemical potentials of electrons, μ_C, and holes, μ_V; the carrier concentrations in the bands, N; the peak positions in the spectrum, ε_{max}; and the LBSs, $\Delta\varepsilon_{max}$, corresponding to the theoretical curves in Fig. 3. The values given in the table were obtained using the following values of the adjustable parameters: $E_G = 2.78$ eV, $U = 0.064$ eV, and $\theta = 0.034$ eV. In the calculations, the effective masses of electrons and holes were $m_C = 0.17m_0$ and $m_V = 1.64m_0$ [7].

We now comment on the above-mentioned condition for equality of the densities of electrons and holes. The point is that the material of the QW is pyroelectric [8]. The condition for electrical neutrality should also involve the pyroelectric charges whose surface density may well be ~10^{13} cm^{-2}. In the case of narrow wells (with a width no larger than 40 Å), however, the surface density of the pyroelectric charges dramatically decreases to the value of ~10^{10} cm^{-2} as the width decreases. Therefore, the pyroelectric charges can be disregarded for narrow wells [8].

REFERENCES

1. N. A. Shapiro, P. Perlin, C. Kisieloowski, *et al.*, MRS Internet J. Nitride Semicond. Res. **5**, 1 (2000).

2. M. A. Jacobson, D. K. Nelson, N. Grandjean, *et al.*, Phys. Status Solidi C **0**, 487 (2002).

3. K. Motoki, T. Okahisa, N. Matsumoto, *et al.*, Jpn. J. Appl. Phys. **40**, L140 (2001).

4. J. I. Pankove, *Optical Processes in Semiconductors* (Prentice-Hall, Englewood Cliffs, N.J., 1971; Mir, Moscow, 1973).

5. A. S. Davydov, *Quantum Mechanics*, 2nd ed. (Nauka, Moscow, 1973; Pergamon, Oxford, 1976).

6. N. F. Mott and E. A. Davis, *Electronic Processes in Non-Crystalline Materials* (Clarendon, Oxford, 1971; Nauka, Moscow, 1974).

7. R. J. Radtke, U. Waghmare, H. Ehrenreich, and G. H. Grein, Appl. Phys. Lett. **73**, 2087 (1998).

8. O. Ambacher, J. Majewski, C. Miskys, *et al.*, J. Phys.: Condens. Matter **14**, 3399 (2002).

Translated by É. Smorgonskaya

PHYSICS OF SEMICONDUCTOR DEVICES

Continuous-wave Lasing of Single-Mode Metamorphic Quantum Dot Lasers for the 1.5-μm Spectral Region

L. Ya. Karachinsky[1, 2^], T. Kettler[2], N. Yu. Gordeev[1], I. I. Novikov[1], M. V. Maximov[1], Yu. M. Shernyakov[1], N. V. Kryzhanovskaya[1], A. E. Zhukov[1], E. S. Semenova[1], A. P. Vasil'ev[1], V. M. Ustinov[1], N. N. Ledentsov[1, 2, 3], A. R. Kovsh[1, 3], V. A. Shchukin[1, 2, 3], S. S. Mikhrin[1, 3], A. Lochmann[2], O. Schulz[2], L. Reissmann[2], and D. Bimberg[2]

[1]*Ioffe Physicotechnical Institute, Russian Academy of Sciences, St. Petersburg, 194021 Russia*
^*e-mail: Karach@switch.ioffe.ru*
[2]*Institut für Festkörperphysik, Technische Universität, D-10623 Berlin, Deutschland*
[3]*NL-Nanosemiconductor GmbH, 44227 Dortmund, Deutschland*
Submitted March 28, 2005; accepted for publication April 12, 2005

Abstract—Lasers based on InAs/InGaAs quantum dots grown on metamorphic (In,Ga,Al)As layers deposited by MBE on GaAs substrates exhibited emission near 1.5 μm with a differential quantum efficiency of about 50%. The narrow-stripe lasers operate in a single transverse mode and withstand continuous current density above 20 kA cm^{-2} without significant degradation. A maximum continuous-wave output power of 220 mW is obtained. Neither current nor beam filamentation was observed up to the highest pumping levels. © *2005 Pleiades Publishing, Inc.*

1. INTRODUCTION

In the past few years, considerable progress has been made in the development of quantum dot (QD) semiconductor lasers [1]. QD lasers have exhibited the previously predicted, ultra-low threshold current density [2], high temperature stability [3] and differential efficiency [4], small α parameter and, consequently, suppressed filamentation of the field [5], and a reduced shift of the lasing wavelength with variation in the pump current. Special attention has been given to the long-wavelength QD lasers on GaAs substrates [6], which can be used in optical communication systems. High-quality 1.3 μm stripe lasers and vertical-cavity surface-emitting lasers (VCSELs) have been developed [1, 7]. This progress has stimulated interest in QD lasers that are formed on the GaAs substrates and emit at longer wavelengths, up to 1.5 μm.

Until recently, only the InP–InGaAsP system of materials had been used in the development of 1.3–1.55 μm semiconductor lasers. However, some fundamental problems limit the potentialities of these devices. Insufficient electron confinement in the active region [8, 9] results in poor temperature stability of the threshold current and emission wavelength. Another serious problem limiting the areas of application of quantum well (QW) lasers based on InP is the small difference between the refractive indices of GaInAs and AlInAs. Due to this factor, the reflectance of the distributed Bragg reflector necessary for the operation of a vertical laser (>0.99) can be attained only in structures containing no less than 50 pairs of layers. Thus, the develop-ment of integrated VCSELs based on this system of materials is problematic.

Two different approaches in the development of 1.5 μm semiconductor lasers are used nowadays. The first is based on the use of GaInAsN–GaAsN [10] or GaInNAsSb–GaNAsSb [11] QWs in the active region. Lasing at 1.42 μm with the total output optical power in the CW mode $P_{CW} = 17$ mW (cavity length $L = 600$ μm, stripe width $W = 4$ μm) was reported in [10]. In the GaInNAsSb–GaNAsSb system, the lasing wavelength was 1.498 μm, with $P_{CW} = 140$ mW, $L = 2500$ μm, and $W = 20$ μm [11].

Recently, we suggested another approach based on the concept of metamorphic growth of InGaAlAs buffer layers on GaAs substrates [12, 13]. Earlier, metamorphic growing was used for the formation of QW [14, 15] and QD [16] lasers on silicon substrates. However, the CW output power of these lasers was low and the lasers soon degraded.

To localize the misfit dislocations in the bottom buffer layer and attain a low density of dislocations in the upper layers, we have derived a special defect-reduction technique [17]. Wide-stripe injection lasers with ten InAs–InGaAs QD layers in the active region lased at 1.48–1.52 μm, with a threshold current density about 1–1.5 kA cm^{-2}, and an external differential quantum efficiency of 52%. The total optical emission power from a 100-μm-wide stripe under pulsed pumping exceeded 7 W [17, 18]. However, operation of these lasers in the CW pumping mode has not yet been observed or studied.
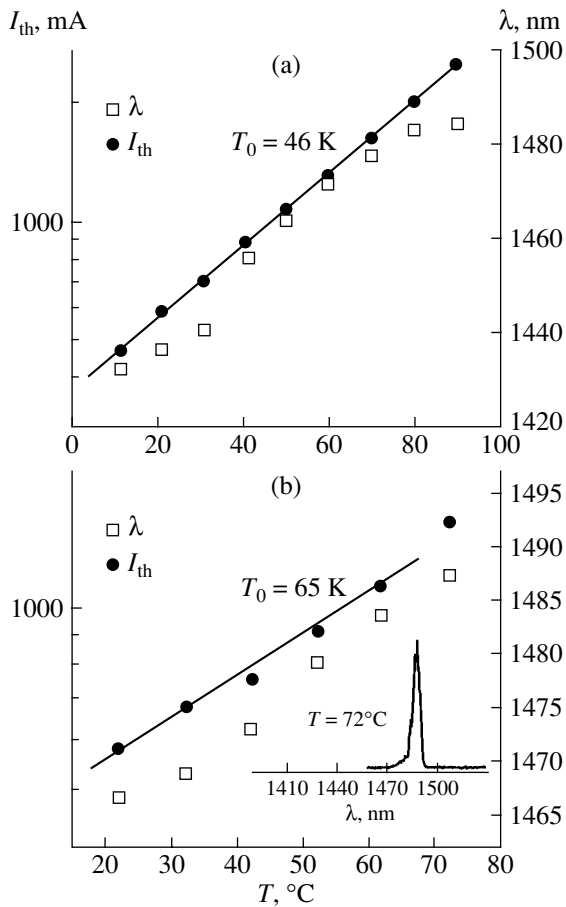
Fig. 1. Temperature dependences of the threshold current and lasing wavelength, recorded under pulsed excitation for samples of structures (a) no. 1 and (b) no. 2. The inset in Fig. 1b shows the electroluminescence (EL) spectrum of structure no. 2 at 72°C and pump current $I = 1.1I_{th}$. $L = 2$ mm; W: (a) 6, (b) 7 μm.

The goal of this study was the design of 1.5 μm single-mode CW lasers on GaAs substrates. We present a detailed analysis of the temperature, power, spatial, and spectral characteristics of metamorphic lasers with InAs QDs.

2. EXPERIMENTAL

Metamorphic laser heterostructures no. 1 and no. 2 were MBE-grown on (100) n^+-GaAs substrates. Ten layers of InAs QDs formed in the Stranski–Krastanov mode were placed in the center of an $In_xGa_{1-x}As$ ($x \approx 21\%$) waveguide of 0.8 μm in thickness. Each QD layer was overgrown with a thin $In_yGa_{1-y}As$ ($y \approx 41\%$) layer. The emitters were InAlGaAs layers (In ≈ 21%). Two versions of the metamorphic buffer were used in this study. In structure no. 1, it consisted of an InGaAs layer 1 μm thick followed by an InAlGaAs (Al ≈ 30%) n-type emitter 1.5 μm in thickness. In structure no. 2, an InGaAs–InAlGaAs superlattice 1.5 μm thick with an average Al content of ≈15% served as the metamorphic buffer and the n-type emitter simultaneously.

Stripe lasers with a stripe width of 6, 7, and 8 μm were fabricated from the grown heterostructures. Ni/AuGe/Au and Ti/Pt/Au contacts were deposited onto the n- and p-doped sides, respectively. Lasers of different cavity lengths were fabricated. The samples were soldered onto a copper heat sink with the p-type side down for better heat removal. No coating was deposited onto the cavity mirrors. The lasers were studied in a wide range of temperatures in CW and pulsed modes (pulse width $\tau = 200$ ns, repetition frequency $f = 1$ kHz).

In the study of the near-field pattern, the facet of a laser diode was projected with a microscope objective onto a CCD camera. A Ge photodiode was used as a detector in the spectral, power, and far-field pattern measurements.

3. RESULTS AND DISCUSSION

At first, the lasers were studied in the pulsed mode. For samples with a cavity length of 1.4 mm, the threshold current I_{th} was in the range of 380–420 mA at a temperature of 20°C for all three stripe widths: $W = 6, 7,$ and 8 μm. Figures 1a and 1b show the temperature dependences of the threshold current and lasing wavelength for structures no. 1 and no. 2, respectively. The characteristic temperature T_0 was 46 K for structure no. 1 and 65 K for no. 2. The longest lasing wavelength was observed for structure no. 2 at 72°C (see the inset in Fig. 1b). Figures 2a and 2b show emission–current characteristics for structures no. 1 and no. 2, respectively. The maximum total output optical power obtained from heterostructure no. 1 was 800 mW and 440 mW from no. 2. The highest differential quantum efficiency for the studied samples with a cavity length of 1.4–2 mm was 35% and 50% for heterostructures nos. 1 and 2, respectively.

Figure 3 shows distributions of the emission intensity across the facet of a sample of heterostructure no. 2 with a stripe 6 μm wide at different pump currents. The laser was placed on a micropositioning device, which made it possible to calculate the image scale by shifting the laser with respect to the microscope objective lens and camera. As can be seen in Fig. 3, the near-field emission profile remains virtually unchanged as the pump current increases. This observation indicates that increasing the pump current does not lead to excitation of new optical modes and filamentation. Samples with a stripe width of 7 and 8 μm exhibited similar behavior. The obtained results confirm previous data [5] on the considerable suppression of filamentation in QD semiconductor lasers.

The inset in Fig. 3 shows far-field emission in the lateral and vertical directions for a sample of heterostructure no. 2 with a stripe 6 μm wide at a pump current of $2.4I_{th}$. The FWHM of the lateral field lies in the
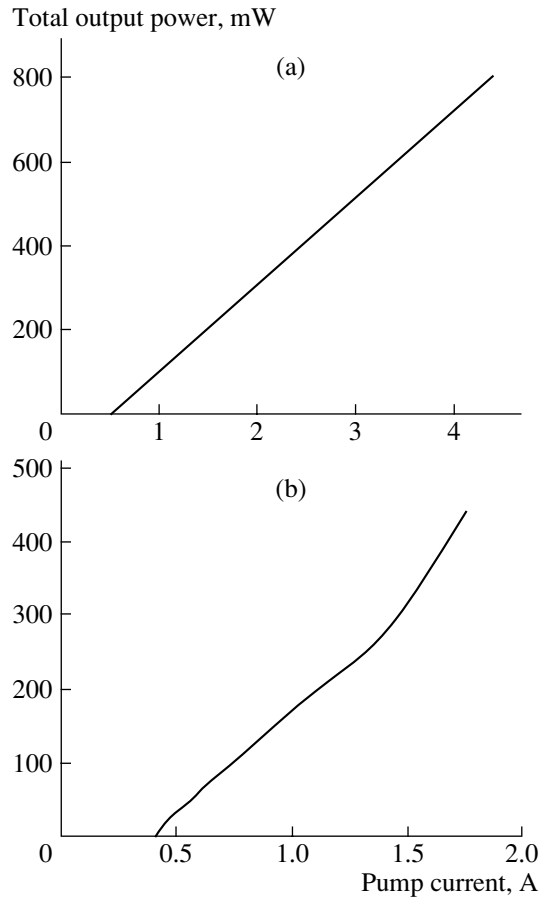
Total output power, mW

Fig. 2. Emission–current characteristics of structures (a) no. 1 and (b) no. 2. Pulsed excitation, $T = 20°C$. (a): $W = 6$ μm, $L = 2$ mm, $I_{th} = 500$ mA; (b): $W = 7$ μm, $L = 1.4$ mm, $I_{th} = 390$ mA.

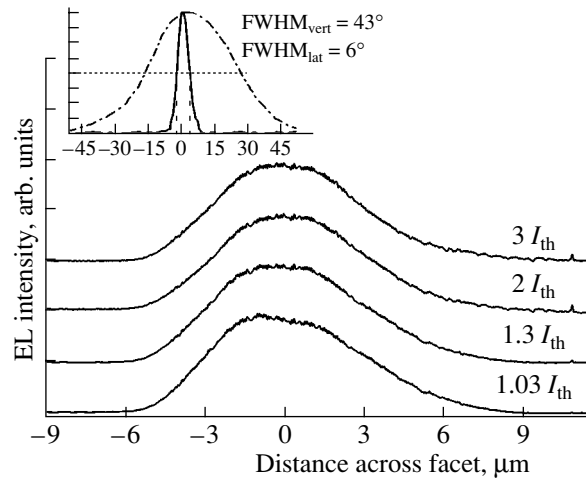**Fig. 3.** Distributions of the emission intensity across the facet of a sample of structure no. 2 with a stripe width $W = 6$ μm for different pump currents. $T = 20°C$. Inset: far-field emission in the lateral and vertical planes at a pump current of $2.4I_{th}$. $L = 1.4$ mm.

range 5.6°–7.1° at a pump current $I = (1.25–2.4)I_{th}$. The far-field emission profile is Gaussian, which was observed also for lasers with a stripe width of 7 and 8 μm. In the vertical direction, the far-field distribution did not change as the pump current was varied; the beam divergence was 43°, which agrees fairly well with the data calculated for the given configuration of the waveguide. Therefore, we conclude that the long-wavelength QD lasers under study lase in the fundamental optical mode. Similar results were obtained also for heterostructure no. 1, where the FWHM of the far-field emission was 6°–8° in the lateral direction and 40°–42° in the vertical direction.

Figure 4 shows the room-temperature lasing spectra of heterostructure no. 2, obtained under pulsed excitation at different pump currents. As can be seen, the emission wavelength at the lasing threshold is 1448.6 nm. As the pump current increases, emission emerges also in the long-wavelength range, with the main peak at about 1460.5 nm. Similar behavior of the emission spectra as a function of the pump current was observed for heterostructure no. 1. To determine whether two spectral

peaks belong to the same transverse lasing mode or to different modes, we have studied the spectrally resolved lateral far-field pattern of structure no. 2 at a pump current of $1.8I_{th}$. The monochromator was tuned to different peaks of the emission spectrum, $λ_1 = 1448.6$ nm or $λ_2 = 1460.5$ nm. This experimental method was suggested in [19]. It appeared that the distribution profiles for both spectral peaks coincide (see the inset in Fig. 4) and correspond to the same transverse mode. We believe that the transition of lasing from short to longer wavelengths at a pump current of about $(1.25–1.5)I_{th}$ is caused by heating of the active region; this inference is confirmed by the data of spectral studies in the CW mode, which are presented below. We intend to perform further studies to consider this problem in more detail.

Figures 5a and 5b show the emission–current and current–voltage characteristics of lasers based on heterostructure no. 1 ($W = 6$ μm, $L = 2$ mm) and no. 2 ($W = 7$ μm, $L = 2$ mm), respectively, recorded in the CW mode at 10°C. As can be seen from Figs. 5a and 5b, in both structures the optical output power increases with the pump current, and both curves exhibit features (the so-called kinks). As some specific value of the pump current (1.5 A for heterostructure no. 1 and 1 A for no. 2) is exceeded, a reversible decrease in the optical output power is observed, which is related to heating of the active region. The maximum optical output power was 220 mW for heterostructure no. 1 and 70 mW for no. 2. The differential quantum efficiency was 38.4% for heterostructure no. 1 and 22% for no. 2. As can be seen in Fig. 5a, the metamorphic lasers under study withstand the CW mode operation without noticeable degradation at a pump current of about 2.6 A ($\sim$22 kA cm^{-2}.)

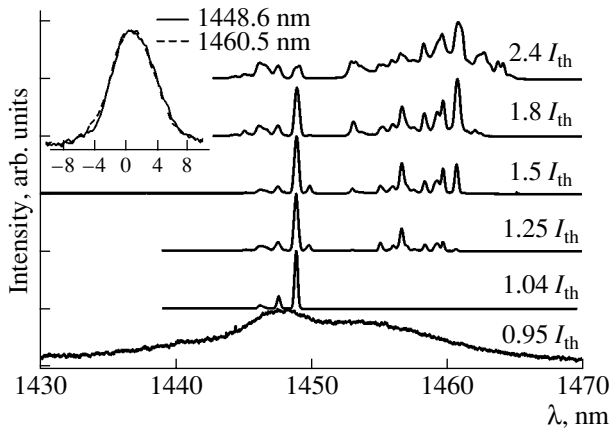**Fig. 4.** Spectra of emission from structure no. 2, recorded under pulse excitation at different pump currents and $T = 20°C$. Inset: lateral far-field emission recorded with spectral resolution at a pump current of $1.8I_{th}$. $W = 8$ μm, $L = 1.4$ mm.
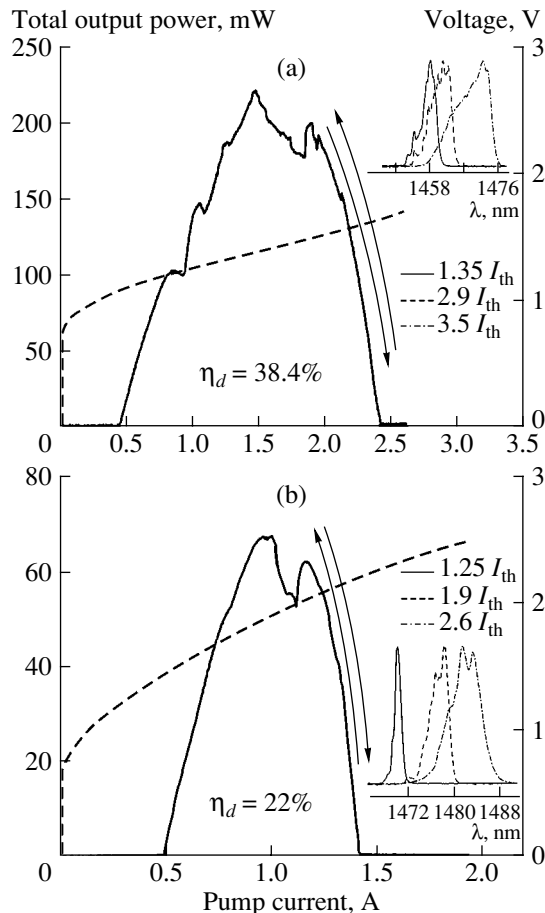

Fig. 5. Emission–current (solid lines) and current–voltage (dashed lines) characteristics of laser emission from structures (a) no. 1 and (b) no. 2. CW mode, $T = 10°C$. Insets: the CW-mode emission spectra. (a): $W = 6$ μm, $L = 2$ mm, $I_{th} = 430$ mA; (b): $W = 7$ μm, $L = 2$ mm, $I_{th} = 480$ mA.

The insets in Figs. 5a and 5b show the corresponding emission spectra for heterostructures no. 1 and no. 2. Kinks in the emission–current characteristics can be related to transitions between different groups of longitudinal spectral modes [20]. The red shift of the lasing wavelength with an increase in the pump current is related to heating of the active region. The amount of this heating can be estimated using the data presented in Figs. 1a and 1b. The position of the emission peak in the CW mode is compared with the position of the peak under pulsed pumping at different temperatures. Our estimates show that for both structures the maximum heating amounts to about 60°C.

4. CONCLUSION

We studied metamorphic lasers with InAs–InGaAs QDs, MBE-grown on GaAs substrates and emitting at about 1.5 μm. Lasers with a stripe width of 6–8 μm exhibit single-mode operation with a high differential quantum efficiency, up to 50%. The maximum optical power was 220 mW in the CW mode and 800 mW in the pulsed mode. In this type of lasers, the CW mode and spatially single-mode operation are observed for the first time. The obtained CW output power is an order of magnitude higher than that reported previously for lasers that operated in this spectral region and were based on nitrogen-containing QWs. The absence of filamentation is observed up to high excitation levels. The obtained results allow us to assert that semiconductor heterostructures with metamorphic InAs–InGaAs QDs are a highly promising material for the fabrication of stripe lasers and VCSELs intended for the 1.3–1.5 μm spectral range and formed on GaAs substrates or on other substrates lattice mismatched and/or having different thermal expansion coefficients.

REFERENCES

1. N. N. Ledentsov, IEEE J. Sel. Top. Quantum Electron. **8**, 1015 (2002).

2. G. Park, O. B. Shchekin, D. L. Huffaker, and D. G. Deppe, IEEE Photonics Technol. Lett. **12**, 230 (2000).

3. O. B. Shchekin, J. Ahn, and D. G. Deppe, Electron. Lett. **38**, 712 (2002).

4. A. R. Kovsh, N. A. Maleev, A. E. Zhukov, *et al.*, Electron. Lett. **38**, 1104 (2002).

5. Ch. Ribbat, R. L. Sellin, I. Kaiander, *et al.*, Appl. Phys. Lett. **82**, 952 (2003).

6. D. G. Deppe, D. L. Huffaker, S. Csutak, *et al.*, IEEE J. Quantum Electron. **35**, 1238 (1999).

7. D. Bimberg, N. N. Ledentsov, and J. A. Lott, MRS Bull. **27**, 531 (2002).

8. M. Yano, H. Imai, and M. Tukusagawa, J. Appl. Phys. **52**, 3172 (1981).

9. H. Ishikawa and I. Suemune, IEEE Photonics Technol. Lett. **6**, 344 (1994).

10. D. Gollub, S. Moses, M. Fischer, and A. Forchel, Electron. Lett. **39**, 777 (2003).

11. S. R. Bank, M. A. Wistey, L. L. Goddard, *et al.*, IEEE J. Quantum Electron. **40**, 656 (2004).

12. A. E. Zhukov, A. R. Kovsh, S. S. Mikhrin, *et al.*, Fiz. Tekh. Poluprovodn. (St. Petersburg) **37**, 1143 (2003) [Semiconductors **37**, 1119 (2003)].

13. N. N. Ledentsov, A. R. Kovsh, A. E. Zhukov, *et al.*, Electron. Lett. **39**, 1126 (2003).

14. J. P. van der Ziel and N. Chand, J. Appl. Phys. **68**, 2731 (1990).

15. M. E. Groenert, Ch. W. Leitz, A. J. Pitera, *et al.*, J. Appl. Phys. **93**, 362 (2003).

16. K. K. Linder, J. Phillips, O. Qasaimeh, *et al.*, Appl. Phys. Lett. **74**, 1355 (1999).

17. N. N. Ledentsov, A. R. Kovsh, V. A. Shchukin, *et al.*, Proc. SPIE **5624**, 335 (2005).

18. M. V. Maksimov, Yu. M. Shernyakov, N. V. Kryzhanovskaya, *et al.*, Fiz. Tekh. Poluprovodn. (St. Petersburg) **38**, 763 (2004) [Semiconductors **38**, 732 (2004)].

19. N. Yu. Gordeev, A. M. Georgievski, V. I. Kopchatov, *et al.*, in *Proceedings of International Symposium on Nanostructures: Physics and Technology* (St. Petersburg, Russia, 1997), p. 183.

20. D. Ouyang, R. Heitz, N. N. Ledentsov, *et al.*, Appl. Phys. Lett. **81**, 1546 (2002).

Translated by D. Mashovets

PHYSICS OF SEMICONDUCTOR DEVICES

The Limiting Energy Resolution of SiC Detectors in Ion Spectrometry

N. B. Strokan*, A. M. Ivanov*^, A. A. Lebedev*, M. Syväjärvi**, and R. Yakimova**

*Ioffe Physicotechnical Institute, Russian Academy of Sciences, St. Petersburg, 194021 Russia
^e-mail: alexandr.ivanov@mail.ioffe.ru
**Linköping University, S-581 33 Linköping, Sweden
Submitted April 12, 2005; accepted for publication April 25, 2005

Abstract—The Monte Carlo method is used to simulate the complete stopping of α particles in SiC. A histogram of energy losses in nuclear-scattering events is obtained. The energy-loss spectrum has the characteristic asymmetric shape with the line full width at the half-maximum $FWHM_{nucl} \approx 4.22$ keV. The final shape of the spectral line is obtained by a convolution with the Gaussian function that describes the contribution of the ionization and noise fluctuations (originated in the detector and instrumentation) to the signal. The resulting value of FWHM for the line is equal to 8.75 keV (at a noise variance of 1.7 keV). The experimental energy resolution of the detectors was found to be poorer than the calculated value by a factor of 2. It is established that the losses of charge during its transport in the detector bulk are insignificant, so that the discrepancy between the calculated and experimental values of the resolution should be attributed to the nonoptimal design of the detector window. © 2005 Pleiades Publishing, Inc.

1. INTRODUCTION

Appreciable progress has been made recently in the growth of single-crystal high-purity SiC films using the method of chemical reactions in the gaseous phase [1, 2]. The films have a concentration of uncompensated donor impurities on the level of 10^{14}–10^{15} cm^{-3} and a thickness of 30–50 μm. These parameters make it possible to use the layers with good results as nuclear-radiation detectors. Detectors based on SiC are very promising due to the wide band gap of the material, the high electrical and mechanical strength, the chemical stability, and the high threshold energy for the formation of structural defects. The latter circumstance ensures the radiation resistance of the SIC structures.

Successful fabrication of SiC detectors was started in the late 1990s. At that time, the characteristics of the detectors were not good enough to ensure a sufficient extent of the depletion region in the detector. The transport of the nonequilibrium charge carriers generated by radiation occurred in diffusion–drift conditions and was accompanied by a noticeable capture of the carriers [3]. It is worth noting that a good point consisted in the fact that the conditions of the capture of diffusing charge carriers were almost the same for the entire area of the detector according to the data reported elsewhere [4]. Detectors that had a transistor structure and were formed on 10-μm-thick *p*-type 6*H*-SiC films were studied. The amplitude of the signal in the detectors of this type is proportional to the squared diffusion length of electrons and, in combination with a fairly high energy resolution (~10%), indicated that this parameter was uniformly distributed throughout the detector bulk. It is

significant that the value of the energy resolution was established starting with the voltage at which the depletion region was ~3-μm thick, in which case diffusion was a fosteriori prevalent in the charge-carrier transport.

A similar conclusion could be drawn also for the "thick" (30 μm) films with a difference concentration of impurities smaller than 4.5×10^{16} cm^{-3} [5]. Detectors with a standard diode structure made it possible to resolve all four lines of the α decay from the ^{226}Ra preparation, notwithstanding substantial losses of the charge carriers in the course of the diffusive transport. The results mentioned above made it possible to expect the attainment of a high energy resolution under the condition of exclusion of a "slow" diffusion and realization of a "rapid" drift of charge carriers.

A high energy resolution of the detectors based on next-generation SiC films has been reported in recent publications. For example, the energy resolution attained for short-range nuclear particles (by the example of α particles with an energy of ~5.5 MeV) was equal to 0.5% [6] and ≲0.35% [7]. For the X-ray radiation in the energy region of ≤60 keV, the resolution obtained was equal to ~300 eV, which corresponded to the relative resolution of 0.5% at the upper boundary of the range [8]. The results mentioned rank below those for silicon detectors developed technologically to the highest extent only by a factor of 2; the energy resolution of these silicon-based detectors corresponds virtually to the theoretical limit.

In this paper, we consider two related issues. We estimate the ultimately attainable energy resolution of the detectors that use silicon carbide as the detecting

medium. We then analyze the possible factors that bring the energy resolution below the theoretically allowable values.

2. BASIC FACTORS LIMITING THE ENERGY RESOLUTION

Semiconductor spectrometry is based on the "ionization" principle of radiation detection. The charge generated in an operating medium as a result of stopping of a nuclear particle (or absorption of a photon) is taken as a measure of the energy of the corresponding particle. In the general case, fluctuations of the basic and twofold origin accompany the transformation of energy into equivalent charge. First, the ambiguity of the energy losses of a particle manifests itself in the events of elastic scattering by the atoms of the operating medium (in the case under consideration, by the Si and C atoms). This dissipated energy is spent unproductively from the standpoint of generation of the electron–hole pairs. Second, the yield of the nonequilibrium charge directly in the cascades of impact ionization fluctuates as well. The practically unavoidable noise in the detector and detection electronics contributes also to broadening of the spectral line. It is worth noting that the factor of nuclear scattering is absent in the cases of spectrometry of X- and γ-ray radiation.

A more detailed consideration of stopping α particles in SiC yields the following pattern. The transformation of the particle energy into the charge of electron–hole pairs is a result of a complex branched sequence of events. According to the information stated above, primary collisions of the incident particle with both the atomic electrons (ionization) and the silicon and carbon nuclei (scattering) occur. In turn, the δ electrons formed as a result of ionization give rise to cascades of impact-ionization events. The primary displaced atoms form the secondary recoil atoms, which create the tertiary displaced atoms, and so on. Simultaneously, the primary displaced atoms and secondary recoil atoms are also involved in ionization; consequently, a fraction of the energy lost as a result of nuclear scattering of the particle is spent on an increase in ionization. An analytical description of the statistics of the generated charge is very difficult if the general pattern of the events is considered. Therefore, the energy losses of the particle in the events of nuclear scattering and ionization are here considered separately and within certain approximations.

2.1. Nuclear Scattering

Let us consider the manifestation of nuclear scattering in the case of spectrometry of α particles with an energy of 5.4 MeV. This energy is close to that of the decay of a number of isotopes, in particular, of uranium, plutonium, and americium. In the case of silicon-based detectors, it is the energy losses in the events of

elastic scattering by Si atoms that make the major contribution to the width and shape of the spectral line [9].

An analysis carried out in the fundamental original study [10] showed that a monochromatic line undergoes the following changes if the nuclear scattering is taken into account. First, the line shifts to lower energies by the value of the average losses as a result of scattering (~10 keV). Second, the monoline acquires an asymmetric shape and is conditionally represented as a Gaussian peak with an extended tail on the low-energy side. The variance of the peak is given by

$$\sigma_{nucl} = 0.2 A^{4/3} Z^{1/2}, \qquad (1)$$

where A and Z are the atomic mass and charge of the particle, respectively. For α particles, the value of the resulting line width at the half-maximum (FWHM) is expressed as

$$FWHM_{nucl} = 2.35\sigma_{nucl} = 4.22 \text{ keV}.$$

An analytical description of the distribution-tail shape is lacking in the available publications.

It is significant that the variance depends only on the properties of the scattered particle. However, the direct use of the data obtained previously on scattering of α particles in silicon detectors [9] appears to be incorrect for the binary SiC detectors. Indeed, according to formula (1), the presence of carbon atoms gives rise to the energy-loss spectrum with the variance similar to that in the silicon detectors. However, the difference between the masses of carbon and silicon and also between the corresponding scattering cross sections should result in a difference in the energy position of the spectra. In what follows, we report the results of simulation of complete stopping of α particles in SiC using the Monte Carlo method (the TRIM code [11]).

In order to simplify the calculation, we restrict ourselves to consideration of only the energy acquired by atoms in primary collisions. This approach is based on the results obtained in [12] where the second-order collisions and the corresponding ionization were taken into account. However, the result obtained did not differ from the value $FWHM_{nucl} = 4.22$ keV. In what follows, we use a value of 5 eV a fortiori too small for the displacement-threshold energy for the Si and C atoms. This approach makes it possible to take into account collisions with a small transfer of energy. The obtained histogram is shown in Fig. 1.

We now clarify qualitatively the process of formation of the histogram in Fig. 1. As the α particles are slowed down, major energy losses occur in the multiple events of excitation of electron shells. The number of the elastic-scattering events is on the order of 100. The differential cross section of scattering with transfer of the energy in the range from T to $T + dT$ to the atom is described by the following well-known formula:

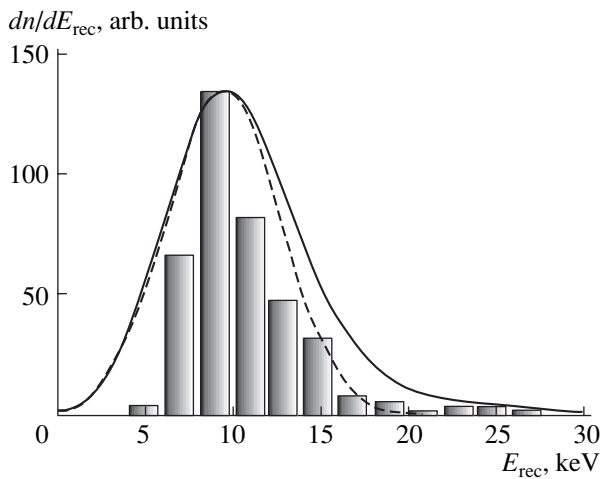$$d\Omega/dT = (E_\alpha T^2)^{-1}. \qquad (2)$$

Fig. 1. Distribution of the energy transferred to the primary recoil atoms during stopping of the 5.4-MeV α particles (histogram) and the convolution of this distribution with the Gaussian function (the solid line) whose variance involves fluctuations in the ionization efficiency and noise (5). The dashed line represents the Gaussian function that features the common left-hand side with the results of the convolution. The full width of the line at the half-maximum is equal to 8.75 and 7.60 keV for the spectra described by the convolution and Gaussian function, respectively.

Fig. 2. Dependence of the total energy E_{rec} transferred to the Si and C atoms by an α particle on the path length traversed by the particle. The calculation was carried out for the final stage of stopping ($E_\alpha = 2.0$ MeV). The main fraction of the energy is transferred at the end of the path in which case the α-particle energy drops to hundreds of keV.

Fig. 3. The spectrum of the energy T transferred to the Si and C atoms for a randomly chosen 5.4-MeV α particle.

Here, E_α is the α-particle energy. The range of energies T is fairly wide since the maximum value of the transferred energy in the head-on collision is $T_{max} = 0.44E_\alpha$ and $0.75E_\alpha$ for scattering by the Si and C atoms, respectively. Thus, in the beginning of the stopping process for an α particle, the energy transferred to silicon atoms can be as high as ~2.4 MeV and the maximum energy transferred to carbon atoms is ~4.0 MeV. However, it follows from formula (2) that collisions with transfer of small portions of the energy are most probable. These collisions occur at the end of the α-particle path where most of the energy is already lost in inelastic collisions.

In Fig. 2, we show the calculated dependence of the total energy transferred to the Si and C atoms on the distance along the α-particle track; the dependence was averaged over 1000 particles. The calculation was carried out for the final portion of the stopping process, in which the α-particle energy decreased to 2 MeV and the range was $d = 5.0\,\mu$m. It is significant that the resulting value $E_{rec} = 9.2$ keV is close to the value of the most probable E_{rec} in the histogram shown in Fig. 1 and obtained for the case of $E_\alpha = 5.4$ MeV under consideration. It can also be seen that a sharp increase in E_{rec} is observed starting with $d \approx 4.0\,\mu$m, where the α-particle energy is found to be lower than 300 keV. This circumstance narrows to a great extent the range of energies T transferred to atoms in individual collisions. However, the poor statistics of the transfer events brings about a significant variance not only in the shape of the transferred-energy spectra $dn/dT = f(T)$ for individual particles (Fig. 3) but also in the total spectrum energy. It is these quantities that form the histogram shown in Fig. 1.
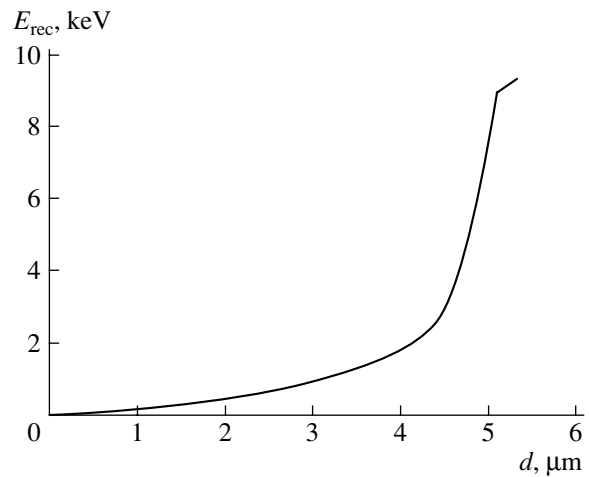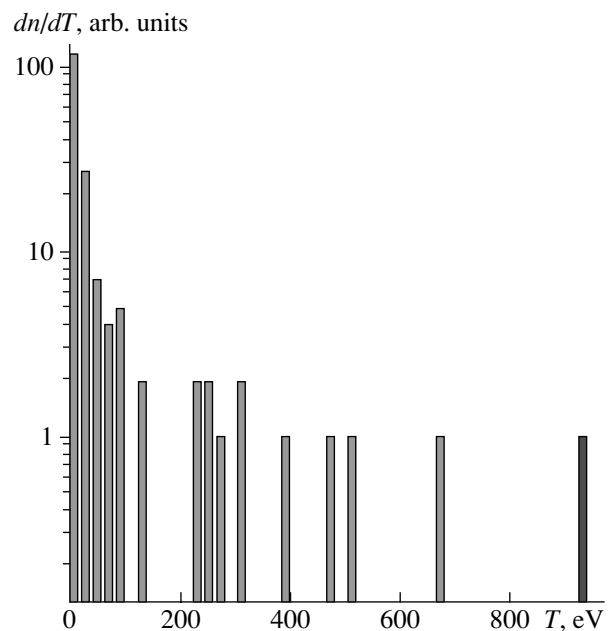
In the region of small deviations from the most probable (mean) value, the histogram shown in Fig. 1 is almost symmetric. As follows from an analysis of the spectra $dn/dT = f(T)$, this region can be attributed to the particles that are not involved in collisions with the transfer of large energies T.

The large values of E_{rec} that contribute to the right-hand side of the histogram are related to the fact that the events with transferred energies T of several keV appear

in the chain of collisions. The events with T equal to tens of keV are characteristic of the beginning and middle of the α-particle path; however, the probability of these events decreases as $(E_\alpha)^{-1}$. For the cases of $E_{rec} \geq$ 30 keV, we took into account approximately the ionization produced by the recoil atoms. The Si atoms with energies of tens of keV spend ~60% of their energy on ionization. Correspondingly, the values $E_{rec} \gtrsim 30$ keV were multiplied by 0.4 and only after that were included in the histogram. In order to obtain the resulting shape of the spectral line (the solid line in Fig. 1), we carried out the convolution of the histogram with the spectra of the ionization fluctuations and noise. To make clear the asymmetry of the spectral line, we plotted the Gaussian function that had the left-hand side in common with the result of the convolution (dashed line in Fig. 1).

2.2. Fluctuations of the Ionization Efficiency

Fluctuations of the ionization efficiency are related to the fact that the δ electrons generated directly by an α particle and the hot charge carriers generated later by these electrons spend their energy not only on ionization but also on the excitation of the lattice vibrations. The presence of two mechanisms (channels) brings about a statistical redistribution of the energy between these channels. In addition, the energy is spent by different portions (from event to event) within the channels themselves.

Fluctuations of the above origin were considered for the first time in the case of gases [13]. It was established that the variance of the number of generated electron–ion pairs (N) is not described by the Poisson law; rather, it is described by a more contracted distribution

$$\overline{(N - N_0)^2} = FN_0, \tag{3}$$

where N_0 is the mean number of the pairs and $F < 1$ is the Fano factor. This limitation of fluctuations is a consequence of the condition implicitly present: a particle should lose a strictly fixed energy. The values of the Fano factor are equal to $F = 0.1$–0.2 for the semiconductor materials used in nuclear detectors. The distribution of the number of electron–hole pairs can be described using the Gaussian function with the line width

$$FWHM_{ion} = 2.35(F\varepsilon_0 E_\alpha)^{1/2}, \tag{4}$$

where ε_0 is the average energy needed for formation of an electron–hole pair.

The value of F is unknown for SiC. Assuming that $F = 0.1$ and using the value $\varepsilon_0 = 7.70$ eV [7, 8], we find that $FWHM_{ion} = 4.8$ keV in the case under consideration. This value (taking into account the use of the value of F on the left-hand boundary of the range) exceeds the energy fluctuations in the case of nuclear scattering.

The noise spectrum is also described by a Gaussian distribution; therefore, the combined manifestation of the ionization fluctuations and noise is expressed by the Gaussian law with the variance

$$\sigma_\Sigma = (\sigma_{ion}^2 + \sigma_{noise}^2)^{1/2}. \tag{5}$$

After performing the convolution of the aforementioned spectrum with the data of the histogram in Fig. 1, we obtain the spread function for the line shape (see Fig. 1, solid line). In calculations, we assumed that $\sigma_{noise} = 1.7$ keV for noise. It can be seen that, within the assumptions used above, the resulting line width is 8.75 keV. This value virtually coincides with the calculated ultimate energy resolution of silicon detectors.

3. COMPARISON WITH EXPERIMENTAL DATA

In the case of silicon, the ultimate energy-resolution level was attained in practice [9]. Consequently, the factors involving the semiconductor nature of both silicon itself and the detector structure do not play an important role in the limitation of the energy resolution.

The energy resolution of SiC-based detectors, whose technology is less advanced, is two times lower than the calculated value. This discrepancy is caused most probably by losses of the nonequilibrium charge in the course of its transport in the active region of the detector and also by nonoptimal design of the detector window.

3.1. Losses of Charge in the Bulk of the Detector Structure

Losses of charge in the course of transport can occur owing to either recombination of electron–hole pairs or localization of one of the pair components at the capture centers. The factor determining the resulting spread in the signal amplitudes (the energy resolution of the detector) consists in the difference in the conditions of the transport of charge-carrier packets for different tracks; this difference is unavoidable for actual single crystals. We emphasize that it is the inhomogeneities that are important since the volumes of the tracks diffusing to electrodes are insignificant. For example, the track volume is ~5×10^{-9} cm^3 for α particles even if the transverse diffusive spread is taken into account.

In SiC detectors fabricated using next-generation SiC films, a leveling off of the signal amplitude is clearly observed as the bias voltage (U) increases. This circumstance indicates that the charge transport occurs in full measure and the charge losses do not exceed the accuracy of measurements. This accuracy is very high, so that the losses that are not accounted for can amount to tenths of a percent.

The factor related to inhomogeneity can be estimated from the dependence of the detector's energy resolution on the charge loss $\lambda = (q_0 - q)/q_0$. Here, q_0
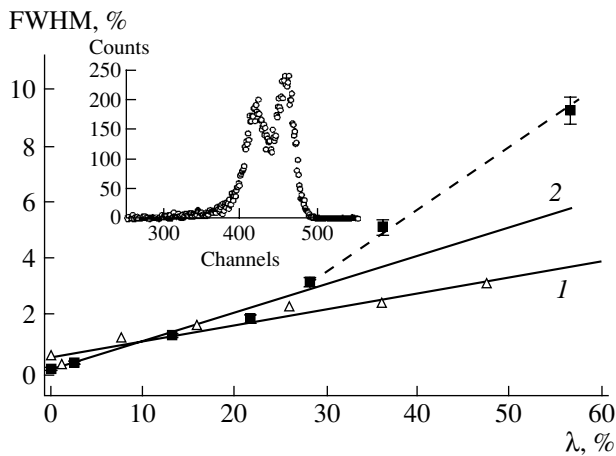
FWHM, %

Fig. 4. Dependences of the detector energy resolution on the value of the charge losses. These are due to the operation in the mode of incomplete charge transport as a result of the involvement of diffusion. The slope of the dependences is related to the nonuniformity of the conditions of the charge-carrier transport for the tracks of individual α particles. Curves *1* and *2* represent the data for a homogeneous sample and a sample that has the spectrum in the form of a doublet at low bias voltages (see inset).

and q are the charge generated by the particle and that detected. In order to include the losses λ, the voltage applied to the detector U is lowered to transfer the detector to the mode where the field-region thickness becomes smaller than the α-particle range and diffusion is involved in the charge transport. According to [14], the dependence of the charge losses on the spectrum width referred to the mean amplitude is linear:

$$\text{FWHM} = \kappa\lambda. \qquad (6)$$

The value of the coefficient κ serves as a measure of the charge-loss nonuniformity. It was reported [14] that $\kappa = 0.36$ in the case of a conventional surface-barrier silicon nuclear detector.

In Fig. 4, we show the dependences (6) for two types of SiC detectors. Dependence *1* corresponds to a detector whose spectrum is described by a single line in the entire range of voltages (including the zero voltage). The spectrum of the second sample consisted of a doublet at the bias voltages ≤ 35 V (see the inset in Fig. 4). Consequently, the conditions of the charge transport were evidently different for different areas of the sample. As a whole, the sample should be considered as two detectors that are connected in parallel and feature different charge losses λ. Correspondingly, the function $\text{FWHM} = f(\lambda)$ features a kink at the value of losses (the voltages U) that gives rise to the doublet.

It is significant that the obtained values of the parameter $\kappa = 0.06$–0.10 are appreciably smaller than those reported previously [14] for silicon. As a result, after estimating the adverse effect of the charge capture on the energy resolution with formula (6), we obtain

$\text{FWHM} \approx 0.01\%$; thus, the value of FWHM is insignificant compared with the fundamental limitation of $\sim 0.2\%$.

3.2. *The Role of the Detector Window*

As shown above, one fails to account for the discrepancy between the calculated values of the energy resolution and the experimental data by the charge capture in the detector bulk. Therefore, this discrepancy should be attributed to the nonoptimal design of the detector window. A similar problem was solved when Si-based detectors started to be used in high-resolution spectrometry [15]. The disadvantages of the Schottky barriers have been revealed, and the necessity for obtaining an ultrashallow p^+–n junction by diffusion was established. Using the concept of a built-in field (see, for example, [16]), it became possible to obtain an effective window thickness as small as 300 Å (for silicon equivalent).

In the SiC detectors designed for the α-particle spectrometry, a structure with the Schottky barrier formed by deposition of 0.1-μm-thick chromium film was used. Direct energy losses in this film amount to 34 keV (0.6%). Since the film is considered as thin, fluctuations of this quantity are appreciable. An estimation using the Bohr model (see monograph [18]) yields the value $\text{FWHM}_{\text{win}} \geq 10$ keV for the conditions of normal incidence of α particles on the surface. Methodically, this circumstance means that the source becomes nonmonochromatic. It is worth noting that the parallelism of the α-particle beam was not controlled in the measurements of the energy resolution in [17]; therefore, the energy fluctuations were more significant after α particles traversed the window.

The charge losses due to the surface-recombination mechanism constitute another deleterious factor when the Schottky barrier is used. Specific features of dense tracks formed by α particles manifest themselves here. As a result of the high density of nonequilibrium charge carriers, the track is in the state of shielded plasma for a certain interval of time. Electrons and holes in the track are not separated by an electric field; rather, they diffuse to the semiconductor–metal interface and recombine via surface states. A high local nonuniformity of the recombination rate is characteristic of a real surface; as a result, significant fluctuations in the charge losses should also be expected.

It is worth noting that the role of the interface was also studied for silicon surface-barrier detectors. In particular, the charge transport in ultradense tracks of the fission fragments and accelerated heavy ions was studied [19, 20]. The origin of the observed charge deficit was related by the authors predominantly to the state of the detector surface.

4. CONCLUSION

We used the Monte Carlo method to simulate the spectrum of energies transferred to the Si and C atoms ("the operating medium") in the course of elastic scat-

tering of α particles. The spectrum features a characteristic asymmetry due to the right-hand side of the spectrum related to the transfer of significant portions of energy to the atoms. The characteristics of the spectrum are close to those in the case of a silicon detector, although the presence of carbon atoms could introduce distortions. The energy absorbed by a Si atom differs from that absorbed by a C atom as a result of the differences between the atomic masses and scattering cross sections.

Fluctuations in the ionization efficiency (at the same values of the Fano factor) are larger in the case of SiC as a result of the higher average energy required for generation of an electron–hole pair. The general Gaussian shape of the spectrum of both the ionization fluctuations and the noise unavoidable experimentally makes it possible to sum the squares of their variances. This circumstance compensates for a larger contribution of the ionization channel by the smaller noise figure of the SiC detectors (much lower generation currents). The calculated resulting width of the spectral line was found to be equal to 8.75 keV.

As for the factors of the semiconductor origin, the attained level of the quality of the film bulk ensures the collection of charge to within fractions of a percent. In addition, charge transport occurs in the situation where the conditions over the detector area are almost identical. The experimental values of the energy resolution are larger than the calculated values by a factor of 2; this discrepancy should be related to the inadequately developed technology of the SiC detector as a whole. In order to improve further the energy resolution of the SiC detector, it is necessary first of all to refine the technology of the detector window.

In general, we can conclude that, as a result of using next-generation SiC films, this semiconductor has joined the group of the main semiconductor materials suitable for high-resolution spectrometry of nuclear radiation.

ACKNOWLEDGMENTS

REFERENCES

1. R. Yakimova, M. Syväjärvi, R. R. Ciechonski, and Q. Wahab, Mater. Sci. Forum **457–460**, 201 (2004).

2. CREE Research, Durham, NC 27713, USA.

3. F. Nava, P. Vanni, C. Lanzieri, and C. Canali, Nucl. Instrum. Methods Phys. Res. A **437**, 354 (1999).

4. A. A. Lebedev, N. B. Strokan, A. M. Ivanov, *et al.*, Appl. Phys. Lett. **79**, 4447 (2001).

5. N. B. Strokan, A. M. Ivanov, N. S. Savkina, *et al.*, J. Appl. Phys. **93**, 5714 (2003).

6. A. M. Ivanov, E. V. Kalinina, A. O. Konstantinov, *et al.*, Pis'ma Zh. Tekh. Fiz. **30**, 1 (2004) [Tech. Phys. Lett. **30**, 575 (2004)].

7. N. B. Strokan, A. M. Ivanov, E. V. Kalinina, *et al.*, Fiz. Tekh. Poluprovodn. (St. Petersburg) **39**, 382 (2005) [Semiconductors **39**, 364 (2005)].

8. G. Bertuccio, S. Binetti, S. Caccia, *et al.*, Mater. Sci. Forum **483–485**, 1015 (2005).

9. I. N. Il'yashenko and N. B. Strokan, Pis'ma Zh. Tekh. Fiz. **22**, 1 (1996) [Tech. Phys. Lett. **22**, 599 (1996)].

10. J. Lindhard and V. Nielsen, Phys. Lett. **2**, 209 (1962).

11. *Ion Implantation: Science and Technology*, Ed. by J. F. Ziegler (Academic, Orlando, 1984).

12. E. L. Haines and A. B. Whitehead, Rev. Sci. Instrum. **37**, 190 (1966).

13. U. Fano, Phys. Rev. **72**, 26 (1947).

14. N. B. Strokan, Pis'ma Zh. Tekh. Fiz. **24**, 44 (1998) [Tech. Phys. Lett. **24**, 186 (1998)].

15. E. M. Verbitskaya, V. K. Eremin, A. M. Malyarenko, *et al.*, Fiz. Tekh. Poluprovodn. (St. Petersburg) **27**, 2052 (1993) [Semiconductors **27**, 1127 (1993)].

16. S. M. Sze, *Physics of Semiconductor Devices*, 2nd ed. (Wiley, New York, 1981; Mir, Moscow, 1984), Vol. 1.

17. A. Ivanov, E. Kalinina, G. Kholuyanov, *et al.*, Mater. Sci. Forum **483–485**, 1029 (2005).

18. L. Feldman and J. Mayer, *Fundamentals of Surface and Thin Film Analysis* (North-Holland, New York, 1986; Mir, Moscow, 1989).

19. V. F. Kushniruk, Preprint No. 13-11889, OIYaI (Joint Inst. for Nuclear Research, Dubna, 1978).

20. V. F. Kushniruk, Preprint No. R13-11933, OIYaI (Joint Inst. for Nuclear Research, Dubna, 1978).

Translated by A. Spitsyn

PHYSICS OF SEMICONDUCTOR DEVICES

"Ideal" Static Breakdown in High-Voltage (1 kV) 4*H*-SiC *p*–*n* Junction Diodes with Guard Ring Termination

P. A. Ivanov^, I. V. Grekhov, N. D. Il'inskaya, and T. P. Samsonova

Ioffe Physicotechnical Institute, Russian Academy of Sciences, St. Petersburg, 194021 Russia

^e-mail: Pavel.Ivanov@mail.ioffe.ru

Submitted May 19, 2005; accepted for publication June 1, 2005

Abstract—Nearly "ideal" static high-voltage breakdown (1060 V) in 4H-SiC p^+–n–n^+ diodes with guard ring termination is observed. At the doping level of 1.9×10^{16} cm^{-3} in the n-type base, the diode breakdown field is 2.7×10^6 V/cm. At the reverse bias as high as 1000 V, the leakage-current density does not exceed 5×10^{-5} A/cm^2. The diodes withstand without degradation an avalanche-current density of 1 A/cm^2, which corresponds to the dissipated power of 1 kW/cm^2. © 2005 Pleiades Publishing, Inc.

The problem of raising the breakdown voltage limited by edge effects remains topical for 4*H*-SiC *p*–*n* structures. To reduce the concentration of the edge electric field in SiC structures, different methods adopted from silicon technology are used: field plates [1], guard ring termination [2–4], and methods based on control over the charge in the depletion region at the edge of a junction, such as partial etching-off of a heavily doped *p*(*n*)-type region [5], ion implantation (with an accurately determined dose of *p*(*n*)-type impurity) into *n*(*p*)-type base [6, 7], etc. Each of these methods has its own advantages and disadvantages, and the search for optimal methods for forming the edge contour of the field is ongoing.

One of the widespread methods for limiting the edge field in high-voltage mesa-epitaxial *p*–*n* junctions is the formation of floating mesa-epitaxial guard rings (MEGR) [4, 5, 8]. MEGR structures are produced by selective etching of the heavily doped epitaxial layer; in this procedure, the main mesa-epitaxial junction and the encircling rings are formed simultaneously. The spacing between the main junction and the first ring is chosen so that the space-charge regions (SCR) of the main and guard *p*–*n* junctions join before the electric field in the structure reaches its critical strength. In the presence of several guard rings, the thickness of the formed SCR smoothly decreases toward the edge of the structure, thus reducing the concentration of the field in the region of the main junction.

The breakdown voltage in SiC structures with floating guard rings is very sensitive to the spacing between the main junction and the first ring, the spacing between the rings, the width of each ring, and the total number of rings. It is noteworthy that, due to the very high field of the avalanche breakdown in SiC, and, accordingly, the very thin SCR at the breakdown, the spacing between the rings must be very narrow. In particular, in [4], the distance of 2 μm between the rings was used

in MEGR SiC diodes with the base doped to a level of 2×10^{16} cm^{-3} and the breakdown voltage of ~1 kV. The best blocking properties (1100 V) were obtained in diodes with 12 (!) guard rings.

As is well known, the influence of edge effects on the breakdown of a diode is suppressed if the depletion layer under the edge of the anode is thick (see, e.g., [9]). Evidently, the efficiency of floating guard rings can be improved if their breakdown voltage is higher than that of the main junction. In this study, we used this approach to fabricate 4*H*-SiC diode structures, which exhibit nearly ideal breakdown characteristics, with four guard rings with a 1 kV breakdown voltage.

For the fabrication of p^+–n_0–n^+ diodes, we used commercial epitaxial 4*H*-SiC substrates grown by Cree Inc (Durham, NC, United States) and presented for study by the Air Force Research Laboratories (Kirtland, NM, United States). According to the specification of the material, the concentration of donors (nitrogen) in the 20-μm-thick n_0-type layer is $N = (1.9–2) \times 10^{16}$ cm^{-3}; the concentration of Al and nitrogen in the p^+ and n^+ emitter layers is 3×10^{19} and 10^{18} cm^{-3}, respectively; and the thickness of the emitter layers is about 1 μm.

Figure 1 shows the MEGR structure of the diodes fabricated. To increase the thickness of the depletion region of the guard *p*–*n* junctions, boron was preliminary introduced by local diffusion into the peripheral region of the main junction. The diffusion was performed from the implanted source: boron ions were implanted directly into p^+-type layer at room temperature (a dose of 3×10^{14} cm^{-2}, energy 100 keV.) The mask for implantation was an Al layer of 1 μm in thickness with annular windows (50 μm in width, inner diameter 350 μm) fabricated by photolithography. The diffusion spreading of the implanted impurity was carried out at 1700°C in an Ar atmosphere for 20 min. As was shown previously in [10], the implanted boron dif-
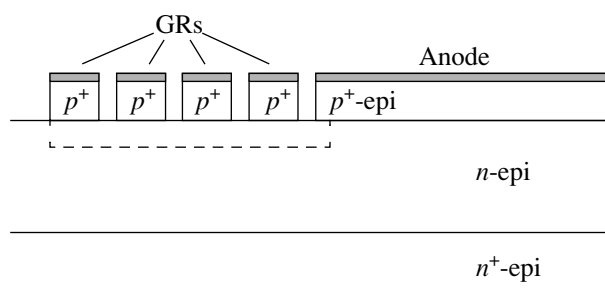
Fig. 1. MEGR structure of 4H-SiC p^+–n–n^+ diodes. The dashed line outlines the region in which donors are partially compensated by boron atoms.

Fig. 2. *I–V* characteristics of 4H-SiC p^+–n–n^+-diodes with MEGR structure. (a) Linear scale (photograph taken from the screen of L2-56 curve tracer; horizontal scale, 200 V per division; vertical scale, 1 mA per division); (b) semilog scale.

fuses comparatively easily in the *p*-type material. The concentration of boron atoms of about 10^{16}–10^{17} cm^{-3} varies only slightly over distances of up to several micrometers from the surface of the *p*-type layer, with the exception of a thin surface region where it sharply decreases due to outward diffusion. As boron atoms enter the *n*-type region, the coefficient of their diffusion decreases drastically, and a decaying concentration profile of boron is formed in the *n*-type layer. In the case under consideration, we expected that donors in the *n*-type layer would be partially compensated by the diffused boron atoms, so that the SCR of the *p–n* junction of guard rings would be somewhat wider than the SCR of the main junction. The MEGR structure was formed by selective ion etching of the *p*-type layer in SF$_6$ plasma. The mask was a 0.12-μm-thick Ni layer with four annular windows formed by flash photolithography. The width of each window was 2 [mu]m, the spacing between the main junction and the first ring (and between the rings) 1.5 μm; the diameter of the main junction was 410 μm, and its area was 1.3×10^{-3} cm^2. A Ni layer of about 1.5 μm in thickness served as an ohmic contact to the p^+-type region of diodes and to the rear *n*-type region; this layer was deposited by ion sputtering and annealed in a vacuum for 10 min at 800°C.

The current–voltage (*I–V*) characteristics of the thus fabricated diode structures were studied in a microprobe setup, without any special heat sink. During the measurement, a 4*H*-SiC wafer was immersed in Fluoroinert dielectric liquid. Figure 2a shows a typical reverse *I–V* characteristic, which shows a very abrupt breakdown of the diode at voltages higher than 1000 V. As can be seen in Fig. 2b, where the *I–V* characteristic is plotted on semilog scale, the leakage current of the diode does not exceed 10 nA up to a voltage of 900 V. A sharp rise in the characteristic, associated with the avalanche current, is observed at V_b of about 1060 V. In the avalanche portion of the *I–V* characteristic, a 10 V increment in the reverse bias causes an increase in the current by about an order of magnitude.
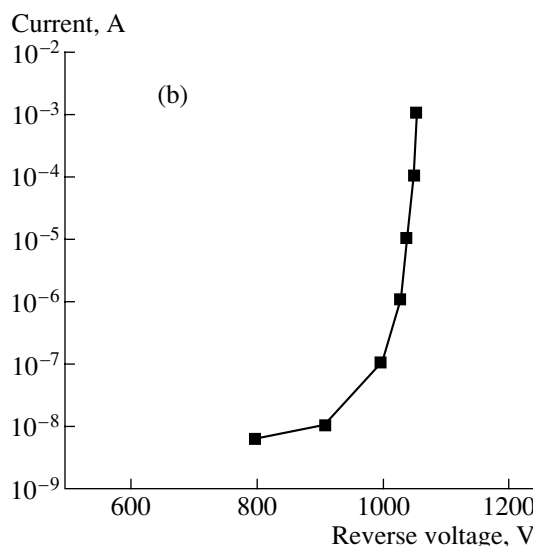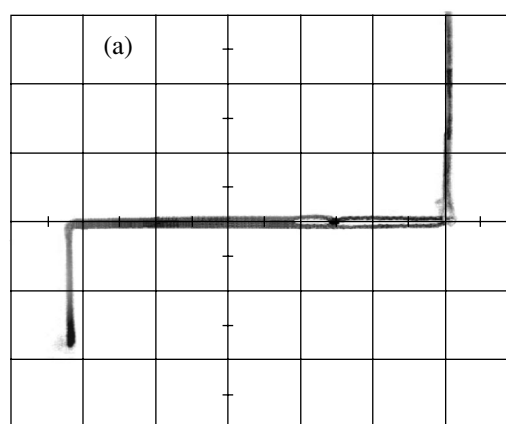
The maximum field strength E_b in the p^+–n junction was calculated from the relation

$$V_b = \frac{\varepsilon E_b^2}{2qN},\qquad(1)$$

as 2.7×10^6 V/cm. Here, q is the elementary charge and ε is the dielectric constant of 4*H*-SiC. In fact, this is just the theoretical limit for a 4*H*-SiC planar p^+–n diode with the base doped to a level of 2×10^{16} cm^{-3} [11]. In the avalanche-breakdown mode, the diodes withstand without destruction a reverse current of no lower than 2 mA, which corresponds to the dissipation power of 1 kW/cm^2. Thus, the fabricated high-voltage diode structures exhibited nearly "ideal" electric breakdown, at least in quasi-static conditions. Further, we intend to perform an experimental examination of the effect of boron diffusion on the efficiency of guard rings and to

study the pulse breakdown of diodes in the modes typical of the generation of ultrafast impact-ionization fronts.

REFERENCES

1. Q. Wahab, T. Kimoto, A. Ellison, *et al.*, Appl. Phys. Lett. **72**, 445 (1998).
2. D. C. Sheridan, G. Niu, J. N. Merrett, *et al.*, Solid-State Electron. **44**, 1367 (2000).
3. D. C. Sheridan, G. Niu, J. N. Merrett, *et al.*, in *Proceedings of International Symposium on Power Semiconductor Devices and ICs* (Osaka, 2001), p. 191.
4. I. Sankin, J. B. Dufrene, J. N. Merrett, and J. B. Casady, Mater. Sci. Forum **433–436**, 879 (2003).
5. X. Li, K. Tone, L. Hui, *et al.*, Mater. Sci. Forum **338–342**, 1375 (2000).
6. D. Peters, R. Schorner, K. H. Holzlein, and P. Friedrichs, Appl. Phys. Lett. **71**, 2996 (1997).
7. K. J. Schoen, J. M. Woodall, J. A. Cooper, Jr., and M. R. Melloc, IEEE Trans. Electron. Devices **45**, 1595 (1998).
8. L. Fursin, K. Tone, P. Alexandrov, *et al.*, Mater. Sci. Forum **338–342**, 1399 (2000).
9. A. Blicher, *Field-Effect and Bipolar Power Transistor Physics* (Academic, New York, 1981; Énergoatomizdat, Leningrad, 1986).
10. M. K. Linnarsson, M. S. Janson, A. Shöner, *et al.*, Mater. Sci. Forum **457–460**, 917 (2004).
11. A. O. Konstantinov, Q. Wahab, N. Nordell, and U. Linderfelt, Mater. Sci. Forum **264–268**, 513 (1998).

Translated by D. Mashovets

===== **PERSONALIA** =====

Yuriĭ Vasil'evich Shmartsev
(On the 75th Anniversary of His Birth)

This year, Yuriĭ Vasil'evich Shmartsev would have celebrated his 75th birthday. He passed away suddenly in January 1993, still full of energy, several days before his birthday.

All of Shmartsev's scientific activity was associated with the Ioffe Physicotechnical Institute of the Soviet (now Russian) Academy of Sciences; he started working at this institute in 1957 after graduating from the physics–mechanics department of Leningrad Polytechnical Institute (now St. Petersburg State Polytechnic University) and Dzerzhinskiĭ Artillery Engineering Academy and after several years of military service in research institutes of the Ministry of Defense of the Soviet Union.

The scope of Shmartsev's scientific interests concentrated around the problem of impurity states in semiconductors. The result of his first studies was the development of a method for growing dislocation-free, doped germanium crystals intended, in particular, for infrared photoelectronics. Shmartsev studied in detail the transport phenomena in heavily doped semiconductors. The results obtained became the experimental basis for development of contemporary theoretical concepts concerning quantum interference of charge-carrier wave functions and electron–electron interaction in disordered semiconductors.

In the 1960s, the studies carried out by Shmartsev led to the development of a general model of impurity states related to nonequivalent extrema in the conduction band of III–V semiconductors. This model is still used at present to explain the processes induced by the *DX* centers. In the 1980s, Shmartsev carried out a series of studies concerned with doping of III–V semiconductors with isovalent impurities. In 1987, Shmartsev and his colleagues were awarded the State Prize of the USSR for the above series of studies.

During his last years, Shmartsev supervised studies concerned with physical phenomena in a two-dimensional electron gas, paying attention to all aspects of this problem, namely, the theory, technology, and new physical effects. Shmartsev and his collaborators discovered the spin–orbit scattering in a quasi-two-dimensional electron gas; in addition, the determining role of scattering by the piezoelectric potential of acoustic phonons was established in studies of the energy relaxation of two-dimensional electrons in the GaAs/AlGaAs heterostructures.

As a whole, the range of Shmartsev' interests in the field of the physics and technology of semiconductors and semiconductor structures was so wide that it is not easy to enumerate all the problems that he found time to solve or that he formulated.

Early progress in the journal *Fizika i tekhnika poluprovodnikov* (*Semiconductors*) was related to Shmartsev's long-term activity as the deputy editor-in-chief of this journal from the date of its foundation in 1967. The scientific profile, thoroughness of reviews, style, presentation, and rating of the journal depended to a great extent on Shmartsev's efforts.

The scientific–public activity of Shmartsev was also extensive. He was a member of the Bureau of the Scientific Council "Physics and Chemistry of Semiconductors" in the Presidium of the Academy of Sciences and took part in meetings of the scientific and specialized councils at Ioffe Physicotechnical Institute and Leningrad (St. Petersburg) Polytechnic Institute.

It is impossible to appreciate Shmartsev's scientific activity without mentioning that he was a brilliant lecturer and the educator of scientific successors. Shmartsev was known as a demanding but benevolent reviewer of theses. Starting in 1961, he read lectures at Leningrad Polytechnical Institute. These lectures corresponded first to a special course in the physics of semiconductors and then (in 1977–1990) to a complete course in general physics for the students of the physics–mechanics department. At present, many of his pupils (doctors and candidates of science) continue physical studies in Russia and in various foreign countries.

At present, twelve years since Shmartsev's death, we, his pupils and followers, continue to remember him quite often owing to the following circumstances related to Shmartsev's traits.

We attempt to follow his idea of organizing experiments so that they provide an unambiguous solution to the formulated problem. Shmartsev referred to such experiments as crucial.

We cannot stand fuzzily formulated ideas when we write articles for publication (such was Shmartsev's teaching). We remember that Shmartsev often altered his own texts as many as ten times and said that we should try to bring a text to perfection.

When dealing with students and postgraduate students, we remember how much time Shmartsev spent with pleasure on his pupils, rejoiced in their successes, aimed at giving them a maximum of independence, and always helped them when difficulties arose.

The principle of Shmartsev to carry out studies that are on an international level and to avoid studies that are intended just to increase the number of publications has made it possible for his pupils to continue their scientific activity even during this time that is so difficult for Russian science.

Shmartsev was and remains for us an example of the scientist for whom scientific activity was the most important and interesting occupation and an example of the scientists who created the spirit of Ioffe Physicotechnical Institute, the spirit of a continuous search for scientific truth, persistent keenness on research, and refinement and benevolence in contacts with colleagues.

Colleagues, pupils, and followers
Editorial board of the journal
Fizika i tekhnika poluprovodnikov

Translated by A. Spitsyn

===== **PERSONALIA** =====

Boris Vasil'evich Tsarenkov
(On the 75th Anniversary of His Birth)

Boris Vasil'evich Tsarenkov is a well-known scientist whose field is the physics and technology of semiconductors and semiconductor electronics. This year, he celebrated his 75th birthday.

Tsarenkov graduated in 1954 from the Leningrad Electrotechnical Institute. In the same year, he started working at the D.N. Nasledov laboratory of the Ioffe Physicotechnical Institute of the Soviet Academy of Sciences; from that time, all of Tsarenkov's scientific activity has been associated with this institute.

The start of his work at this institute coincided with the time when the III–V semiconductor compounds (then, a new class of materials for solid-state electronics) became of interest for scientists and technologists. Tsarenkov made a considerable contribution to both the establishment and the development of scientific concepts concerning the properties of these materials. He was the initiator of the development and study of p–n structures based on the III–V semiconductors in the Soviet Union. For example, the first p–n structure based on GaAs in the Soviet Union was fabricated with his participation (1956). Later, a solar photoconverter (1957) and the first light-emitting diode (1962) were fabricated under his supervision. The most important result of Tsarenkov's studies during the 1960s was his discovery (in collaboration with D.N. Nasledov, A.A. Rogachev, and S.M. Ryvkin) of high-efficiency radiative recombination and the stimulated-emission effect in semiconductors (1962), which led to the development of a semiconductor laser and the advent of luminescent semiconductor electronics.

In 1965, Tsarenkov developed the diffusion technology for p–n structures based on GaAs and GaP. He is a patentee for the first invention in the Soviet Union concerning the liquid-phase epitaxy of the III–V semiconductors, which initiated the wide use of this technology in the Soviet Union.

Commercial production of light-emitting diodes and semiconductor lasers was organized in the 1960s for the first time in the Soviet Union at the Start plant under the scientific supervision of Tsarenkov. In subsequent years, Tsarenkov (in collaboration with his colleagues) carried out fundamental studies of electronic and optoelectronic phenomena in specific graded-gap structures.

Many of his pupils and followers (more than 35 Candidates of Science, 8 Doctors of Science, and hundreds of former students) work successfully for the benefit of Russian and world science. The students graduated from the basic optoelectronics department of the Leningrad Electrotechnical Institute remember with warmth and cordiality the lectures delivered by Tsaren-

kov and the personal contacts with him as their teacher and tutor and as a professor in this department. Tsarenkov worked for a long time as a member of the editorial board of the journal *Fizika i tekhnika poluprovodnikov.*

Tsarenkov was the winner of the Lenin prize (1964) for his involvement in the fundamental studies that led to the development of semiconductor lasers. His studies were awarded various medals of the Exhibition of National Economic Achievements.

At present, Tsarenkov lives in the United States; however, he is well informed about all the events that occur in this country and, of course, at Ioffe Physicote-chnical Institute, which is still close to his heart. Tsarenkov is still in contact with many physicists in Russia and other countries. There are many real friends of his among these physicists; we wish Tsarenkov good health and happiness.

Editorial board of the journal
Fizika i tekhnika poluprovodnikov

Translated by A. Spitsyn